The role of K27M in histone 3 variants and ACVR1 mutations in promoting tumorigenicity of Diffuse Intrinsic Pontine Glioma

Abdulshakour Mohammadnia

Department of Human Genetics, Faculty of Medicine, McGill University, Montreal, Quebec, Canada

November 2021

A thesis submitted to McGill University in partial fulfillment of the requirements of the degree of Doctor of Philosophy (Ph.D.)

Abstract

Diffuse intrinsic pontine gliomas (DIPGs) are the most lethal pediatric brain tumors. In addition to substitution of lysine to methionine at amino acid position 27 of the histone H3 variants (H3K27M) mutations, 20-25% of DIPGs present with somatic mutations in ACVR1 that encodes the ALK2 receptor, member of the BMP receptor family. ACVR1 mutations preferentially cosegregate with H3.1K27M and exert distinct responses to BMP signaling in H3.3 and H3.1K27M DIPGs. To better understand the role of ACVR1 and H3K27M mutations, we used CRISPR-Cas9 system to generate ACVR1 KO, H3.1K27M KO, and H3.3K27M KO cell lines. We show that ACVR1 R206H mutation blocks astrocytic differentiation in H3.3K27M DIPGs whereas ACVR1 G328E/V mutations confer H3.1K27M DIPGs a mesenchymal phenotype. ACVR1 is an important player in DIPG tumorigenesis *in vitro* and *in vivo* and a potential therapeutic target for the recently designed selective ACVR1 inhibitor, M4K2009. Our results suggest that H3.1K27M and H3.3K27M DIPGs emerge from a different cell of origin and implicate distinct roles for the different ACVR1 variant mutations. In addition, we have found H3K27me2 and H3K27me3 levels are lower in H3.1K27M in comparison with H3.3K27M cell lines but their mechanism of action in restricting H3K27me3 is same in both contexts. Furthermore, we have same pervasive acetylation in H3.1K7M with H3.3K27M. Finally, we have provided evidence on distinct transcriptomic and epigenomic profiles of lineage regulators which highlight different cells of origins. In conclusion, H3K27M and ACVR1 mutations exert different effects based on cell of origin to induce tumorigenesis.

Résumé

Les gliomes infiltrant du tronc cérébral (ou DIPG en anglais pour diffuse intrinsic pontine gliomas), représentent la principale cause de mortalité chez l'enfant. Elles représentent 20 à 25 % des tumeurs cérébrales pédiatriques et se caractérisent par une mutation sur l'histone H3.3 : H3.3K27M. En plus des mutations sur l'histone H3, d'autres mutations sont fréquemment associées aux DIPGs, tel que les mutations sur ACVR1, le gène codant pour le récepteur de l'activine (ALK-2) détectées dans environ 20 % des DIPG et s'associant de préférence avec les mutations H3.1 K27M. Ces associations induisent des réponses distinctes sur la voie de signalisation BMP. Pour mieux comprendre le rôle des mutations ACVR1 et H3K27M, nous avons dans un premier temps utilisé le système CRISPR-Cas9 pour générer des lignées cellulaires modifiés : $ACVR1^{mut}$, $H3.1K27M^{KO}$ et $H3.3K27M^{KO}$. Ainsi nous avons démontré que la mutation $ACVR1^{R206H}$ bloque la différenciation astrocytaires dans H3.3K27M tandis que les mutations $ACVR1^{G328E/V}$ confèrent aux DIPGs H3.1K27M un phénotype mésenchymateux. Nos résultats suggèrent que les DIPG H3.1K27M et H3.3K27M émergent chacune d'une cellule d'origine différente, les associant à des rôles distincts lorsqu'elles sont combinées à ACVR1 muté. ACVR1 joue un rôle clé dans les mécanismes tumorigéniques ce qui lui confère un potentiel thérapeutique. En effet de récent découverte ont identifié un inhibiteur spécifique de l'activité de ALK-2 connu sous le nom de M4K2009 permettant de réduire la croissance des tumeurs. De plus, nous avons noté que ces mutations entrainaient des altérations épigénétiques, dont une baisse plus importe de la tri-méthylation de H3K27 dans H3.1K27M comparé à H3.3K27M. Cependant, leur mécanisme d'action pour restreindre la déposition de H3K27me3 est le même dans les deux mutations. De plus, nous avons la même acétylation omniprésente dans H3.1K7M avec H3.3K27M. Enfin, nous avons identifiés grâce aux données transcriptomiques et épigénomiques des régulateurs spécifiques qui mettent en évidence le fait que H3.1K27M et H3.3K27M émergent chacune d'origine cellulaire distinct, ce qui expliquerait les effets différents de H3K27M associé à ACVR1 en fonction de la cellule d'origine affecté induisant la formation de tumeur.

Table of Contents

List of Figures:

List of Tables:

List of Abbreviations:

Diffuse intrinsic pontine glioma: DIPG

pediatric high-grade glioma: pHGG

lysine 27 to methionine: K27M

K27 methylation: H3K27me

H3K27 trimethylation: H3K27me3

mass spectrometry: MS

bone morphogenic protein:BMP

glycine-serine-rich: GS

Polycomb repressive complex 2: PRC2

enhancer of zeste homolog 1: EZH1

enhancer of zeste homolog 2: EZH2

suppressor of zeste 12 homolog 12: SUZ12

embryonic ectoderm development: EED

Su(var)3-9/enhancer-of-zeste/trithorax: SET

polycomb group proteins: PcG

distal-less homeobox 2: Dlx2

Hedgehog: Hh

neural stem cells: NSCs

neural progenitor cells: NPCs

are oligodendrocyte progenitor cells: OPCs

mitogen-activated protein kinase: MAPK

Ras homolog: Rho

guanosine triphosphatase: GTPase

CpG islands: CGIs

epithelial-to-mesenchymal transitions: EMT

fibrodysplasia ossificans progressiva: FOP

receptor-activated SMADs: R-SMADs

inhibitor of differentiation: ID

subventricular zone: SVZ

Glial fibrillary acidic protein: GFAP

homeobox genes: HOX

Gene set enrichment analysis: GSEA

single samples gene set enrichment analysis: ssGSEA

Immunohistochemistry: IHC

chromatin immunoprecipitation and sequencing: ChIP-seq

Principle component analysis: PCA

Quantitative PCR: qPCR

subgranular zone: SGZ

Acknowledgements

I would like to express my deepest gratitude to my supervisor, Dr. Nada Jabado for her mentorship and continuous patience. She graciously accepted me as her graduate student. She taught me how to think critically, and more importantly how to do research in a collaborative way. I found her to be extraordinarily professional and supportive supervisor.

I would like to thank all my colleagues in the Jabado's lab who made my PhD a great and fun experience. Specifically, to our amazing lab manager Damien Faury and all other research assistants, graduate, undergraduate and visiting students of the lab including Augusto Faria Andrade

Andrea Bajic, Ashot Harutyunyan, Bethany Tong , Brian Krug, Carol Chen, Carolina Cavalieri Gomes, Caterina Russo, Emily Nakada, Elias Jabbour, Elvis Valera, Erin (Xiaodan) Yang, Gayathri Yogarajah, Jihane Adelon, Jonathan Pratt, Josiane Alves Fra, Kateryna Rossokhata, Leonie Mikael, Maud Hulswit, Melissa McConechy, Michele Zeinieh, Nicolas De Jay, Nikoleta Juretic, Pariya Azarafshar, Ricardo Santiago Gomez, Tenzin Gayde, Shriya Deshmukh, Sima Khazaei, Véronique Lisi, and Yuhsin Chu for their help, advice, support and stimulating discussions.

Thanks to my committee members Dr. Livia Garzia, Claudia Kleinman, and Jason Tanny whose input and constructive guidance helped me to shape my projects.

Thanks to our all of our collaborators including, Selin Jessa and Nisha Kabir from Kleinman's lab (McGill University), Jing Zhou from Stiles's lab (Dana-Farber Cancer Institute, Harvard University), and Eric Bareke from Majewski's lab (McGill University) and Srinidhi Varadharajan from Mack's lab (St Jude Children's Research Hospital, Memphis)

Last, but not least, I am grateful of my all of my lifelong friends specially Moein Yaqubi and Niusha Khazei and all my family back in Iran who supported me in every single step of my graduation. I never could have finished my PhD without their help.

Preface and Contribution of authors

Contribution to original knowledge and contribution of authors

All concepts, analyses, results, text, and interpretations presented in this thesis represent original scholarship.

Preface

I joined department of human genetics at McGill University in fall 2016. I started my PhD under the supervision of Dr. Nada Jabado. I worked on mutations and tumorigenesis events of diffuse midline gliomas characterized by H3K27M mutations. The content of this thesis is as a result of my research efforts during the past 6 years

Contribution of authors

Augusto Faria Andrade: Involved in cell cycle and DNA synthesis analysis.

Ashot Harutyunyan: Generating ChIP-seq datasets and mass spectrometry analysis and involved in ChIP-seq analysis and writing results and method sections.

Caterina Russo: involved in generation of H3.3K27M-KO from BT869 cell line.

Damien Faury: Involved in data generation.

Elias Jabbour: Involved in generation ACVR1-KO from SU-DIPGIV cell line.

Michele Zeinieh: injecting cell into mice pontine for H3.3K27M cell lines and subQ injection for H3.1K27M cell line, drug screening assays, clonogenic assays, involved in writing results, discussion, methods of ACVR1 chapter.

Yuhsin Chu: Involved in qPCR experiments to characterize isogenic CRISPR clones and differentiation experiments.

Nisha Kabir: ssGSEA analysis for ACVR1 KO clones and bulk RNA-seq analysis of ACVR1 edited clones.

Jing Zhou: Overexpression of ACVR1 R206H mutation in NPCs, differentiation of NPCs, treatment of NPCs with BMP4 and Activin A ligands. Involved in western blot of ACVR1 mutations characterization.

Eric Bareke: Involved in bulk RNA-seq analysis for ACVR1 edited clones.

Srinidhi Varadharajan: Pervasive acetylation analysis for H3.1K27M and H3.3K27M cell line and tumors.

Chapter 1

Introduction and literature review

Introduction:

Diffuse intrinsic pontine glioma (DIPG) is the most lethal pediatric brain tumor and accounts for almost half of the pediatric high-grade gliomas. DIPGs emerge in the ventral pons, which prevents surgical resection due to the difficult access to this location, while radiotherapy temporarily alleviates symptoms without enhancing survival rate. Despite extensive efforts to treat DIPGs using chemotherapeutics and other strategies, the median overall survival does not exceed one year (1).

Epigenetic mechanisms play a crucial role in DIPGs tumorigenicity. Indeed, around 80% of DIPGs carry the lysine 27 to methionine (K27M) mutation in histone 3 genes, H3.3 (*H3F3A* gene) (63%) or H3.1 (*HIST1H3B* gene) (21%) (2). H3K27M mutations induce significant changes in the epigenetic landscape of tumor cells by promoting a global reduction of H3K27 trimethylation (H3K27me3). Several conflicting data exist on the differential effect of K27M on canonical (H3.1 and H3.2) and noncanonical H3 (H3.3) variants on the epigenome. To assess whether the type of oncohistone also participates in specifying cell identity, we compared the individual impact of K27M on H3.1 and H3.3 epigenome using histone mass spectrometry (MS) and ChIP-seq in patient-derived cell lines.

Despite the importance of H3K27M mutation as a main driver of DIPG tumorigenesis, K27M alone is unable to induce tumor formation when expressed in the early developing mouse brain, additional cooccurring mutations such as *PDGFRA, TP53, PPM1D, PIK3CA,* and *FGFR1* are required (3–6). Somatic mutations in the ACVR1 gene have been identified in 20-25% of DIPGs. Patients carrying mutant ACVR1 are younger and benefit from a longer overall survival (6). ACVR1 encodes the ALK2 receptor, a protein kinase belonging to the type I bone morphogenic protein (BMP) receptor family. Mutations in ACVR1 are mainly found associated with H3.1K27M in DIPGs (7–10). Germline mutations in ACVR1 were first identified in fibrodysplasia ossificans progressiva (FOP), an autosomal dominant disorder characterized by ectopic formation of bone in soft tissues (11), and more recently in 3.4% of endometrial cancers (12). Those mutations target residues located in the inhibitory glycine-serine-rich (GS) domain and in the ATP binding pocket of the kinase domain, rendering the receptor slightly hyperactive in the absence of ligand (6,9). ACVR1 R206H (Arg206His) mutation located within the GS domain predominates in FOP, however, in

DIPGs several other mutation variants exist and are located to different domains of the receptor. Previous work from our group demonstrated that ACVR1 is a clonal mutation and constitutes an early event in tumorigenesis (13), but ACVR1 alone is unable to generate tumors and can induce glioma-like lesions only in the presence of H3.1K27M and *TP53* deletion (14). It is still not fully understood how ACVR1 contributes to tumorigenesis in DIPGs. A recent study demonstrated that substitution of glycine to valine at amino acid position 328 of the ACVR1 gene ($ACVR1^{+/G328V}$ mutation) causes oligodendroglial differentiation arrest and high-grade diffuse glioma in mice when combined with H3.1K27M and (substitution of histidine to arginine at amino acid position 328 of the Pik3ca gene) $Pik3ca^{H1047R}$ (15). However, it is not well elucidated how ACVR1 induces tumorigenesis when combined with the different H3K27M histone variants, H3.1 or H3.3, and whether ACVR1 employs the same mechanisms for tumor formation in these two backgrounds.

In this study, we found a strong correlation between $ACVR1^{+/R206H}$ mutation and H3.3K27M, and between $ACVR1^{+/G328E/V}$ and H3.1K27M, suggesting context dependencies of these two mutations. ACVR1 mutations exert different responses in H3.1 and H3.3K27M to BMP signaling proteins and induce profound transcriptomic changes. We used the CRISPR-Cas9 system to generate isogenic ACVR1 knockout cells derived from primary patient cell lines. Knocking out ACVR1 significantly decreased cell proliferation *in vitro* and increased survival of mice in both H3.1 and H3.3K27M DIPGs albeit through separate mechanisms. ACVR1 R206H mutation in H3.3K27M impairs the ability of the cells to differentiate to astrocytes, whereas the G328E/V mutation alters the mesenchymal properties of H3.1K27M cells by disrupting their interaction with the extracellular matrix. These results show the role of ACVR1 mutations in tumorigenesis is context dependent and suggest that they underlie different cells of origin that largely depend on the partnering histone mutation. We finally demonstrate that a new ALK inhibitor, M4K2009, is highly specific to ALK2 and that it exerts beneficial responses in DIPGs as a potential candidate for therapeutic targeting. Furthermore, we found epigenomic differences between H3.1K27M and H3.3K27M cell contexts. Comparison of H3K27 methylation levels by MS and ChIP-seq experiments revealed lower levels of H3K27me2/3 in H3.1K27M cell lines in comparison with H3.3K27M cell lines. To compare the effect of H3.1K27M and H3.3K27M in their respective isogenic contexts, we CRISPR/Cas9 knocked out H3.1K27M in three HGG cell lines and profiled

H3K27me2/3 by ChIPseq. In both H3.1 and H3.3K27M cell lines, removal of the mutation resulted in increased spread of H3K27me2/3. showing that the effect of the oncohistone on H3K27me2/3 is reversible regardless of the H3 variant targeted by K27M.

Literature review:

Diffuse intrinsic pontin glioma

Diffuse intrinsic pontine glioma (DIPG) is the most lethal pediatric brain tumor and accounts for almost half of the pediatric high-grade gliomas. In addition to an examination for abnormalities via radiography analysis in the pons, neuropathological symptoms including cranial nerve palsies and long tract and cerebellar signs are the basis for DIPG diagnosis (16) .

DIPGs emerge in the ventral pons, a part of the brain which is involved in the vital functioning of the body including in breathing, blood pressure, and heart rate. While it plays this critical role, its anatomical location prevents easy access to surgical resectioning while an alternative treatment like radiotherapy only temporarily alleviates symptoms without enhancing survival rate (17) . Other therapeutic strategies including cytotoxic chemotherapy, small-molecule inhibitors, and immunotherapies have been used on their own or in combination with radiotherapy, but none of these treatments have increased survival rates in DIPG patients (18). So, despite extensive efforts to treat DIPGs using chemotherapeutics and other strategies, the median overall survival of those diagnosed with DIPG does not exceed one year (1).

Recently, research in this field has been fueled by an increase in the number of biopsies being performed based on the safe computer-aided stereotactic biopsies. Additionally, access to biopsies has helped researchers to design genetically stratified clinical trials that aim to provide better treatment for DIPG patients (17).New aspects of DIPG biology have been discovered thanks to new and safe biopsy strategies and sequencing technologies to obtain and better characterize patient-derived tumor cells (19). A wide range of genes involved in epigenetic regulation, signaling pathways and nervous system development are described to play a role in the DIPGs. The most relevant mutation is the lysine 27 to methionine (K27M) mutation in the histone 3 genes, specifically in histone variants H3.3 encoded by H3F3A and H3.1 encoded by HIST1H3B genes (2) . These recurrent gain-of-function mutations are mutually exclusive and are present in 84% of DIPGs. The K27M mutation is more prevalent in H3F3A (63%) than in HIST1H3B (21%).

Histone variants and their functions during development

Histone proteins form a protein complex with DNA in structures called nucleosomes. Nucleosomes are comprised of octamers, which contain four core histone proteins, H2A, H2B, H3 and H4, and are approximately 147 bps of DNA in length (20) . In addition, each nucleosome can contain linker DNA and a linker histone known as H1 (20) . Posttranslational modifications occur on the N-terminal of histone H3, including methylation, acetylation, ubiquitination, etc., are involved in regulation of gene expression, DNA replication and repair. There are three variants of histone H3; these are H3.1 (canonical), H3.2 (canonical), and H3.3 (non-canonical), which are coded by 17 different genes. H3.1 and H3.2 are categorized as canonical histone H3 and are expressed during the S phase of the cell cycle, but H3.3, categorized as non-canonical histone H3, is expressed throughout the cell cycle (17). In addition to different expression patterns, it has been shown canonical and non-canonical histone H3 variants have different functions. For example, H3.3 is deposited in transcriptionally active genes and generally modified by posttranslational modifications associated with activation of transcription, but variants H3.1 and H3.2 are deposited throughout the genome and generally associated with modification involved in repression of gene expression (17). Also, silico analysis of bulk RNA-seq data has shown these variants have different gene expressions during development; for example, H3.3 genes are expressed in all developmental stages but decrease in later developmental stages while H3.1 genes significantly down-regulate in prenatal stages and remain silenced with development progression. In addition, this transcriptomic analysis revealed highest expression level HIST1H3B in early developmental stages among other encoding H3.1 protein isoforms (21).

Polycomb repressive complex 2 (PRC2) is involved in gene expression repression by catalyzing H3K27me2 and me3 posttranslational modification on lysine 27 of histone H3. This complex is composed of three core proteins, enhancer of zeste homolog 1 (EZH1) or homolog 2 (EZH2), suppressor of zeste 12 homolog 12 (SUZ12), and embryonic ectoderm development (EED). EZH1 and EZH2 are core catalytic subunits of the PRC2 complex due to the Su(var)3-9/enhancer-of-zeste/trithorax (SET) domain, which catalyzes H3K27me2 and H3K27me3 (22). It has been shown that polycomb group proteins (PcG) are involved in the developmental transition of the nervous system. For example, these proteins downregulate genes involved in neurogenesis and lead to

transition into astrocytic differentiation by facilitating expression of genes involved in astrocytic fate. In addition, it has been shown that polycomb group proteins facilitate oligodendrogenesis through repression of distal-less homeobox 2 (Dlx2); this gene represses oligodendrocytic cell fate identity (23).

Role of histone mutations in diffuse midline glioma

Both H3.3K27M and H3.1K27M mutations significantly affect the epigenetic landscape of tumor cells by promoting a global reduction of K27 methylation (H3K27me). It has been suggested that the K27M mutation inhibits polycomb repressive complex (PRC2) protein activity, which is responsible for the generation of different K27 methylation states (mono-, di-, and tri-) that play an important role in the regulation of gene expression (24). It has been shown that K27M-mutant histones bind Ezh2 (the core catalytic component of PRC2) with higher affinity relative to wild type H3 histones. Despite similarities in H3.1 and H3.3K27M mutation effects, differences have been exhibited that include age of occurrence, mutation partnership, tumor locations, and gene expression profiles (25).

Despite the global decrease of H3K27me2 and H3K27me3, levels of H3K27ac have been shown to increase in K27M mutant cells (24,26,27). Transcriptomic analysis of H3.3K27M tumors has revealed the global upregulation of PRC2 target genes and downregulation of a subset of genes involved in the regulation of developmental processes and the cell cycle; for example, G0-G1 to S phase regulator, CDKN2A/P16, is downregulated in H3.3K27M tumors (28). Another characteristic of DIPGs is their amplifications in cell cycle regulator genes, especially those genes involved in G1-S transitions. For example, there are amplifications in cyclin D family members, CCND1, CCND2, CCND3, and cyclin dependent kinase inhibitors CDK4 and CDK6 (29). These cyclins and kinases form complexes that are involved in inducing cell cycle progression from G1-S phases through phosphorylation of retinoblastoma proteins (29–31). Due to their critical role in the proliferation of cell cycle regulator genes and its role in different cancers, there are multiple ongoing clinical trials which target CDKs, specifically CDK4 and CDK6 in DIPGs (17).

Currently, our group has shown that removing the H3.3K27M mutation using CRISPR-Cas9 from patient-derived cell lines restores normal levels of H3K27me3 (32). In addition, we have found

levels of H3K27me2 in H3.3K27M mutated patient-derived cell lines are similar to H3K27me3 in isogenic H3K27M-KO cell lines (32). Removing the H3K27M mutation in DIPG xenografts showed, in addition to restoring normal levels of H3K27me3, significantly increased survival of mice in comparison with the control group (32). Another group used a knockdown model for H3K27M and xenografts and showed similar restoration of H3K27me3 and increase in mice survival rates (33).

Epigenetic and chromatin accessibility is crucial for precise temporal and spatial gene expression regulation during development and differentiation (34,35). It has been shown, and very well studied, that the activity of many central regulators of development and differentiation in pluripotent states are regulated by H3K27me3 and H3K4me3 histone proteins posttranslational modifications; these, in turn, are associated with gene expression suppression and activation, respectively (36). Regulatory elements of developmentally important genes marked with the presence of these two histones are known as "bivalent domains," which keep genes in poised states. Removing H3K27me3 marks leads to activation of gene expression of these lineage-determining genes due to the presence of the H3K4me3 mark (36). Integrated transcriptomic and epigenomic analyses have shown an upregulation of many genes in H3K27M, which are enriched in bivalent promoters. Many of these genes are related to immature differentiation states (32,33).

Developmental and cellular origin of diffuse intrinsic pontine glioma

The restriction of DIPGs to the ventral pons and their occurrence during specific childhood periods, suggests a potential deviation from normal development. Morphometric analysis of human pons during childhood revealed a five-fold increase in pontine size within the first five years of life. This growth was continuous but more gradual throughout the remaining childhood years (37,38). The initial upsurgence in volume is due to an increase in myelination (37,38). Monje et al. (2011) showed two populations of Nestin-expressing neural precursor cells in the ventral pons and subventricular zone of human postmortem samples. In addition, the same group showed that 40% to 60% of Nestin neural precursor cells express oligodendroglial precursor transcription factor, Olig2. This population of cells decreased by age two and increased again by

age six, which corresponds with DIPG occurrences. Also, they showed that the Hedgehog (Hh) signaling pathway is active in DIPGs and it is involved in self renewal of DIPGs (38). Previously, it has been shown that the Hedgehog (Hh) signaling pathway is involved in many developmental processes. It has been shown Olig2 is regulated by the Shh signalling pathway in the ventral embryonic spinal cord (39). So, Monje et al. (2011) derived pontine precursor-like cells expressing Olig2 and Sox2 from mouse to study role of Sonic hedgehog (Shh) in this cellular context. Constitutively, activating the Hedgehog pathway in Olig2-Cre mice showed a 2.8- fold increase in the number of proliferating cells in the ventral pons of P14. Studies have shown that the size of the pons increases six folds due to myelination by oligodendrocytes during the first five years of life (37). A recent study using mice has shown the same five-fold increase in basis pontine, postnatally, but this increase in size is not dependent on myelination but is dependent on proliferation (40).

Previously, it was shown that H3K27M mutations are not able to generate tumors *in vivo* without the presence of other co-occurring mutations, such as TP53 or PPM1D (12). Introduction of the H3K27M mutation in neural stem cells (NSCs) derived from human embryonic stem cells (ESCs) caused a higher proliferation rate, but introduction of the same mutation in ESCs, ESC-derived astrocytes, and human fibroblasts did not increase cell proliferation (25,41). Presence of the H3K27M mutation in combination with TP53 knockdown in NSCs leads to the generation of neoplastic properties (41). It has been shown that the over-expression of H3K27M drives tumorigenic events in NPCs (3,24,41). A more recent study by Nagaraja et al., (2019) showed that H3K27M mutations maintain the stem cell state of NPCs, but this activation of tumorigenic pathways more closely resembles *in vivo* medulloblastoma tumorigenic events (42).

Pathania et al., showed that within the developing hindbrain the overexpression of H3.3 K27M in combination with Trp53 loss in embryonic neural progenitor cells (NPCs) is the origin for some pontine nuclei; this leads to both focal and diffuse tumors. The same conclusions could not be obtained in similar experiments performed in postnatal mice (4). In addition, the H3.3K27M mutation is able to immortalize human fetal NPCs derived from the hind brain but not progenitors derived from the cortex (43). These studies indicate that fetal NPCs derived from the hind brain are possible cells of origin for DIPGs. Histone mutations in cancer may act by preventing normal

differentiation and maintaining cells in a specific cell identity state (25). Funato et al. (2014), showed that the knockdown of TP53 and expression of H3K27M in NPCs led to a complete block of differentiation towards astrocytic lineage and low levels of differentiation to oligodendrocytes and neurons (41). Injection of these cells in the pons of mice resulted in the slow growth of tumors, which resemble lower grade DIPGs (41). Comparison with published gene expression data for early neural plate (neural rosette) stages and late neural (neural precursor cells) stages showed significant correlation between H3.3K27M-regulated genes and the neural rosette stage (41). In addition, they showed these genes were upregulated in DIPGs with a H3K27M mutation in comparison with G34R/V tumors or histone wild type DIPGs (41). It was shown that expression of H3.3K27M in neural precursor cells reprograms these cells into the more primitive neural rosette state (41). Interestingly, Funato et al., showed expression of H3K27M alone or with P53 corresponded to a gain of H3K27me3 as well as the down-regulation of oligodendrocyte differentiation genes Nkx2.2 and MBP in neural precursor cells (41).

Furthermore, studying single cell RNA-seq data derived from six patients with H3.3K27M mutations revealed oligodendrocyte progenitor-like cells as the largest population of stem cells in H3.3K27M tumors (44). This data set has been generated using fresh tissue samples from DIPG patients. They have found oligodendrocyte progenitor like cells (OPC-like) as comprising the majority of tumor cells in comparison with more differentiated cells. These cells showed higher proliferation and tumor progression capacity in comparison with more differentiated cells in H3K27M DIPGs.

Comparing the transcriptomic profile of DIPG at the single cell level with isocitrate dehydrogenase (IDH) mutant oligodendroglioma (IDH-O), IDH-mutant astrocytoma (IDH-A), and IDH–wild-type glioblastoma revealed higher numbers of upregulated genes in H3K27M gliomas (44), which is consistent with previous reports on the mechanism of blocking PRC2 action using bulk transcriptomic and epigenomic analysis.

Filbin et al., identified four transcriptomic programs, including cell cycle (such as PCNA and CDK1), astrocytic differentiation (AC-like) (such as GFAP and APOE), oligodendrocytic differentiation (OClike) (such as MBP and PLP1), and OPC-like programs (such as PDGFRA and CSPG4) in H3K27M

gliomas. Scoring cells based on these four programs showed OPC like cells as the only proliferative cell population with potential in generated oligodendrocyte- and astrocyte-like cells (44).

Enhancer analysis using H3K27ac ChIP-seq experiments from twenty five H3K27M DIPGs and five non-malignant pontine samples revealed three distinct identities, including H3.1K27M, H3.3K27M and normal pons (42).

Enhancer analysis showed higher activation of PI3K signaling and p38 mitogen-activated protein kinase (MAPK) signaling in H3.1K27M DIPG in comparison with H3.3K27M DIPGs. Previously, mutations in PI3K were shown to co-occur with the presence of H3.1K27M DIPGs (5). On the other side, H3.3K27M super enhancer analysis revealed the presence of Ras homolog (Rho) guanosine triphosphatase (GTPase) activity, cytoskeletal remodeling, and early neural development enrichment in comparison with H3.1K27M tumors (42). Motif analysis showed a family of RNF-like transcription factors, which play a role in midline brain formation are enriched in H3.3K27M DIPGs (42,45).

The study of early events driven by H3K27M is hindered in tissue and *in vitro* models, so Nagaraja et al., (2019) generated, stage-specific, human stem cells are used to study the role of H3K27M in chromatin remodeling (42). Enhancer analysis in three relevant stem cell contexts, including multipotent neural precursors, pre-OPCs, and early OPCs, showed that oligodendroglial lineage more closely resemble DIPGs when compared with multipotent neural precursors. H3.3K27M showed a higher correlation with oligodendroglial lineage and authors claimed that H3.1K27M is possibly more differentiated in the lineage than other mutations and they were not able to capture more differentiated states in their data (42).

H3.1K27M and H3.3K27M showed a similar global decrease of H3K27me3 in one cycle of early oligodendrocyte precursor cells but differentH3K27me3 loci affected. CpG islands (CGIs) recruited PRC2 (46) and H3K27M led to the global loss of H3K27me3 (42). Also, H3.3K27M is colocalized with wild type H3.3, and higher levels of K27M mutations are correlated with higher levels of PRC2 inhibition. So, authors observed higher levels of correlation between CGIs and loss of H3.3K27me3 in the presence of H3.3K27M in early oligodendrocyte precursor cells (42). The

same mechanism is not happening in early oligodendrocyte precursor cells with H3.1K27M mainly due to their ubiquitous distribution on the genome. Over-expression of both H3.1K27M and H3.3K27M mutations in early oligodendrocyte precursor cells for two cell cycles (25 days) led to distinct enhancer and promoter profiles. These differences are comparable with those observed between H3.1K27M and H3.3K27M DIPGs (42), including p38 MAPK signaling activation in H3.1K27M, Rho GTPase signaling, neurite extension, and early neural development pathways in H3.3K27M contexts.

Comprehensive transcriptomic analysis using 78 pediatric high-grade gliomas, including 33 H3K27M and 43 non H3K27M tumors, revealed a profile of 49 genes associated with epithelial-to-mesenchymal transitions (EMT). These are differentially expressed in H3K27M tumors in comparison with non H3K27M tumors (47). From this profile of genes, 26 are highly expressed in H3K27M tumors and are related to pre-EMT; 23 genes are highly expressed in non H3K27M and are mostly associated with post-EMT. Analysis of these genes in nine independent gene sets related to epithelial cells and early brain development showed strong enrichment of 26 pre-EMT genes, whereas a profile of 26 random genes did not show any significant enrichment(47).

A number of experimental studies have supported findings that cell of origins in EMT states having the potential to generate H3K27M tumors. For example, Funato et al., 2014 showed that the over-expression of H3K27M, p53 loss, and PDGFRA NPCs injected mice brain induced low grade gliomas and generated tumors expressing neuroepithelial genes (41). In another major study, Pathania et al., (2017) determined that an over-expression of H3K27M and the loss of P53 in embryonic NPCs can generate gliomas in the forebrain and hindbrain of mice (4). These tumorigenic events are not happening in post-EMT cell models. For example, Funato et al., used constitutive expressions of H3K27M, p53 loss, and PDGFRA in astrocytes, but this model did not generate tumors (41).

Sanders et al., used single cell RNA-seq derived from organoids which mimics the early weeks of human prenatal cortical development and generates relevant cell types to study EMT events Based on scoring method, they showed lower EMT scores for neuroepithelial and early radial glia cells in comparison with more differentiated intermediate progenitors, late radial glia, and

neurons (47). These more differentiated intermediaries have higher EMT scores or they are post-EMT. Mapping H3K27M over-expressed genes to the single cell RNA-seq and clustering analysis revealed these tumors more closely resemble neuroepithelial cells and radial glial cells with pre-EMT signatures. In summary, authors showed H3K27M tumors are showing pre-EMT signatures, which reflects specific developmental time points and cell of origins (47).

Single cell and bulk RNA-seq analysis showed H3 wild type (H3WT) gliomas are showing post-EMT signatures with high expressions of post EMT marker genes, including CDH2, CDH6, and VIM. There are multiple clusters in single cell RNA-seq data with different EMT signatures. Case in point, one cluster of cells with H3K27M cells showing higher post-EMT signals characterized by the high expression of CDH11 (47). Another example is the FN1 marker gene which reflect a more differentiated subclonal population. In contrast, they have identified two clusters of cells with high expressions of pre-EMT genes, including CADM1, PTEN, CTNNB1, and SFRP1 (47). Finally, there is an intermediate cluster with expressed genes playing a role during EMT. This cluster of cells expresses high levels of SMAD2 and VCAN and is mainly composed of H3.1K27M cells (47). GSEA analysis of genes upregulated in H3.1K27M in comparison with H3.3K27M revealed epithelial terms are enriched in H3.3K27M cells, but mesenchymal signatures are stronger in H3.1K27M cells. An analysis of single cell RNA-seq from H3.1K27M tumor samples highlights a higher score and completeness of EMT than most other cell types with the exception of non-H3K27M tumors. Bulk RNA-seq of SU_DIPGIV (H3.1K27M), SU_DIPGVI and JHH-DIPG1 (H3.3K27M cell lines) showed significantly higher scores of EMT completion in comparison with the other two H3.3K27M cell lines (47). In addition, culturing five H3.1K27M and eight H3.3K27M cell lines showed a high attachment of H3.1K27M and higher neutrosphere formation capacity in H3.3K27M, which could infer that H3.1K27M are more differentiated (47).

ACVR1 mutations and BMP signaling in diffuse intrinsic pontine glioma

Mutations in the ACVR1 gene, which encodes type I bone morphogenic protein receptor ALK2 and belongs to the bone morphogenic signaling (BMP) family of proteins, mainly co-occurs with the H3.1K27M mutation (7–10,48). ACVR1 mutations occur in 20-25% of DIPG tumors and were recently identified in 3.4% of endometrial cancers (12). Decades before the discovery of ACVR1

mutations in DIPGs, germ line mutations in ACVR1 were identified in fibrodysplasia ossificans progressiva (FOP). FOP is an autosomal dominant disorder that leads to the ectopic formation of bone in soft tissues, like muscle, tendon, and ligament (6). Different ACVR1 mutations have been reported to result in a slightly hyperactive form of this protein, which functions even in the absence of an activation signal (6,9). ALK2 belongs to the bone morphogenic signaling (BMP) family in the TGF-beta superfamily. Ligand dependent activation of TGF-beta and BMP signaling pathway is dependent on the formation of heterotetramer complexes of type I and two type II receptors. The binding of ligand(s) to receptors leads to type II and type I receptor interactions. This, in turn, causes type II receptor, which are constitutively active kinases, to phosphorylate type I receptors (49,50). Finally, phosphorylated and activated receptors cause the phosphorylation of intracellular effectors of TGF-beta and BMP signaling known as receptor-activated SMADs (R-SMADs). R-SMADs interact with SMAD4, which is known as co-Smad (Smad4), to form a complex, which is then translocated to the nucleus where it is involved in gene expression regulation in association with other coactivators or corepressors (51). Different types of Type I receptors in TGF-beta and BMP pathways will phosphorylate different R-SMADs; for example, ACVR1B/ALK4 and ACVR1C/ALK7 phosphorylate SMAD1 and SMAD2 but other ALKs, including ACVR1/ALK2, BMPR1A/ALK3, and BMPR1B/ALK6, are involved in the phosphorylation of SMAD1, SMAD5, and SMAD8/9 effectors (51).

DIPG patients with ACVR1 mutations tend to be younger and have longer survival time in comparison with ACVR1 wildtype DIPG patients (6,8). It has been shown that ACVR1 is a clonal mutation and is present as an early event of tumorigenesis (13), but ACVR1 mutations alone are not able to generate tumors when expressed in P53 null mouse astrocytes and implanted in brain parenchyma (12).

Mutations in ACVR1 mainly occur in two regions, the inhibitory glycine-serine-rich (GS) domain and in the ATP binding pocket of the kinase domain, both of which lead to hyperactive versions of the protein (9). ACVR1 mutations increase the phosphorylation of Smad1/5/8 down-stream effectors in BMP signaling. Subsequently these Smad1/5/8 interact with Smad4 and migrate to the nucleus to regulate BMP target genes, including the inhibitor of differentiation (ID) 1-3 genes (6). Wu et al. (2014) used zebrafish embryos to assess the effects of different ACVR1 mutations

and found that the injection of normal ACVR1 mRNA led to dorsalized phenotypes, whereas ACVR1 mutations led to ventralized phenotypes (9). They showed that the substitution of arginine to glycine at amino acid position 258 of the ACVR1 gene (R258G mutation) had a minimal effect on ventralization while the G328V mutation had the strongest effect. In contrast to FOP disease, which has several established *in vivo* and *in vitro* models, there is a lack of DIPG models with ACVR1 mutations which can recapitulate tumorigenic events (12). Additionally, there is a lack of appropriate *in vivo* models that capture ACVR1 behaviour and histone mutations together across different developmental timepoints, which is warranted by the very heterogenous and context-dependent nature of BMP signaling. For example, during early neurodevelopment, high levels of BMP signaling increase self-renewal and proliferation of neural progenitor cells, but at later stages of neurodevelopment BMP signaling induces astrocytic and neuronal differentiation from neural progenitor cells (12). In addition to ACVR1 mutations, there are other genetic abnormalities or mutations in the BMP signaling pathway, for example the amplification of ID2 and ID3 or mutations in BMP3, BMPK (5). Recently, Hoeman et al., (2019) showed the *in vitro* over-expression of ACVR1 R206H that induces the expression profile of genes related to the mesenchymal signature and this mutation is activating STAT3 signaling (14). Using the RCAS mouse model, the same group showed that the overexpression of PDGFA and ACVR1 R206H mutation accelerated tumorigenesis. Adding H3.1K27M to the over-expression of PDGFA as well as to the ACVR1 R206H mutation led to higher tumor growth and malignancy (14).

Recently, it has been shown that the ACVR1 R206H mutation does not need upstream type II receptor kinases to phosphorylate SMAD1/5 (52). In the presence of Activin A, this ligand induces ACVR1/ALK2 clustering, which induces autoactivation and induction of SMAD1/5 (52). Also, in normal physiological conditions, Activin A can induce ALK4 (ACVR1B) and ALK7 (ACVR1C), which requires the type II receptors ACVR2A/B. It is not, however, able to induce ALK2 (52).

In addition, it has been shown in two independent studies, one using a mouse model and the other, a FOP patient-derived induced pluripotent stem cells, that Activin A strongly induces phosphorylation of SMAD1/5 in the presence of ACVR1 R206H mutations and not wild type ACVR1 (53,54). More recently, it has been shown that Activin A can induce the weak phosphorylation of SMAD1/5 in HEK293 cells, but this activation becomes significantly stronger

in the presence a heterozygous or homozygous mutation at the ACVR1 R206H site (52). In addition, ACVR1-KO HEK293 cells still responding to BMP4 and BMP2 were comparable with the parental cell line but significantly decreased in response to Activin A, Activin B, BMP4/7, and to a lesser extent BMP7 (52). As Activin A is known to be a TGF-beta ligand, the treatment of HEK293 cells in the presence or absence of ACVR1 mutation showed significant increases of SMAD2 phosphorylation in comparison with the control group (52). In addition, the weak activation of BMP pathways in the presence of Activin A and phosphorylation of SMAD1/5 is not dose-dependent, but in the presence of the ACVR1 R206H mutation it became similarly dose-dependent in its response to the BMP4/7 ligand (52). Interestingly, ACVR1 R206H mutations in HEK293T cells showed an extended activation time of SMAD1/5 phosphorylation in comparison with wild type HEK293T cells. These extensions in the induction BMP pathway and phosphorylation of SMAD1/5 is not due to intracellular signaling nor the presence of recycling receptors on the cell surface. Furthermore, ACVR1 R206H mutation leads to an increase in the catalytic efficiency of ACVR1 in response to Activin A. ACVR1 R206H activation in the presence of Activin A is not only independent from ACVR1B/ALK4 and ACVR1C/ALK7 as type I receptors, but also it does not need kinase activity of type II receptors to phosphorylate SMAD1/5 (52).

BMP signaling is highly regulated both spatially and temporally by other signaling pathways during development; for example, in postnatal stages, BMP signaling induces astrocytic differentiation and inhibits oligodendrocyte and neuronal differentiations (12). During early embryonic development, the inhibition of BMP signaling plays a critical role in the differentiation of ectoderm cells into neuroectoderm cells and this signaling pathway is involved in neural crest specification. So, the BMP signaling pathway is playing a role in the establishment of both the central and peripheral nervous system. The gradient of BMP signalling pathways secreted by dorsal structures in the developing brain and spinal cord is involved in dorsal-ventral patterning (55). BMP signalling is highly context dependent and in different developmental time points, it plays a different role; for example, during forebrain development, it is initially involved in neurogenesis and then astrogliogenesis and finally, it participates in neurite outgrowth from immature neurons (55). BMP signalling is also involved in the of neural stem cell niches in the

subventricular zone (SVZ) and subgranular zone (SGZ), which is highlighting the highly context dependent nature of this signalling pathway (55).

Previously, it was shown that the possible origin of DIPGs are oligodendrocyte progenitor cells (OPCs) (38,44). Many studies indicate that the BMP signaling activation and phosphorylation of smad1/5/8 promotes differentiation towards neuronal and astrocytic lineages (56). Interestingly, it was shown that BMP-Smad signaling induces postnatal subcortical bipotent oligodendroglial-astroglial (O-2A) progenitors to differentiate toward astrocytes and inhibit oligodendroglial differentiation in a dose-dependent manner (56). Furthermore, Cheng et al., (2007) showed that spinal cord OPCs, which express BMP receptors, induce astrocytic differentiation in a dose-dependent manner and inhibit oligodendrocyte differentiation by increasing inhibitor of differentiation 4 (Id4) expression levels and down-regulating oligodendrocyte lineage transcription factors, Olig1 and Olig2 (57). ACVR1 mutations in DIPG and FOP are gain-of-function mutations in which the ACVR1/ALK2 protein is hyperactive. This results in the higher phosphorylation of Smad1/5/8 and, subsequently, to the over-expression of the inhibitor of differentiation genes. A significant number of DIPG cells express the astrocytic marker, Glial fibrillary acidic protein (GFAP). Interestingly, type 2 astrocytes generated from OPCs express both astrocytic marker GFAP and oligodendrocytic marker A2B2 (58). Moreover, patients with FOP disease show different neurologic symptoms. Kan et al., (2012) observed demyelinating lesions (suggesting the loss or dysfunction of oligodendrocytes) and inflammatory changes due to ACVR1 mutations in mouse models and patients in an MRI study (59). Therefore, ACVR1 mutations in DIPGs could deviate from the normal differentiation of OPCs towards an astrocytic fate.

Mouse model for $ACVR1^{+/G328V}$ mutation showed expression of this mutation in whole body led to mice death before birth reflecting major developmental anomalies (15). Expressing $ACVR1^{+/G328V}$ under control of Nes, as marker of neuroglia lineage did not show any significant anomalies. Expressing $ACVR1^{+/G328V}$ under control of Olig2 as master regulator of the oligodendroglia lineage, which previously has been suggested that Olig2 expressing cells as lineage of origin for DIPGs, showed mice born normal but some of them failed to gain normal weights and died (15). Surviving mice showed significant neurological anomalies, three weeks postnatal.

Tracing ACVR1$^{+/G328V}$ using ROSA26LSL-tdTomato reporter allele showed twice the number of oligodendroglial cells in the ventral brainstem of postnatal mice on days 7 and 21, which indicates an expansion of cells favored by ACVR1 mutation (15). Glial cells derived from mice models for ACVR1$^{+/G328V}$ showed higher levels of SMAD1 phosphorylation, which is due to the activation of BMP signalling. In addition, inhibition using the BMP pathway antagonist noggin and activin inhibitor follistatin did not change the expression of ID1/2/3 genes, which are induced by the ACVR1+/G328V mutation. Finally, these cells showed higher proliferation rates in comparison with the control cell population, Acvr1$^{+/+}$;Olig2$^{Cre/+}$ (15).

ID genes are able to induce cell proliferation by the negative regulation of cell cycle regulators or the indirect activation of E2F transcription factors by interrupting Rb function (60). So, Fortin et al., showed an upregulation of Ccna2 and Cdc25a in which their expression is controlled by E2F transcription factors in G1-to-S cell-cycle stage. This upregulation has been shown to be specific to ACVR1$^{+/G328V}$ glial cells and does not control cell populations (15).

Bulk transcriptomic analysis of ACVR1$^{+/G328V}$ and the control group (Acvr1$^{+/+}$;Olig2$^{Cre/+)}$ showed significant downregulation of mature oligodendrocyte marker genes, Cnp1, Mobp, Mog, and Opalin (Tmem10), in the presence of a ACVR1 mutation. Gene set enrichment analysis (GSEA) of RNA-seq data revealed the upregulation of genes involved in BMP signaling pathway and downregulation genes involved in oligodendrocyte differentiation (15). Despite the fact PDGFRA amplification rarely co-occurs with ACVR1 mutations, ACVR1$^{+/G328V}$ induces Pdgfra expression in Olig2 positive glial cell populations. In addition, PDGFRA staining of four ACVR1 mutant DIPGs showed the heterogeneous presence of PDGFRA in these tumors (15).

ACVR1$^{+/G328V}$ induces expression of Ascl1 and Sox11 transcription factors in postnatal day 7 of Acvr1floxG328V/+;Olig2Cre/+ mice brainstems (15). Previously, it has been shown that Ascl1 over-expression in adult glioblastoma induces neuronal signatures and inhibits glial differentiation (61).

In addition, it has been shown that expression of ACVR1$^{+/G328V}$ and Hist1h3bK27M in Olig2 context additively increases E2F transcription factor activity and leads to higher proliferation rate of cells (15). Finally, mice carrying both ACVR1$^{+/G328V}$ and Hist1h3b K27M in Olig2 context were not able

to form tumors. Adding Pik3cafloxH1047R/+ which is commonly co-occurring mutation with ACVR1 and H3.1K27M mutations, leads to tumor formation with high-grade diffuse gliomas characteristics.

Transcriptomic analysis showed there is increased expression of SOX11 and ASCL1 in DIPG patients in comparison to normal brain tissue. Generating isogenic cell models using CRISPR-Cas9 technology for SOX11 and ASCL1 transcription factors in SU-DIPG-XXXVI and HSJD-DIPG-007 cell lines showed the downregulation of PDGFRA acting as an oligodendrocyte progenitor regulator (15). An *in vivo* xenograft experiment using edited cell lines and their control groups (LentiCRISPRv2-GFP encoding a control sgRNA) showed longer survival rates and lower expressions of PDGFRA at the end point.

Expressing ACVR1 mutations and wildtype ACVR1 in the neurosphere of Nestin-Tv-a (Ntv-a);p53fl/fl mice (derived from postnatal day 3) showed an increase in BMP signaling activation in mutant cells with the most significant effect on the proliferation of and survival from the R206H mutation (14). Bulk transcriptomic analysis of ACVR1 R206H mutation alone or in the presence of H3.1K27M showed the same trend in the induction of genes involved in EMT and JAK/STAT3 signaling pathways. In the absence of H3.1K27M there are 24 genes significantly affected but in the presence of H3.1K27M this number increased to 2478 genes. In summary, ACVR1 mutations induce the mesenchymal signature, and it is dramatically enhanced in the presence of the H3.1K27M mutation. For example, mesenchymal genes, including CD44, TNC, and Snail2, were upregulated, whereas proneural and glial lineage regulator, Sox10, was downregulated (14). Previously, the role of STAT3 pathways has been shown in the induction mesenchymal signature in brain tumors (62). Authors have shown ACVR1 mutations can modestly induce STAT3 Y705 phosphorylation and its activation.

In vivo experiments in the astrocyte deficient for P53 showed ACVR1 mutations are not inducing glioma or glioma-like tumors (9). Nestin expressing brainstem progenitors with different ACVR1 mutations, including R206H, G328V and G328V in the absence of P53 and presence of H3.1K27M, were able to generate glioma-like lesions. It has been known that ACVR1 mutations are associated with mutations in the PI3K pathway, so that Ntv-p53fl/fl;PTENfl/f is added to ACVR1

and H3.1K27M mutations. Despite the formation of glioma-like lesions, these brainstem progenitors were not able to form glioma-like tumors (14).

The presence of Nestin and minimal presence of Olig2 was apparent through the staining of glioma-like lesions (14). Using DIPG biopsies, it has been shown that DIPGs with H3.1K27M and ACVR1 mutations are showing mesenchymal and pro-angiogenic gene expression signatures (63,64). Glioma-like lesions are expressing endothelial marker CD31 and mesenchymal marker CD44 genes (14). PDGFRA is known to play a role in tumorigenesis with H3.3K27M and P53 loss, resulting in the addition of PDGFA ligand to ACVR1 mutation and H3.1K27M in Nestin positive brain stem progenitors led to survival time of 70 days, which is significantly shorter than the median survival of the same cells in the absence of ACVR1 mutations (180 days) (14). Replacing H3.3K27M with H3.1K27M mutations in this context did not significantly change the survival rates of mice, which were shown to decrease survival time in the presence of ACVR1 mutations and the PDGFA ligand is not dependent on H3K27M mutations of different histone variants (14).

Hypothesis and aims:

Hypothesis 1. ACVR1 mutations are not sufficient to induce tumorigenesis and collaborate with H3K27M mutants to deviate normal program for development.

Aim 1: Remove ACVR1 and histone H3 mutations and generate isogenic lines using CRISPR-Cas9 to study *in vitro* differentiation and *in vivo* tumor formation using the xenograft model.

We will modify several patient derived cell lines (DIPG007, DIPG36, DIPG4, DIPG21) using CRISPR/Cas9 gene-editing technology, to generate isogenic cell lines with and without ACVR1 and histone mutations. Generated isogenic cell lines will be subject to the following experiments to address ACVR1's and histone H3's role in tumorigenesis:

First: Edited cell lines (ACVR1 mutation knockout and ACVR1 complete knockout, H3K27M-KO) with unedited CRISPRed clones and parental cell lines will be injected into the pons of mice to investigate the effect of these mutations on tumor formation *in vivo* using xenograft model. DIPG007 and DIPG36, previously shown to generate tumors in mice pons, will be used for this experiment. This experiment will address whether DIPG cell lines depend on ACVR1 mutation for tumor formation.

Second: *In vitro* investigation of ACVR1 and H3K27M effect on the transcriptome of DIPG cell lines and addressing their role in proliferation, migration and clone formation. Our generated isogenic lines using CRISPR technology will help to address these questions in the right cellular context for DIPGs.

Third: BMP signaling plays an important role in nervous system development and generation of astrocyte and oligodendrocytes. CRISPR isogenic cell lines for different ACVR1 mutations will provide a unique opportunity to assess the impact on differentiation. We will apply the Dirks differentiation protocol, in which growth factors will be removed gradually and BSA will be gradually added. Transcriptome analysis will be performed in order to check how ACVR1 affects differentiation pathways. In addition, stemness and differentiation markers will be assayed using immunofluorescence, western blotting, and qRT-PCR.

Hypothesis 2: H3.1K27M and H3.3K27M mutations have differential effects on the epigenome.

Aim 1: Targeting different patient derived cell types using CRISPR-Cas9 and over-expression systems to address different effects of H3.1- and H3.3-K27M mutations.

First: To investigate this question, patient derived cell lines were subjected for mass spectrometry and ChIP-seq experiments. Different histone post translational marks (PTMs), including H3K27me3, H3K27me2, H3K27ac, H3K36me3, and H3K36me2 were assessed using ChIP-seq. The same cell lines were used to generate mass spectrometry data for histone PTMs. But due to significant heterogeneity of these cell lines, we used CRISPR-Cas9 to generate K27M-knockout isogenic lines. Previously, several H3.3K27M-KO cell lines, including BT245, DIPG13, HSJ19, and HSJ31 were generated and recently we generated three cell lines with H3.1K27M-knockout, DIPG36, DIPG4, and DIPG21. These cell lines will be subjected to the same ChIP-seq experiments for candidate marks based on the mass spectrometry and ChIP-seq analysis of parental cell lines, including K27ac, K27me2, and K36me2. Transcriptome analysis using RNA-seq analysis will be conducted to see differences in gene expression profile and over-lapping with ChIP-seq experiments.

Second: To investigate whether these epigenetic differences are caused by histone H3.1- and H3.3-K27M mutations or cell of origin, we are conducting over-expression of H3.1K27M mutations in wild type and H3.3K27M-knockout cell lines. To this aim, lentivirus particles carry H3.1K27M and H3.1 WT used for infection of G477 cell line (wildtype cell line for histone mutations), BT245 and DIPG13 (as H3.3K27M-knockout cell lines). After confirmation by western blot, generated cell will be profiled using ChIP-seq and mass spectrometry experiments for K27ac, K27me2, and K36me2 marks. RNA-seq data will help to identify gene expression changes across different cell lines and the effect of mark differences between H3.1 and H3.3K27M on gene expression program.

Chapter 2

Material and methods

Patient samples and clinical information

This study was approved by the Institutional Review Board of the respective institutions from which the samples were collected. We thank Keith Ligon and Michelle Monje, and Angel Montero Carcaboso for generously sharing primary tumor cell lines established from patients with high-grade glioma.

Cell culture

Tumor-derived cell lines HSJD-DIPG007, SU-DIPGIV, and SU-DIPGXXXVI were maintained in NeuroCult NS-A proliferation media (StemCell Technologies) supplemented with bFGF (10 ng/mL) (StemCell Technologies), rhEGF (20 ng/mL) (StemCell Technologies), and heparin (0.0002%) (StemCell Technologies).Tumor derived cell lines BT869 and SF10693 were maintained in TSM media which contains Neurobasal-A Medium (1X) (Invitrogen Cat no:10888-022), D-MEM/F-12 (Invitrogen Cat no:11330-032), HEPES buffer solution (1M, Invitrogen Cat no:15630-080), MEM Sodium Pyruvate solution (100X, Invitrogen Cat no:11360-070), GlutaPlus , NeuroCult^{TM} SM1 neuronal supplement (StemCell Technologies Cat no: 05711), H-EGF (Shenandoah Biotech Cat no: 100-26), H-FGF-basic-154 (Shenandoah Biotech Cat no: 100-146), H-PDGF-AA (Shenandoah Biotech Cat no: 100-16), H-PDGF-BB (Shenandoah Biotech Cat no: 100-18), Heparin solution (StemCell Technologies Cat no: 07980). All patient derived cell lines were seeded on plates coated in poly-L-ornithine (0.01%) (Sigma) and laminin (0.01 mg/mL) (Sigma).

Lentiviruses for H3.3K27M and H3.1K27M were gifts from Dr. Peter Lewis. Lentiviruses expressing H3.3-H3.3-K27M and H3.1K27M were applied for 24 h and G418 (Wisent) selection (500 ng/mL) was maintained for the duration of growth. Retrovirus expressing ACVR1-R206H and ACVR1 wildtype (control) were applied on NPCs. NPCs expressing ACVR1-R206H and ACVR1 wildtypes received from Dr. Charles stiles.

CRISPR/Cas9 genome editing

pSpCas9(BB)-2A-GFP (PX458) was a gift from Feng Zhang (Addgene plasmid # 48138).

ACVR1 guide was designed to target exon 6 of ACVR1 gene overlapping with R206H mutation. CRISPR-Cas9 editing was carried out as described in (65,66). Constructs were transfected with

lipofectamine 3000 (Thermo Fischer Scientific) or nucleofection kit for human stem cells according to the manufacturer's protocol. Flow cytometry sorted single GFP + cells in 96-well plates, 48 to 72-h post-transfection. Clones were kept in 96 well plates for two to five weeks (cell line dependent) to provide enough time for single cells to form clones. DNA was extracted from clones. Designed primer for exon 6 of ACVR1 was used to screen clones by PCR and Sanger sequencing. Selected clones were screened by Illumina MiSeq system for the target exon to confirm complete knockout of the ACVR1 mutated allele or complete knockout of both mutated and wildtype alleles (Fig 2.1).

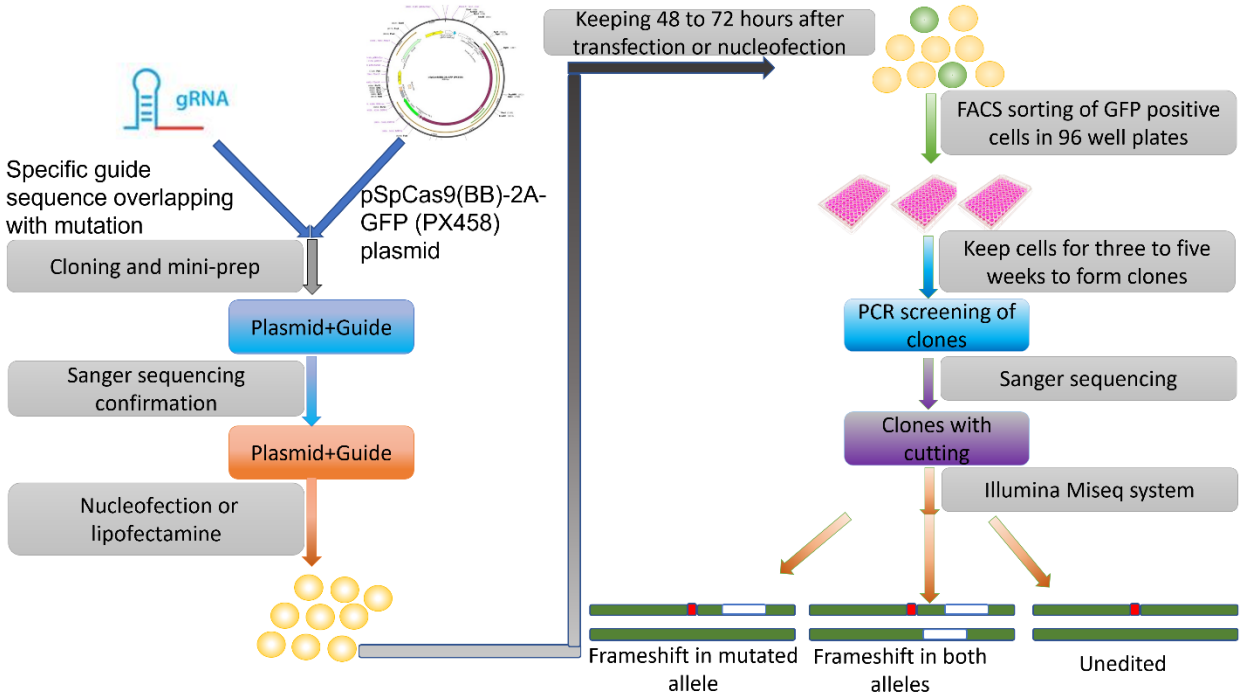

Figure 2. 1. Generation of isogenic CRISPR edited cells for ACVR1 R206H and G328E/V mutations using primary DIPG cell lines.

Schematic representation of the CRISPR editing strategy used in this study. CRISPR guide was used to target exon 6 of ACVR1 gene and K27M mutations in HIST1H3B and H3F3A genes. Positive clones were sorted as single cell using FACS for isogenic clones. ACVR1 sequences were checked on all isogenic clones using sanger and Illumina Miseq sequencings.

Western blotting

Cells were lysed for 1 hour using RIPA buffer (home-made) supplemented with complete, mini, EDTA-free proteinase inhibitor cocktail tablets (Roche). Histone lysates were extracted using Histone Extraction Kit (Abcam, ab113476). Protein amounts were quantified using PierceTM BCA Assay Kit (ThermoFisher Scientific). Thirty micrograms of whole cell lysates (1 microgram for histone lysates) were separated on 10% Mini-PROTEAN TGX Stain-Free Precast Gels (Bio-Rad) and transferred onto PVDF membranes for one hour. Blocking was then performed using 5% skim milk or 5% Bovine Serum Albumin (BSA) in Tris-buffered saline (50mM Tris, 150mM NaCl, pH 7.4, 0.1% Tween 20) (TBST) for one hour at room temperature. Membrane were incubated in the presence of the relevant antibody overnight at 4 degrees in 5% milk/BSA in TBST: Anti-p21 (1:200, Santa Cruz sc-6246), anti-Beta-tubulin (1:5000), anti-PDGFRA (1:2000). Membranes were washed three times with TBST prior to incubation with Horse Radish Peroxidase-linked secondary antibodies in 3% milk/BSA for one hour at room temperature: anti-mouse, anti-rabbit. Membranes underwent a final three-rounds of washes with TBSA before the signal was developed with Amersham ECL Prime Western Blotting Detection Reagent (GE Healthcare). Finally, signals were visualized using ChemiDoc MP Imaging System (Bio-Rad).

Cell proliferation assays

Cell lines were plated at low confluency at 15000 cells in 24-well plates. Cell proliferation was assessed using IncuCyte ZOOM System real-time instrumentation (Essen BioScience). Phase contrast was used to assess confluency and 16 images were taken every three hours for each well. Particles smaller than 400 μm^2 were removed from analysis. All confluency data were extracted and normalized to starting point. For CRISPR edited clones, at least two clones were compared with parental cell lines with at least three biological replicates. Patient derived cell lines BT869, HSJD-DIPG007, SU-DIPGIV, SU-DIPGXXXVI, and SF10693 cell lines and ACVR1 edited clones were treated with Activin A (20 ng/mL) and BMP6 (20 ng/mL). In the case of treatment with M4K2009, cells were plated at 15000 cells per well in 24 well plate in quadruplets. BT869 and HSJD-DIPG007 were treated with 3.5uM M4K2009 or vehicle DMSO. SU-DIPGIV and SU-

DIPGXXXVI were treated with 5uM M4K2009 or vehicle DMSO. Proliferation was assessed over 5 days. All experiments were done in triplicate and results are expressed as the average of three independent experiments.

Colony formation assay

Parental cells and isogenic clones were plated in duplicates on laminin coated 6 well plates at 500 cells per well. Cells were left for 10 days until the appearance of visible clones. In the case of treatment with M4K2009, SU-DIPGXXXVI cells were incubated with 5uM M4K2009 or vehicle DMSO for all the duration of the experiment. Cells were then fixed with 4% formalin, washed in PBS, and stained with 0.5% crystal violet. The number of clones was counted in each well and averaged for each duplicate. Final counts are expressed as the average for three independent experiments.

Cell-cycle analysis

To determine cell-cycle distribution, $1x10^6$cells were plated in 6-well plates. Forty eight hours later cells were washed in ice-cold PBS, fixed in 70% ethanol and stored at -20•C until use. Cells were then centrifuged and labeled with 0.5mL of FxCycle PI/RNase Staining Solution (catalog no: F10797, Thermo Fisher), according to manufacturer's instruction. Cell-cycle distribution was determined using BD FACSCanto II cytometer (Becton Dickinson) and analyzed with FlowJo Software (Treestar).

Apoptosis analyses were performed using the FITC Annexin V Apoptosis Detection Kit I (catalog no: 556547, BD Biosciences) following the manufacturer's protocol. Briefly, a total of $5x10^5$ cells were plated. Following 48h incubation, supernatant and trypsinized cells were collected. After washing in ice-cold 1X PBS, cells were resuspended in 1X Binding Buffer. Then 5µl of FITC Annexin V and 5µl PI were added to cells and incubated for 15 min at RT in the dark. 400µl of 1X Binding Buffer to each tube and FACS analysis was performed with FACSCanto II cytometer (BD Biosciences) within 1 hour.

DNA synthesis was measured with Click-iT EdU Flow Cytometry Assay Kit (C10425, Thermo Fisher) according to the manufacturer's protocol. Briefly, 40k cells were plated in 6-well plates. Three hours before harvesting, cells were incubated with 10µM 5-ethynyl-2'-deoxyuridine (EdU). Cells

were then washed in ice-cold PBS, fixed, and then incubated with Click-IT reaction buffer for 30 minutes, protected from light. Cells were then washed and FACS analysis was performed with FACSCanto II cytometer (BD Biosciences).

Cell differentiation assay and immunofluorescence

Patient derived cell lines were treated with 14% fetal bovine serum for two weeks (67–69) or with BMP4 (20ng/ml) and CNTF (20ng/ml) for one week (70). Magistri et al., 2016 used BMP4 (10ng/ml) and CNTF (20ng/ml) to differentiate cells toward astrocyte fate but our experiments revealed higher response to BMP4 at 20ng/ml, so we have modified protocols to optimize it for DIPG cell lines. Cells were then fixed with 45 paraformaldehyde and 15% sucrose for 15 minutes. Cells were permeabilized with 0.1% Triton X-100 and incubated in blocking bluffer containing BSA 2% and normal goat serum 2%. Cells were then incubated overnight at 4C with the primary antibodies GFAP, CD44, OLIG2, and NES. AlexaFluor 594 or 488 were used as secondary antibodies at 1/5000 for one hour at room temperature. Slides were mounted and images were taken using confocal microscope.

Immunohistochemistry (IHC)

Harvested PDOX tissues were immediately fixed in 10% formalin overnight and embedded in paraffin. Samples were cut at 5µm, placed on SuperFrost/Plus slides (Fisher) and dried overnight at 37°C, before IHC processing.

After de-paraffinization and EDTA epitope retrieval, sections were incubated with the primary antibody (Rabbit monoclonal H3.3 K27M (RM192, 31-1175-00, RevMab Bioscience) diluted in 1:600. The slides were then loaded onto the Ventana Discovery Ultra Instrument (Ventana Medical Systems).

Slides were counterstained with Hematoxylin (catalog no: 760-2021, 5266726001, Roche) and Bluing Reagent (catalog no: 760-2037, 5266769001, Roche), washed, dehydrated through graded alcohols, cleared in xylene, and mounted with mounting medium Leica CV 5030 coverslipper. Sections were scanned using the Aperio AT Turbo Scanner (Leica Biosystems). IHC was performed at the Histology Platform from RI-MUHC.

Quantitative PCR

Quantitative PCR (qPCR) was performed to assess expression level of cell cycle, developmental and stemness related genes. Total RNA was extracted from parental, unedited, ACVR1 edited clones from BT869, HSJD-DIPG007, SU-DIPGIV, and SU-DIPGXXXVI primary cell lines using the miRNeasy mini kit (Qiagen) according to manufacturer's instructions with purity and integrity assessed utilizing Nanodrop (Thermo-Fisher) and Experion (Biorad) methodologies. 100 ng of RNA was used for reverse-transcription using the iScript RT Supermix (BioRad) following manufacturer's instructions. We have used previously confirmed from PrimeTime qPCR Primer Assays source (IDT). Real-time PCR for CDKN1A, CDKN2B, CCND2, GFAP, CD44, and GAPDH as reference gene was done on the generated cDNA from 3 biological replicates for each experimental condition. Samples were run on a Lightcycler 96 (Roche) with the SsoFast Evagreen SuperMix kit (BioRad). Cycling conditions were: 95°C for 30 sec followed by 40 cycles 95°C for 5sec/60°C for 20 sec. Fold change values were calculated utilizing the 2−ΔΔCt method with GAPDH expression and parental cells used as the calibrator, comparing each treatment group to the parental as control group.

Drug sensitivity assay

Cells were plated at a density of 3000 cells per well on laminin coated 96 well plates. They were treated with an increasing dose of ACVR1 inhibitors, ranging from 0 to 10uM. DMSO was used as a vehicle control. Cells were incubated with the drugs for 5 days and media was changed on the third day. In order to assess cell viability, Alamar blue (ThermoFisher scientific, #DAL1100, Waltham, MA USA) was added on cells on the 5th day for 6 hours and absorbance at 570nm and 600nm was determined using i-Control microplate reader software by Tecan. Ratio of cell viability was calculated according to the following formula for measuring cytotoxicity and proliferation:

Percentage difference between treated and control cells

$\frac{(O2*A1)-(O1*A2)}{(O2*P1)-(O1*P2)} * 100$ where:

O1 = molar extinction coefficient (E) of oxidized Alamar Blue (Blue) at 570 nm (80586)

O2= E of oxidized Alamar Blue at 600 nm (117216)

A1 = absorbance of test wells at 570 nm

A2 = absorbance of test wells at 600 nm

P1 = absorbance of positive growth control well (cells plus Alamar Blue but no test agent) at 570 nm

P2 = absorbance of positive growth control well (cells plus Alamar Blue but no test agent at 600 nm

Graphs were plotted using Graphpad software using mean of three different replicates. Bars represent standard error of means.

In vivo mouse xenografts

All mice were housed, bred and subjected to listed procedures according to the McGill University Health Center Animal Care Committee and were in compliance with the guidelines of the Canadian Council on Animal Care. Female NOD.Cg-Prkdc^{scid} mice (4-6 weeks) were used for xenograft experiments (Jackson Laboratory). For brain orthotopic injection, mice were injected with HSJD-DIPG007 and BT869 parental lines and isogenic ACVR1 KO clones at a density of 7.10^5 cells in the pons: 1) HSJD-DIPG007 parental cells (n=10), 2) HSJD-DIPG007 unedited Clone C5 (n=5), 3) HSJD-DIPG007 ACVR1 KO clone C8 (n=5), 4) HSJD-DIPG007 ACVR1 KO Clone C9 (n=5), 5) BT869 parental cells (n=8), 6) BT869 ACVR1 KO clone C8 (n=5), 7) BT869 ACVR1 KO clone C10 (n=5). The Robot Stereotaxic machine from Neurostar was used for stereotaxic injections using the following coordinates for the pons: anteroposterior: -4.5mm, mediolateral: 0.8mm, dorsoventral: 4.5mm. Mice were continuously monitored for neurological symptoms of brain tumors: weight loss, epilepsy, altered gait, lethargy. They were euthanized immediately when clinical endpoint is reached.

The brains were removed and put in formalin for histology.

For subcutaneous injections, SU-DIPGIV and SU-DIPGXXXVI parental cells and respective isogenic clones, were prepared in Matrigel:PBS (1:1) (Matrigel basement membrane matrix, phenol red free, LDEV free, Corning, #356237, New York, USA), and 4.10^6 cells were implanted in the left flank of female NOD.Cg-Prkdc^{scid} mice (4-6 weeks): 1) SU-DIPGIV parental cells (n=3), SU-DIPGIV ACVR1 KO clone C103 (n=3), 3) SU-DIPGIV ACVR1 clone C122 (n=3), 4) SU-DIPGXXXVI parental cells (n=3), 5) SU-DIPGXXXVI ACVR1 KO clone C104 (n=3), SU-DIPGXXXVI ACVR1 KO clone C120 (n=3). Tumor volume was measured twice per week using a caliper and mice were euthanized when tumor volume reached 1.5cm^3.

Kaplan Meir curve for mice survival was generated using the Graphpad software. Mice that died due to a tumor are considered as 1. Those that were still surviving at the end of the experiment, or those that were euthanized for different reasons that are related to tumor formation were considered as 0.

RNA-seq

Total RNA was extracted from freshly harvested cells of parental/unedited and ACVR1 edited cell using the Aurum Total RNA Mini Kit (Bio-Rad Cat no: 732-6820) according to instructions from the manufacturer. Ribosomal RNA (rRNA) depleted during Library preparation according to instructions from the manufacturer (Epicentre) to achieve greater coverage of mRNA and other long non-coding transcripts. Paired-end sequencing (100 bp) was performed on the Illumina Nova-seq platform.

Analysis of RNA-seq data

RNA-seq datasets were processed using the RNA-seq module of GenPipes (71) (v3.1.2 for tumours and parental cell lines, v3.1.0 for isogenic cell lines). Briefly, raw reads were trimmed using Trimmomatic v0.32 (72) to remove adaptor and sequencing-primer associated reads, then aligned to hg19 using STAR (73) and generates Binary Alignment Map file (.bam). PCR duplicate reads as defined by reads with identical mapping coordinates were then collapsed by Picard (v2.0.1) to produce uniquely aligned reads. Differential gene expression analysis has been done using DESeq (74) and EdgR (75) packages and their results reported in the single merge file. Genes

with log-fold change >1 and adjusted pvalue<0.05 were considered as differentially expressed genes (DEGs).

Gene ontology analysis was done using g:Profiler web server and the results were filtered based on the adjusted-*p-value* (76). To generate two dimensional PCA we used the built-in R function prcomp and ploted using ggplot2 package in R.

Single sample gene set enrichment analysis

To assess developmental gene programs in cell line data, a reference set of 191 gene signatures from published scRNA-seq atlases (Jessa et al. 2019) spanning embryonal day 12.5 to postnatal day 6 of the murine forebrain and hindbrain/pons and 17W–19W of the fetal human telencephalon (69). 100 gene signatures containing cell identity specific genes were used as reported in the original study. Gene set enrichment analysis (GSEA) was performed with these gene sets as input, on genes from the bulk RNA-seq sample set ranked by the Negative Binomial Wald test statistic from differential expression analysis, using the fgsea package (v1.8.0) (77). With fgsea, leading edge genes were obtained, and normalized enrichment scores (NES) were computed by normalizing enrichment to the average enrichment of 10,000 random gene samples. *P-values* were adjusted using the Benjamini-Hochberg procedure; signatures with adjusted *p-value* < 0.01 were considered significantly enriched or depleted.

In addition to mentioned data set and method, we have used single samples gene set enrichment analysis (ssGSEA) implanted in GenePattern 2.0 (78). To perform ssGSEA we used two gene lists including DEGs derived from 73 cell types (clusters) from mouse brains and spinal cords from Rosenberg et al., (2018) (79) to study lineage differentiation events in CRISPR edited clones.

ChIP sequencing

Sample and library preparation

Experimental procedures for chromatin immunoprecipitation and sequencing (ChIP-seq) are similar to those described in (32,80).

Cells were fixed with 1% formaldehyde (Sigma). Fresh frozen tumor tissue samples were homogenized using mortar and pestle while tissue was still frozen, then fixed with 1% formaldehyde. Fixed cell preparations were washed, pelleted and stored at -80°C. Sonication of lysed nuclei (lysed in a buffer containing 1% SDS) was performed on a BioRuptor UCD-300 for 60 cycles, 10s on 20s off, centrifuged every 15 cycles, chilled by 4°C water cooler. Samples were checked for sonication efficiency using the criteria of 150-500bp by gel electrophoresis. After the sonication, the chromatin was diluted to reduce SDS level to 0.1% and before ChIP reaction 2% of sonicated drosophila S2 cell chromatin was spiked-in the samples for quantification of total levels of histone mark after the sequencing (see below).

ChIP reaction for histone modifications was performed on a Diagenode SX-8G IP-Star Compact using Diagenode automated Ideal ChIP-seq Kit. 25ul Protein A beads (Invitrogen) or 70ul of sheep anti-mouse IgG beads (Invitrogen) were washed and then incubated with antibodies (protein A beads with: anti-H3K27me3 (1:40, CST 9733), anti-H3K27me2 (1:50, CST 9728)), and 2 million cells of sonicated cell lysate combined with protease inhibitors for 10 hr, followed by 20 min wash cycle with provided wash buffers.

Reverse cross linking took place on a heat block at 65°C for 4 hr. ChIP samples were then treated with 2ul RNase Cocktail at 65°C for 30 min followed by 2ul Proteinase K at 65°C for 30 min. Samples were then purified with QIAGEN MiniElute PCR purification kit as per manufacturers' protocol. In parallel, input samples (chromatin from about 50,000 cells) were reverse crosslinked and DNA was isolated following the same protocol.

Library preparation was carried out using Kapa HTP or HyperPrep Illumina library preparation reagents. Briefly, for HTP kit, 25ul of ChIP sample was incubated with 45ul end repair mix at 20°C

for 30 min followed by Ampure XP bead purification. A tailing: bead bound sample was incubated with 50ul buffer enzyme mix for 30°C 30 min, followed by PEG/NaCl purification. Adapter ligation: bead bound samples were incubated with 45ul buffer enzyme mix and 5ul of different TruSeq DNA adapters (Illumina) for each sample, at 20°C for 15 min, followed by PEG/NaCl purification (twice). Library enrichment: 12 cycles of PCR amplification. Size selection was performed after PCR using a 0.6x/0.8x ratio of Ampure XP beads (double size selection) set to collect 250-450bp fragments.

For HyperPrep kit, end-repair and A tailing were performed in one reaction: 15ul of ChIP sample was incubated with 45ul end repair+A-tailing mix at 20°C for 30 min, then 65°C for 30 min. Directly proceeded to adapter ligation by adding 5ul of IDT for Illumina Unique Dual Indexes (IDT) adapters and 45ul ligation buffer enzyme mix, incubating at 20°C for 15 min, followed by Ampure XP bead purification. Library enrichment: 10 cycles of PCR amplification. Size selection was performed after PCR using a 0.6x/0.8x ratio of Ampure XP beads (double size selection) set to collect 250-450bp fragments.

ChIP libraries were sequenced using Illumina HiSeq 2000, 2500 or 4000 at 50bp single reads or Illumina NovaSeq 6000 at 50bp paired-end reads (one read used in the analysis for compatibility).

Read processing and alignment

ChIP-seq datasets were processed using the ChIP-seq module of GenPipes (71) (v3.1.2 for tumours and parental cell lines, v3.1.0 for isogenic cell lines). Briefly, raw reads were trimmed using Trimmomatic v0.32 (72) to remove adaptor and sequencing-primer associated reads, then aligned to hg19 or mm10 using bwa-mem (v0.7.12) (81) with default parameters. PCR duplicate reads as defined by reads with identical mapping coordinates were then collapsed by Picard (v2.0.1) to produce uniquely aligned reads. Reads with a mapping quality of 5 or less were then filtered. For single-end (SE) 50bp datasets, reads were extended by 250bp.

Data analysis and signal quantification for tumours and parental cell lines

Wiggle tracks are generated using uniquely aligned reads using Homer (v4.9.1) (82). RPKM was calculated using VisRSeq (v0.9.40) (83) or SeqMonk (v1.46) at annotated genes. Promoter is

defined as a 5kb bin centered on the transcription start site. Median values were generated for promoter-associated H3K27me3 and H3K27ac in each tumour group. Z-score was calculated from the median RPKM as

$$z - score = \frac{(mutant\ median\ RPKM\ -\ WT\ median\ RPKM)}{\sqrt{(mutant\ median\ RPKM + \ WT\ median\ RPKM)}}$$

|Z-score| > 0.5 were designated as significant changes for ChIP-seq datasets.

Data analysis and signal quantification for isogenic cell lines

ChIP-Rx (ChIP with reference exogenous genome) is a technique which applies spike-in Drosophila chromatin as internal control. For each ChIP-seq profile, we calculated the ChIP-Rx ratio (denoted as Rx) as follows:

$$Rx = \frac{s/s\_dmel}{i/i\_dmel},$$

where *s* is the percentage of reads mapped to human genome in the target sample, *s_dmel* is the percentage of spike-in Drosophila genome in the sample, and similarly *i* and *i_dmel* are defined for the input sample. ChIP-seq RPKM values over CGIs and genome-wide 100kb bins for scatterplots were calculated using VisRSeq (v0.9.40) (83). Rx- and RPKM-normalized BigWig tracks were produced using the "bamCoverage" functionality of deeptools (84) (v3.5.1). Rx ratios were supplied via the '--scaleFactor' option. Reads flagged as duplicates, mapping to random, mitochondrial or sex chromosomes, as well as low-mappability regions according to ENCODE's blacklist (85) were discarded. The resulting tracks were visualized using the Integrative Genomic Viewer (86).

To quantify the relative levels of H3K27ac across the genome, the number of reads (scaled using ChIP-Rx ratio) over 1Mb window was determined using HOMER. The read count over repeat families (DNA, LINE, SINE and LTRs) was determined similarly using HOMER. The Repeatmasker annotation for hg19 was retrieved from UCSC table browser.

H3K27me2 broad domain calling

The broad domain calling procedure was adapted from Weinberg et al. Nature 2019 and Harutyunyan et al. Cell Reports 2020 (87,88). Briefly, the abundance of H3K27me2 and corresponding input samples was quantified by binning the genome into 1 kb bins, counting the number of unique reads in each bin (using the 'featureCounts' function of the 'Rsubread' R package) (v2.4.2) (89,90), and normalizing them to library depth. Enrichment of the mark in each bin was calculated as IP/input, and empty bins were given a score of 0. The bins were then segmented based on mean enrichment scores using the PELT method, SIC penalty, and a Z-test through the 'changepoint' R package (Killick et al. Journal of Statistical Software 2014) (v2.2.2) (91). Only segments with sufficient enrichment of the mark (mean score > 1) and length ($\geq$ 50 kb) were retained.

To obtain H3K27M-specific domains in each isogenic line, we called consensus domains across H3K27M replicates (using the 'intersect' functionality of 'bedtools') (v2.29.2) (92). Intervals overlapping domains identified in any corresponding KO replicate were then subtracted (using the 'bedtools subtract'). The reciprocal procedure was used to derive KO-specific domains, i.e. consensus KO domains were identified, and domains overlapping corresponding H3K27M replicates were subtracted.

Enhancer and core-regulatory circuitry analysis

H3K27ac ChIP peaks were identified using MACS2 (93) with a p-value threshold of 1e-9. The ROSE algorithm was used to identify enhancers and superenhancers (SEs) (94).The aggregated H3K27ac binding signals across all H3.1 and H3.3K27M pons samples respectively were determined using ROSE2_META (https://github.com/linlabcode/pipeline/blob/master/ROSE2_META.py). The peaks within +/- 2.5 kb of transcription start site (TSS) were excluded and enhancers within the distance of 12.5 kb were stitched together. The resulting enhancers were ranked by the aggregated H3K27ac signal, and the enhancers above the inflection point were defined as SEs. The SEs were then assigned to the nearest genes. To compare the enhancer landscapes, the fold change of H3K27ac signals between H3.1 and H3.3K27M pons samples for each enhancer was calculated and ranked.

Core regulatory circuitry (CRC) of SE-associated transcription factors were inferred by scanning for TF motifs in SEs. A list of expressed genes in H3.1 and H3.3K27M pontine samples respectively, along with the called SEs were used as input for mapping the regulatory networks using CRC mapper (https://github.com/linlabcode/CRC). This approach used motif scanning, performed using FIMO, to infer number of interacting TF motifs in the proximal SE of a TF (in-degree) and number of SE-associated TFs containing a binding motif for the TF (out-degree). The resulting networks were used to determine the change in in-degree and out-degree between the H3.1 and H3.3K27M pontine samples.

Histone modification quantification with nLC-MS

The complete workflow for histone extraction, LC/MS, and data analysis was recently described in detail. Briefly, cell pellets (approx. 1x106 cells) were lysed on ice in nuclear isolation buffer supplemented with 0.3% NP-40 alternative. Isolated nuclei were incubated with 0.4 N H2SO4 for 3 hours at 4˚C with agitation. 100% trichloroacetic acid (w/v) was added to the acid extract to a final concentration of 20% and samples were incubated on ice overnight to precipitate histones. The resulting histone pellets were rinsed with ice cold acetone + 0.1% HCl and then with ice cold acetone before resuspension in water and protein estimation by Bradford assay. Approximately 20 µg of histone extract was then resuspended in 100 mM ammonium bicarbonate and derivatized with propionic anhydride. 1 µg of trypsin was added and samples were incubated overnight at 37˚C. After tryptic digestion, a cocktail of isotopically-labeled synthetic histone peptides was spiked in at a final concentration of 250 fmol/µg and propionic anhydride derivatization was performed a second time. The resulting histone peptides were desalted using C18 Stage Tips, dried using a centrifugal evaporator, and reconstituted using 0.1% formic acid in preparation for nanoLC-MS analysis.

nanoLC was performed using a Thermo ScientificTM Easy nLCTM 1000 equipped with a 75 µm x 20 cm in-house packed column using Reprosil-Pur C18-AQ (3 µm; Dr. Maisch GmbH, Germany). Buffer A was 0.1% formic acid and Buffer B was 0.1% formic acid in 80% acetonitrile. Peptides were resolved using a two-step linear gradient from 5% to 33% B over 45 min, then from 33% B

to 90% B over 10 min at a flow rate of 300 nL/min. The HPLC was coupled online to an Orbitrap Elite mass spectrometer operating in the positive mode using a Nanospray Flex™ Ion Source (Thermo Scientific) at 2.3 kV. Two full MS scans (m/z 300-1100) were acquired in the orbitrap mass analyzer with a resolution of 120,000 (at 200 m/z) every 8 DIA MS/MS events using isolation windows of 50 m/z each (e.g. 300-350, 350-400…650-700). MS/MS spectra were acquired in the ion trap operating in normal mode. Fragmentation was performed using collision-induced dissociation (CID) in the ion trap mass analyzer with a normalized collision energy of 35. AGC target and maximum injection time were 10e6 and 50 ms for the full MS scan, and 10e4 and 150 ms for the MS/MS can, respectively. Raw files were analyzed using EpiProfile.

Chapter 3

Results

Chapter 3.1

ACVR1 exerts different mechanisms in H3.1 and H3.3K27M contexts to induce tumorigenesis in diffuse intrinsic pontine gliomas

ACVR1 mutations confer differential responses to BMP signaling in H3.1 and H3.3 K27M DIPGs

To better evaluate the status of ACVR1 mutations in DIPGs, we analyzed previously published data (whole genome and whole exome sequencing) on pediatric high-grade glioma (pHGG) and DIPGs (5) and classified DIPGs on the basis of ACVR1 mutations. ACVR1 mutations prevail in DIPGs harboring the canonical H3.1K27M (67%), rather than H3.3K27M (18%) and histone wild type (15%). A more in depth classification of DIPGs based on the mutated residues shows that the ACVR1 R206H mutation preferentially segregates with H3.3K27M DIPGs, whereas H3.1K27M DIPGs present with a wider range of ACVR1 mutations mainly affecting codons 328 (Gly328Val (G328V) or Gly328Glu (G328E)), 356 (Gly356Asp (G356D)), and 256 (Arg256Gly (R256G)) (Fig 3.1A) (7,8,10,95). Other mutations such as *PI3CA/PI3KR1* and *TP53* also co-occur with H3K27M (Fig 3.1A).

Since ACVR1 encodes the ALK2 receptor, and mutations in ACVR1 results in a ligand-independent activation of this receptor (96–98), we asked whether the different ACVR1 mutations differentially affect BMP signaling pathways in H3.3 and H3.1K27M DIPG cells. We first examined the basal expression of phospho-SMAD1/5 (pSMAD1/5) in a panel of DIPGs. We found that DIPGs carrying ACVR1 mutations have an increased basal expression of pSMAD1/5 compared to ACVR1-WT DIPGs, where basal pSMAD1/5 expression is very low (Fig 3.S1A). Stimulation of DIPGs with BMP6 induces the activation of ALK2 receptor in ACVR1-WT and potentiates the activity of ACVR1 mutant DIPGs denoted by a further increase in pSMAD1/5 expression (Fig 3.S1B). In line with these differences, transcriptomic analysis of BMP signaling pathway genes also demonstrates that these genes are differentially expressed in H3.3K27M ACVR1$^{+/\ R206H}$ cell lines (BT869 and HSJD-DIPG007) and H3.1K27M ACVR1$^{G328E/V}$ cell lines (SU-DIPGIV and SU-DIPGXXXVI) (Fig 3.S1D). Mutations in ACVR1 in FOP confer an abnormal response of the receptor to activin A, a TGF-beta ligand that normally acts as an antagonist to BMP receptors (53,54,99). Activin A similarly activates the BMP signaling pathway only in DIPGs harboring ACVR1 mutations but not in the ACVR1-WT DIPGs (Fig 3.1B). We next sought to determine the effects of the abnormal signaling responses to BMPs and activin A *in vitro*. BMP6 and activin A decrease the proliferation of H3.3K27M/ACVR1$^{+/R206H}$ cells, BT869 and HSJD-DIPG007 but have no effect on H3.1K27M/ACVR1$^{+/G328E/V}$ cells, SU-DIPGIV and SU-DIPGXXXVI (Fig 3.1C). We speculated that the

abnormal response to activin A was a result of the ACVR1 R206H mutation as previously described in FOP (53,54,99). To confirm this hypothesis, we used the CRISPR-Cas9 system to generate isogenic clones in which the entire ACVR1 gene or only the mutated allele was removed from the DIPG primary cell lines. Interestingly, knocking out ACVR1 completely abrogated the effect of activin A on proliferation and inhibited pSMAD1/5 activation (Fig 3.1D, 3.1E, 3.S1C) further confirming that ACVR1 R206H mutation confers the abnormal behavior of the receptor. Surprisingly, activin A does not change the proliferation of the DIPG cell line SF10693, which harbors an $ACVR1^{+/R206H}$ mutation in a H3.1K27M background, suggesting that the effect of activin A on proliferation is context dependent and is related to the presence of H3.3K27M (Fig 3.1F). Taken together, these results show that ACVR1 mutations elicit different responses to BMP signaling in H3.1 and H3.3K27M DIPGs, which might underlie differential dependency and tumorigenic mechanisms.

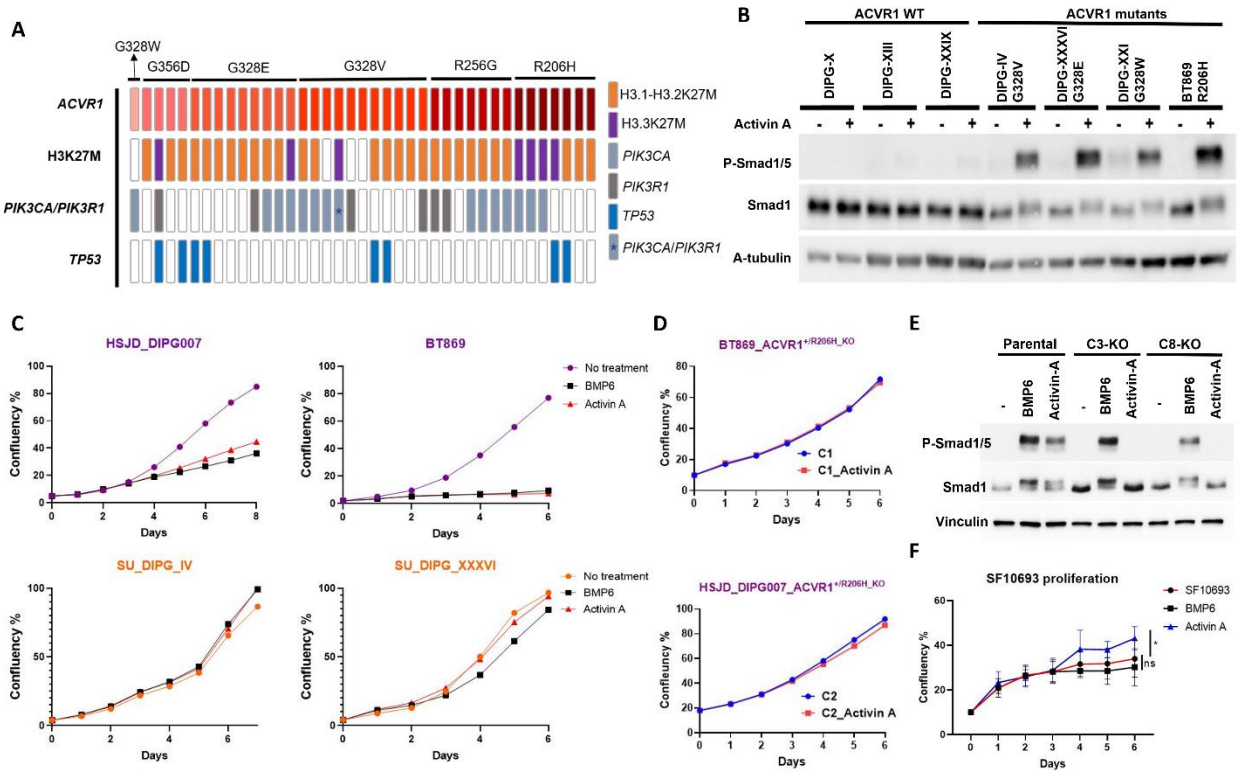

Figure 3. 1. ACVR1 mutations differentially co-segregate with histone mutations and respond differently to BMP ligands.

(A) Analysis of DIPGs harboring ACVR1 mutations (n=39) and their co-occurrence with other main mutations in DIPGs. **(B)** Western blot analysis for P-Smad1/5 protein expression in DIPG cell lines with or without ACVR1 mutations in response to Activin A (20ng/ml for 1 hour). **(C)** Proliferation capacity of ACVR1 mutant primary DIPG cell lines in response to BMP6 (20 ng/ml) or Activin A (20 ng/ml). Cell proliferation was quantified using Incucyte® S3 Live-Cell Analysis System over 6-8 days. **(D)** Proliferation capacity of BT869 and HSJD-DIPG007 parental and isogenic CRISPR edited cell lines (BT869$^{+/R206H\text{-}KO}$ ansHSJD-DIPG007$^{+/R206H\text{-}KO}$) in response Activin A to (20 ng/ml). Cell proliferation was quantified using Incucyte® S3 Live-Cell Analysis System over 6 days. **(E)** Western blot analysis of P-Smad1/5 protein expression in HSJD-DIPG007 parental cells and isogenic CRISPR edited (HSJD-DIPG007$^{+/R206H\text{-}KO}$) in response to Activin A (20 ng/ml) and BMP6 (20 ng/ml). **(F)** Proliferation of SF10693 DIPG cell line harboring H3.1K27M and ACVR1$^{+/R206H}$ mutations in response to Activin A (20 ng/ml) and BMP6 (20 ng/ml) using Incucyte® S3 Live-Cell Analysis System over 6 days.

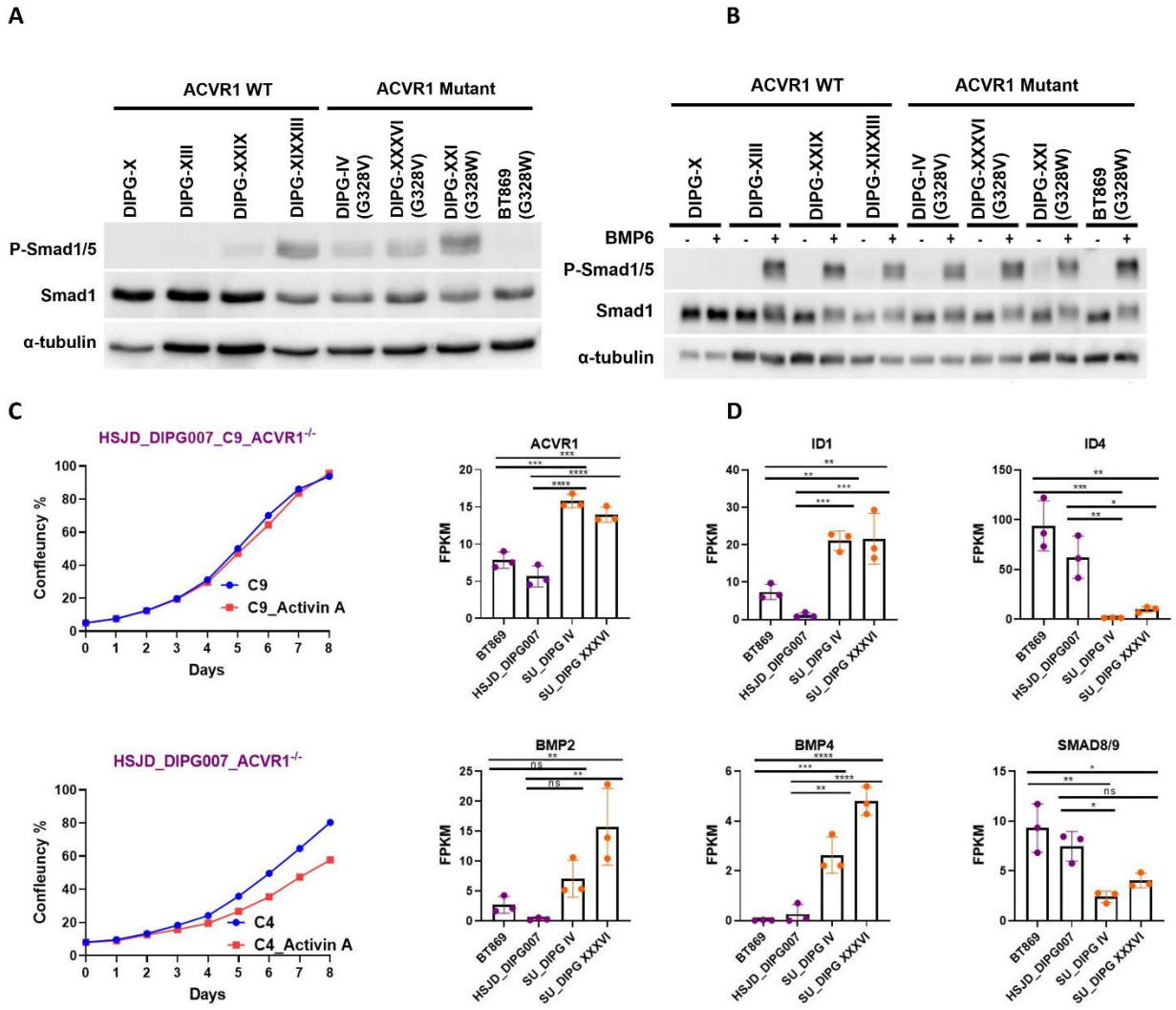

Figure 3.S1. BMP signaling pathway activity in primary DIPG cell lines.

(A) Basal P-Smad1/5 protein detected by western blot analysis in primary DIPG cell lines harboring ACVR1 mutations and not in ACVR1 wild type cell lines. **(B)** Western blot analysis of P-Smad1/5 activity in DIPG cell lines treated with BMP6 (20 ng/ml) for 1 hour. **(C)** Cell proliferation analysis of HSJD-DIPG007 parental and isogenic ACVR1 edited clones in response to Activin A (20 ng/ml) using Incucyte® S3 Live-Cell Analysis System over 8 days. **(D)** ACVR1$^{+/G328E/V}$ H3.1 K27M and ACVR1$^{+/R206H}$ H3.3K27M cell lines show different gene expression of BMP signaling pathway components, at the level of the ligands (BMP2 and BMP4), receptor (ACVR), effector (SMAD8/9), and down-stream target genes (ID1 and ID2). Orange indicates ACVR1$^{+/G328E/V}$ (H3.1K27M) and purple indicates ACVR1$^{+/R206H}$ (H3.3K27M) mutated cell lines in all panels.

Table 3. 1. List of ACVR1 mutated cells have been used to generate isogenic clones using CRISPR-Cas9 strategy.

Purple color is showing H3.3K27M mutated cell lines with ACVR1 R206H mutation and orange indicates H3.1K27M cell lines with ACVR1 G328E/V mutations.

Nr	Cell line	Histone mutation	Gene	Mutation	Edited
1	HSJD-DIPG007	H3.3K27M	ACVR1	R206H	R206H-KO
2	HSJD-DIPG007	H3.3K27M	ACVR1	R206H	ACVR1-KO
3	HSJD-DIPG007	H3.3K27M	ACVR1	R206H	Unedited
4	BT869	H3.3K27M	ACVR1	R206H	R206H-KO
5	BT869	H3.3K27M	ACVR1	R206H	ACVR1-KO
7	BT869	H3.3K27M	ACVR1	R206H	Unedited
9	SU-DIPG-IV	H3.1K27M	ACVR1	G328V	ACVR1-KO
11	SU-DIPG-IV	H3.1K27M	ACVR1	H3.1K27M	Unedited
12	SU-DIPG-XXXVI	H3.1K27M	ACVR1	G328E	ACVR1-KO
14	SU-DIPG-XXXVI	H3.1K27M	ACVR1	H3.1K27M	Unedited

DIPGs harboring H3.3K27M and ACVR1$^{+/R206H}$ mutations resemble neural progenitor cells

Studies aiming at investigating the differences between H3.1K27M and H3.3K27M tumors segregate these two groups into two distinct entities, showing clear differences at the transcriptomic, genomic, methylation, and enhancer profiles (5,42,100). In agreement with these findings, our RNA-seq analysis also separated H3.1K27M and H3.3K27M cells into two different clusters (Fig 3.2A). Gene ontology analysis further demonstrates distinct pathway enrichment with H3.3K27M cell lines expressing genes involved in nervous system development and neuronal differentiation, whereas H3.1K27M cell lines express genes implicated in extracellular matrix organization, response to cytokines, and blood vessel development (Fig 3.2B). These differences are also translated into changes in gene expression. Indeed, H3.3K27M cell lines (BT869 and HSJD-DIPG007) show an enrichment in genes implicated in neural progenitor cell development (*OLIG2, NES, SOX2,* and *MYC*), whereas H3.1K27M cells (SU-DIPGIV and SU-DIPGXXXVI) are enriched with genes involved in cell-cell adhesion and extracellular matrix organization (*COL6A3*, *COL1A1*, *TWIST2*) (FPKM>1) (Fig 3.2C). We also confirmed the expression of the neural progenitor cell markers, Nestin and Olig2, in H3.3K27M DIPG lines but not in H3.1K27M DIPGs (Fig 3.2D). These differences in gene expression and GO pathway analysis suggest that H3.1 and H3.3K27M DIPGs emerge from a different cell of origin.

The expression of neural stem cell genes in H3.3K27M DIPG cell lines led us to speculate that they more closely resemble neural progenitor cells (NPCs) and to further investigate this hypothesis, we asked whether H3.3K27M DIPGs are capable of differentiating into glial cells when exposed to differentiation factors. Fetal bovine serum (FBS) is a potent inducer of astrocytic differentiation of hiPSCs and neural progenitor cells (70,101). Our results also demonstrate that H3.3K27M DIPG cell lines grown in FBS for two weeks showed an increased expression of GFAP (Fig 3.2E, 3.S2B). However, H3.1K27M cell lines were unable to differentiate into glial cells under these same conditions (Fig 3.2E, 3.S2A). Given the well-studied role of BMPs in astrocyte differentiation, we also stimulated H3.3K27M and H3.1K27M DIPGs with BMP4 (20 ng/ml) and CNTF (20 ng/ml) (70,101). Similar to FBS, BMP4 and CNTF induced astrocytic differentiation only

in H3.3K27M DIPGs, denoted by an increase in GFAP expression, but not in H3.1K27M DIPGs (Fig 3.S2B). The ability of H3.3K27M cell lines to differentiate to astrocytes closely recapitulates the differentiation of neural stem cells to astrocytic lineage in response to BMPs. When stimulated with BMPs, NPCs lose the expression of stem cell markers (*OLIG2, NES,* and *SOX2*) and acquire the astrocytic marker GFAP (Fig 3.2F and 3.S2C). We then asked whether the effect of the ACVR1 mutation on BMP signaling would also impact signaling in NPCs. To this end, we used lentiviral expression vectors to create stable transformants NPCs expressing either the wild type protein, or R206H, or G328V mutations. NPCs overexpressing G328V mutation were unable to grow which prevented us from pursuing any further work on them. Overexpression of ACVR1 R206H mutations resulted in a basal increase in pSMAD1/5 expression in NPCs, as well as an increase in BMP signaling in response to BMP6 and activin A, similar to what was observed in ACVR1 mutated DIPGs (Fig 3.2G and 3.2H), whereas parental NPCs and NPCs overexpressing WT ACVR1 did not respond to activin A (Fig 3.2H). Signaling responses to BMP6 correlate with a dose dependent decrease in proliferation in both normal NPCs and NPCs harboring the R206H mutation, but a dose dependent response to activin A was exclusively observed in NPCs carrying the R206H mutation (Fig 3.2J, 3.S2D). Taken together these results confirm the previous findings that H3.1K27M and H3.3K27M DIPGs constitute separate entities and that ACVR1 mutations in part contribute to the differential behavior in these two contexts. In addition, the different ACVR1 mutations (R206H and G328V) play an important role in the response of these cells to BMP signaling and their lineage commitment.

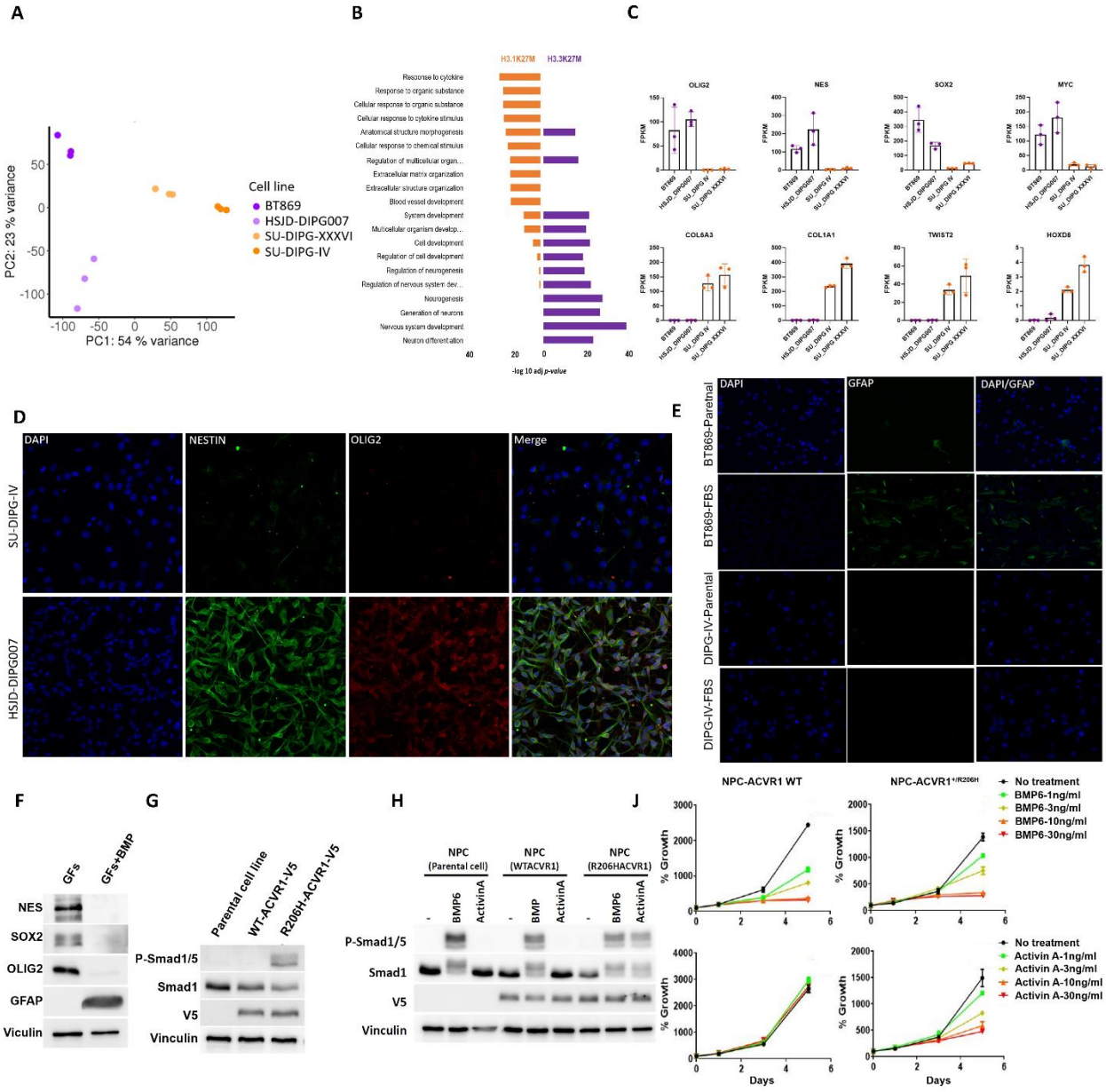
A
PC2: 23 % variance
PC1: 54 % variance
Cell line
BT869
HSJD-DIPG007
SU-DIPG-XXXVI
SU-DIPG-IV
B
H3.1K27M
H3.3K27M
Response to cytokine
Response to organic substance
Cellular response to organic substance
Cellular response to cytokine stimulus
Anatomical structure morphogenesis
Cellular response to chemical stimulus
Regulation of multicellular organ...
Extracellular matrix organization
Extracellular structure organization
Blood vessel development
System development
Multicellular organism develop...
Cell development
Regulation of cell development
Regulation of neurogenesis
Regulation of nervous system dev...
Neurogenesis
Generation of neurons
Nervous system development
Neuron differentiation
-log 10 adj p-value
C
OLIG2
NES
SOX2
MYC
COL6A3
COL1A1
TWIST2
HOXD8
FPKM
D
DAPI
NESTIN
OLIG2
Merge
SU-DIPG-IV
HSJD-DIPG007
E
DAPI
GFAP
DAPI/GFAP
BT869-Paretnal
BT869-FBS
DIPG-IV-Parental
DIPG-IV-FBS
F
GFs
GFs+BMP
NES
SOX2
OLIG2
GFAP
Viculin
G
Parental cell line
WT-ACVR1-V5
R206H-ACVR1-V5
P-Smad1/5
Smad1
V5
Vinculin
H
NPC (Parental cell)
NPC (WTACVR1)
NPC (R206HACVR1)
BMP6
ActivinA
BMP
P-Smad1/5
Smad1
V5
Vinculin
J
NPC-ACVR1 WT
NPC-ACVR1+/R206H
% Growth
Days
No treatment
BMP6-1ng/ml
BMP6-3ng/ml
BMP6-10ng/ml
BMP6-30ng/ml
Activin A-1ng/ml
Activin A-3ng/ml
Activin A-10ng/ml
Activin A-30ng/ml

Figure 3. 2. DIPGs harboring different ACVR1 mutations show distinct transcriptomic and regulatory profile based on the histone variant mutation, H3.1 or H3.3K27M.

(A) Bulk RNA-seq analysis performed on four mutant parental cell lines (n=3 for each cell line). All samples have been generated in the same batch. 10000 most variable genes were used for PCA analysis. **(B)** Gene ontology analysis using g: Profiler (Padj<0.05) was performed to filter significant pathways differentially regulated in H3.1 and H3.3K27M DIPGs. Orange and purple colors are showing H3.1K27M and H3.3K27M enriched processes respectively. **(C)** Bulk RNA-seq analysis for neural and oligodendrocyte progenitors, cell matrix component and regulators across four primary cell lines. Orange and purple colors are showing H3.1K27M and H3.3K27M enriched gene expression respectively. **(D)** Representative immunofluorescence images for Oligodendrocyte Transcription Factor 2 (OLIG2) and Nestin (NES) expression in H3.1K27M and H3.3K27M DIPGs. **(E)** Differentiation potential of H3.1 and H3.3K27M cells after subjection to differentiation media containing 10% FBS in the absence of EGF and FGF for two weeks. Representative immunofluorescence images for the expression of the astrocytic marker Glial fibrillary acidic protein (GFAP) in BT869 and SU-DIPGIV cells. **(F)** Western analysis for the protein expression of NES, SOX2 OLIG2, GFAP in neural progenitor cells. Vinculin was used as loading control. **(G)** Western blot analysis for P-Smad1/5 protein expression in NPCs expressing either wild-type or ACVR1 R206H using lentiviral expression vector. **(H)** Western blot analysis of P-Smad1/5 protein expression in NPCs expressing ACVR1 wildtype of ACVR1 R206H mutation in response to BMP6 (20 ng/ml) and Activin A (20 ng/ml). Note that the basal level of BMP signaling in the ACVR1 R206H line is modest relative to the ligand-treated samples and can only be visualized on immunoblot assays with high exposure times. **(J)** Dose-dependent growth arrest in response to BMP6 and Activin A in NPCs expressing either wildtype or ACVR1 R206H. Only the ACVR1 R206H line responds to Activin A. Cell proliferation was quantified using CellTiter Glo assay 5 days after treatment.

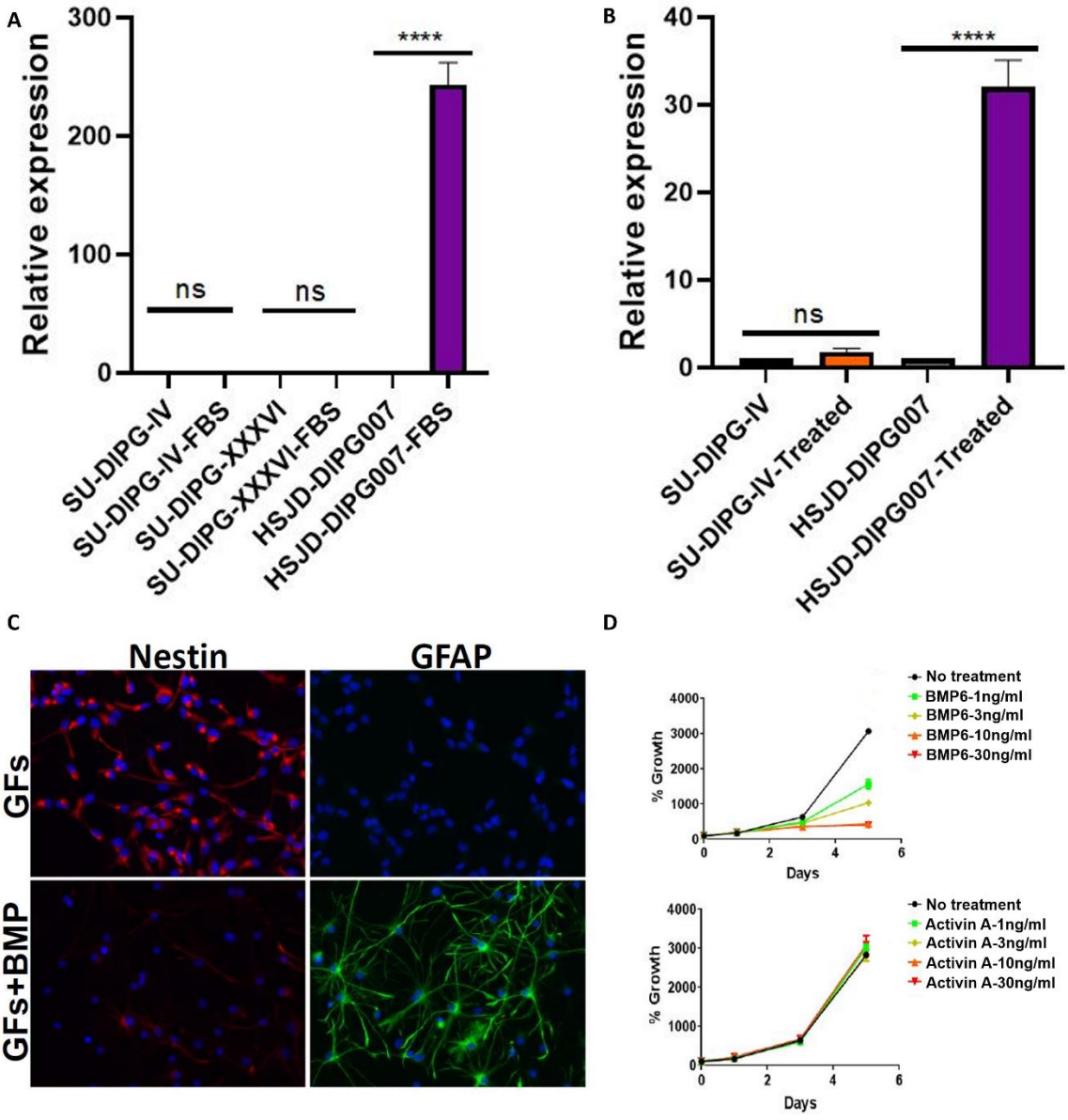

Figure 3.S2. ACVR1 mutations in H3.1K27M and H3.3K27M context show different transcriptome and lineage differentiation capacities.

(A) Differentiation of primary DIPG cells using 10% fetal bovine serum (FBS) for two weeks. qRT-PCR was used to assess GFAP expression level before and after differentiation. **(B)** Differentiation of primary DIPG cells using BMP4 (20 ng/ml) and CNTF (20 ng/ml) for seven days. qRT-PCR was used to assess GFAP expression level before and after differentiation. **(C)** Representative immunofluorescence images for NPCs expressing the astrocytic marker, GFAP after treatment

with BMPs. **(D)** Proliferation assay of NPCs in response to increasing doses of BMP6. NPCs do not respond to increasing doses of Activin A.

ACVR1 R206H mutation confers stem like properties to tumor cells in H3.3K27M DIPGs

In addition to the well-established differences between H3.1 and H3.3K27M at the genetic, epigenetic, and transcriptomic levels (63,100), our results also indicate that these two mutations exert differential responses to BMP signaling pathways. These findings, together with the preferential segregation of ACVR1 mutations towards distinct histone partners, prompted us to speculate that ACVR1 mutations play distinct roles in H3.1 and H3.3 K27M DIPGs. Our aforementioned results indicate that ACVR1 R206H mutation preferably partners with H3.3K27M in DIPGs. In order to better understand the role of this mutation, we performed RNAseq analysis on the two H3.3K27M ACVR1$^{+/R206H}$ DIPG cell lines, BT869 and HSJD-DIPG007 and their respective isogenic ACVR1 KO clones. Principle component analysis (PCA) for all expressed genes segregates parental cell lines and unedited clones from ACVR1 KO edited clones (Fig 3.S3A). Further analysis of the transcriptome shows that ACVR1 KO clones have higher expression of glial differentiation markers, whereas stem cell markers are more highly expressed in parental and unedited cell (Fig 3.3A, 3.S3B). Gene ontology analysis further confirms these findings whereby nervous system development and differentiation pathways are more significantly enriched in ACVR1 KO cells (Fig 3.3B, 3.S3C). We then used the single cell RNA-seq atlas for the pons and forebrain (69) to assess lineage changes upon removal of the ACVR1 gene or the R206H mutation from BT869 and HSJD-DIPG007 primary cells. Using this analysis, we show that removal of ACVR1 in BT869 cells led to the loss of oligodendrocyte progenitor cell markers and the acquisition of astrocytic-specific gene expression profile (Fig 3.3C). Concomitantly, an enrichment of astrocyte specific genes is observed in ACVR1 KO clones compared to parental and unedited cells (Fig 3.3C and 3.3D). Same results are also found in HSJD-DIPG007 (Fig 3.S3D). To provide more validations on our results, we have used gene sets derived from developing mouse brain and spinal cord (79) to conduct ssGSEA analysis for both BT869 and HSJD-DIPG007. ssGESA results were completely consistent for both cell lines in higher enrichment of astrocytic fate in ACVR1 edited clones in comparison

with parental and unedited controls (Fig 3.S4A. 3.4B, 3.4C, 3.S5A, 3.5B, and 3.5C). In addition, BT869 and HSJD-DIPG007 cells show changes in common astrocytic genes which further confirms cell lineage specificity of H3.3K27M and ACVR1 R206H DIPGs (Fig 3.S6A, 3.S6B). To further validate this finding, we performed immunofluorescence staining for the astrocytic markers GFAP and CD44, in BT869 parental cells and isogenic ACVR1 KO clones. Interestingly, we observe an increase in GFAP and CD44 expression in ACVR1 KO cells as well as phenotypic changes with elongated processes reminiscent of astrocytes (Fig 3.3E). It is worth noting that the effect of ACVR1 KO on glial differentiation was observed in the absence of any stimulation or differentiation media, showing that ACVR1 KO alone is sufficient to reprogram cells towards astrocytes. In addition to the upregulation of glial differentiation markers, GFAP and CD44, in ACVR1 KO compared to parental lines there is an increase in expression of the cell cycle inhibitor, CDKN1A/p21 (Fig 3.4A, 3.4B, 3.S6C, 3.S6D, and 3.S6E), and a decrease in the stemness markers PDGFRA (Fig 3.4A) and CSPG4/NG2 (Fig 3.4B) compared to parental cell lines. It is of note that these changes are more pronounced in BT869 cells compared to HSJD-DIPG007, denoting cell specific mechanisms that could account for the tumorigenic properties, although the ACVR1 R206H mutation exerts similar effects. These results imply that the ACVR1 R206H mutation prevents glial differentiation of H3.3K27M DIPGs leading to a reprogramming to a neural progenitor-like lineage.

Activation of BMP signaling in many cancer types enhances cell proliferation through the activation of Id genes and cell cycle regulators; besides, Id gene activation mediates the re-entry of quiescent cells into the G1-S phase (102–104). For this reason, we asked whether knocking out ACVR1 in BT869 and HSJD-DIPG007 cells would impact cell cycle progression in parallel with the decrease in stemness markers. Indeed, we observe an increased expression of the cell cycle inhibitor CDKN1A/p21 in both ACVR1 KO cell lines (Fig 3.4A, 3.S6E). In line with these findings, our FACS data show that ACVR1 KO cells show a reduction in the number of cells entering the S phase and EdU incorporation, compared to parental and unedited cells, denoting a decrease in cell proliferation (Figure 3.4C, 3.4D, and 3.S6F). These results suggest that ACVR1 R206H mutation blocks the ability of H3.3K27M DIPG cells to differentiate to astrocytes and maintains the cells in a stem cell like state which favors their proliferation and self renewal (Fig 3.4E).

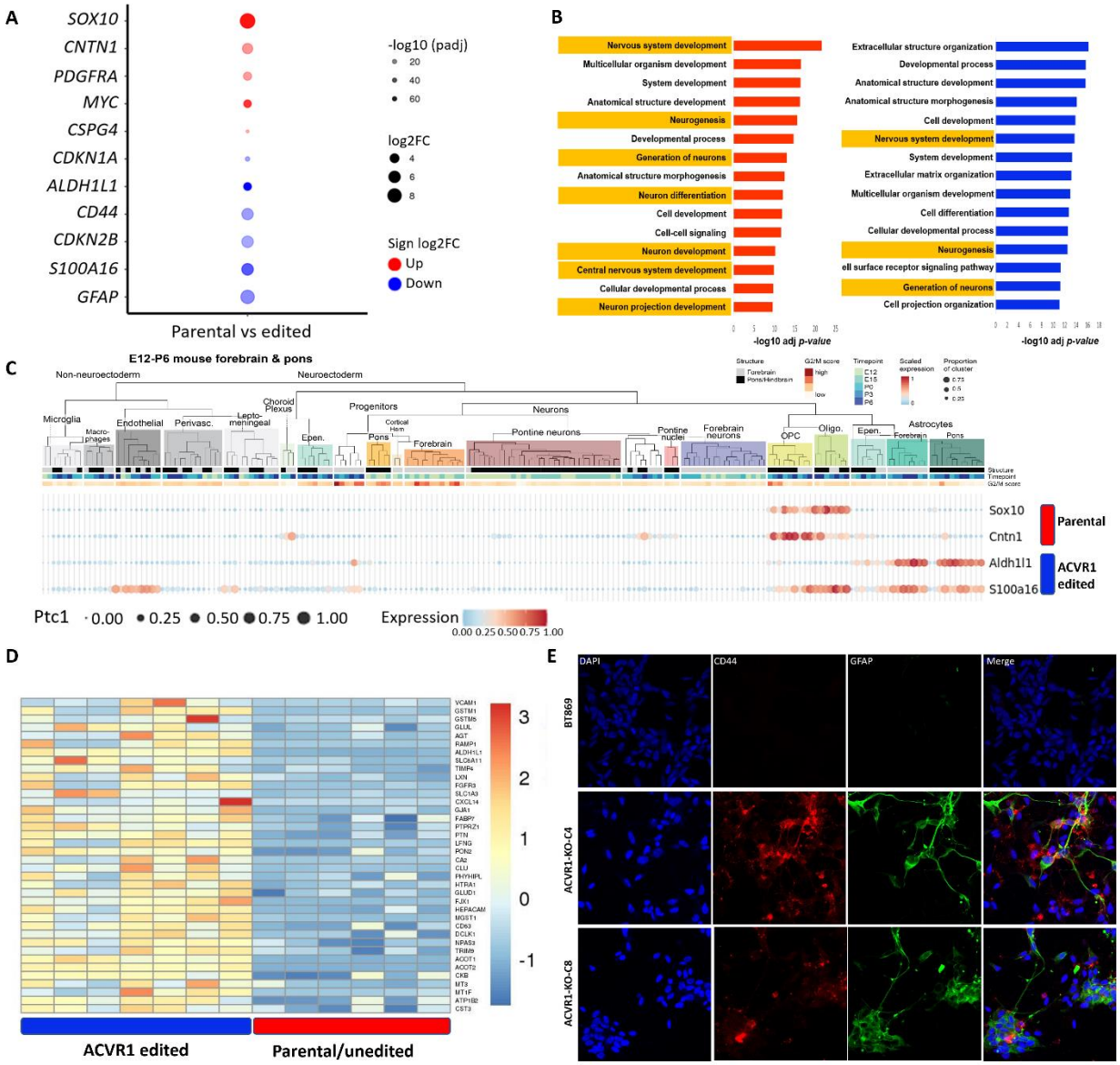
A
SOX10
CNTN1
PDGFRA
MYC
CSPG4
CDKN1A
ALDH1L1
CD44
CDKN2B
S100A16
GFAP
Parental vs edited
-log10 (padj)
20
40
60
log2FC
4
6
8
Sign log2FC
Up
Down
B
Nervous system development
Multicellular organism development
System development
Anatomical structure development
Neurogenesis
Developmental process
Generation of neurons
Anatomical structure morphogenesis
Neuron differentiation
Cell development
Cell-cell signaling
Neuron development
Central nervous system development
Cellular developmental process
Neuron projection development
-log10 adj p-value
Extracellular structure organization
Developmental process
Anatomical structure development
Anatomical structure morphogenesis
Cell development
Nervous system development
System development
Extracellular matrix organization
Multicellular organism development
Cell differentiation
Cellular developmental process
Neurogenesis
ell surface receptor signaling pathway
Generation of neurons
Cell projection organization
-log10 adj p-value
C
E12-P6 mouse forebrain & pons
Non-neuroectoderm
Neuroectoderm
Microglia
Macro-phages
Endothelial
Perivasc.
Lepto-meningeal
Choroid Plexus
Epen.
Progenitors
Cortical Hem
Pons
Forebrain
Neurons
Pontine neurons
Pontine nuclei
Forebrain neurons
OPC
Oligo.
Epen.
Astrocytes
Forebrain
Pons
Sox10
Cntn1
Aldh1l1
S100a16
Parental
ACVR1 edited
Ptc1
0.00
0.25
0.50
0.75
1.00
Expression
0.00 0.25 0.50 0.75 1.00
D
3
2
1
0
-1
ACVR1 edited
Parental/unedited
E
DAPI
CD44
GFAP
Merge
BT869
ACVR1-KO-C4
ACVR1-KO-C8

Figure 3. 3. Removal of R206H mutation from H3.3K27M DIPGs induces astrocytic differentiation of cells.

(A) Dot plot for BT869 unedited, complete ACVR1 KO, and ACVR1 R206H KO clones showing a drastic change in transcriptome. ACVR1 R206H and complete KO clones show a decrease in stemness genes (MYC, CSPG4/NG2, and PDGFRA) and an upregulation of astrocytic genes (GFAP and CD44), and cell cycle regulators (CDKN1A/P21 and CDKN2B/P15). **(B)** Gene ontology analysis using g: Profiler (Padj<0.05) were used to filter significant differential pathway regulation between parental/unedited and ACVR1 edited clones in BT869. **(C)** Cell lineage transition analyzed using the single-cell transcriptome atlas for pons and forebrain. ACVR1 edited cells acquire astrocytic gene expression signature in comparison to unedited controls that acquire an oligodendrocyte progenitor gene expression signature. **(D)** Heatmap of astrocytic specific gene expression profile derived from the single-cell transcriptome atlas analysis showing an overexpression of astrocytic genes in ACVR1 edited clones in comparison to parental/unedited cells. **(E)** Representative immunofluorescence images for the astrocytic markers GFAP and CD44 in BT869 parental cells compared to two distinct BT869 ACVR1-KO clones.

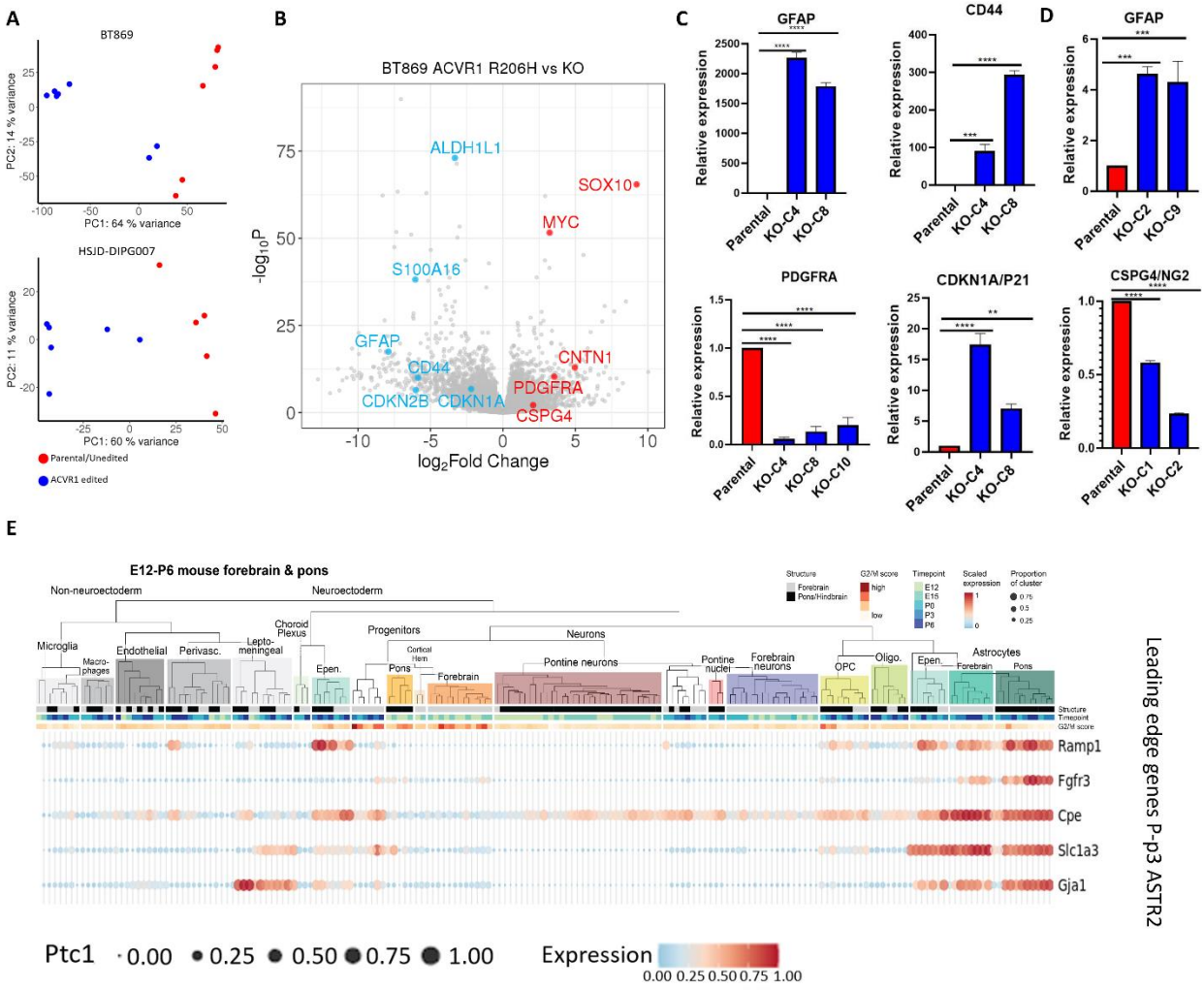
A
BT869
PC2: 14 % variance
PC1: 64 % variance
HSJD-DIPG007
PC2: 11 % variance
PC1: 60 % variance
Parental/Unedited
ACVR1 edited
B
BT869 ACVR1 R206H vs KO
-log10P
log2Fold Change
ALDH1L1
SOX10
MYC
S100A16
GFAP
CD44
CNTN1
CDKN2B
CDKN1A
PDGFRA
CSPG4
C
GFAP
CD44
PDGFRA
CDKN1A/P21
CSPG4/NG2
Relative expression
Parental
KO-C4
KO-C8
KO-C10
D
GFAP
Relative expression
Parental
KO-C2
KO-C9
CSPG4/NG2
Relative expression
Parental
KO-C1
KO-C2
E
E12-P6 mouse forebrain & pons
Non-neuroectoderm
Neuroectoderm
Microglia
Macro-phages
Endothelial
Perivasc.
Lepto-meningeal
Choroid Plexus
Epen.
Progenitors
Cortical Hem
Pons
Forebrain
Neurons
Pontine neurons
Pontine nuclei
Forebrain neurons
OPC
Oligo.
Epen.
Astrocytes
Forebrain
Pons
Structure
Forebrain
Pons/Hindbrain
G2/M score
high
low
Timepoint
E12
E15
P0
P3
P6
Scaled expression
Proportion of cluster
Ramp1
Fgfr3
Cpe
Slc1a3
Gja1
Ptc1
0.00
0.25
0.50
0.75
1.00
Expression
0.00 0.25 0.50 0.75 1.00
Leading edge genes P-p3 ASTR2

Figure 3.S3. Removal of R206H mutation from H3.3K27M DIPGs induces astrocytic differentiation of cells.

(A) Volcano plot for BT869 unedited, complete ACVR1 KO, and ACVR1 R206H KO clones showing a drastic change in transcriptome. ACVR1 R206H and complete KO clones show a decrease in stemness genes (MYC, CSPG4/NG2, and PDGFRA) and an upregulation of astrocytic genes (GFAP and CD44), and cell cycle regulators (CDKN1A/P21 and CDKN2B/P15). **(B)** PCA analysis of ACVR1 edited and parental/unedited cell lines (BT869 upper panel and HSJD-DIPG007 lower panel), showed significant changes in transcriptome and separation of CRISPR edited clones from unedited/parental cells in PCA1. Top 10000 most variable genes were used to generate PCAs. **(C, D)** qRT-PCR quantification of differentiation, stemness and cell cycle genes in BT869 parental and ACVR1 KO clones **(C)** and HSJD-DIPG007 parental and ACVR1 KO clones **(D).** For BT869 cells **(C)** astrocytic markers GFAP and CD44, stemness gene PDGFRA, and cell cycle marker CDKN1A/p21 are assessed. For HSJD-DIPG007 GFAP and the stemness marker CSPG4/NG2 are assessed. Red and blue are showing parental and edited clones respectively. **(E)** Cell lineage transition analyzed using single-cell transcriptome atlas from pons and forebrain. HSJD-DIPG007 ACVR1 KO cells acquire astrocytic gene expression signature but not the unedited controls.

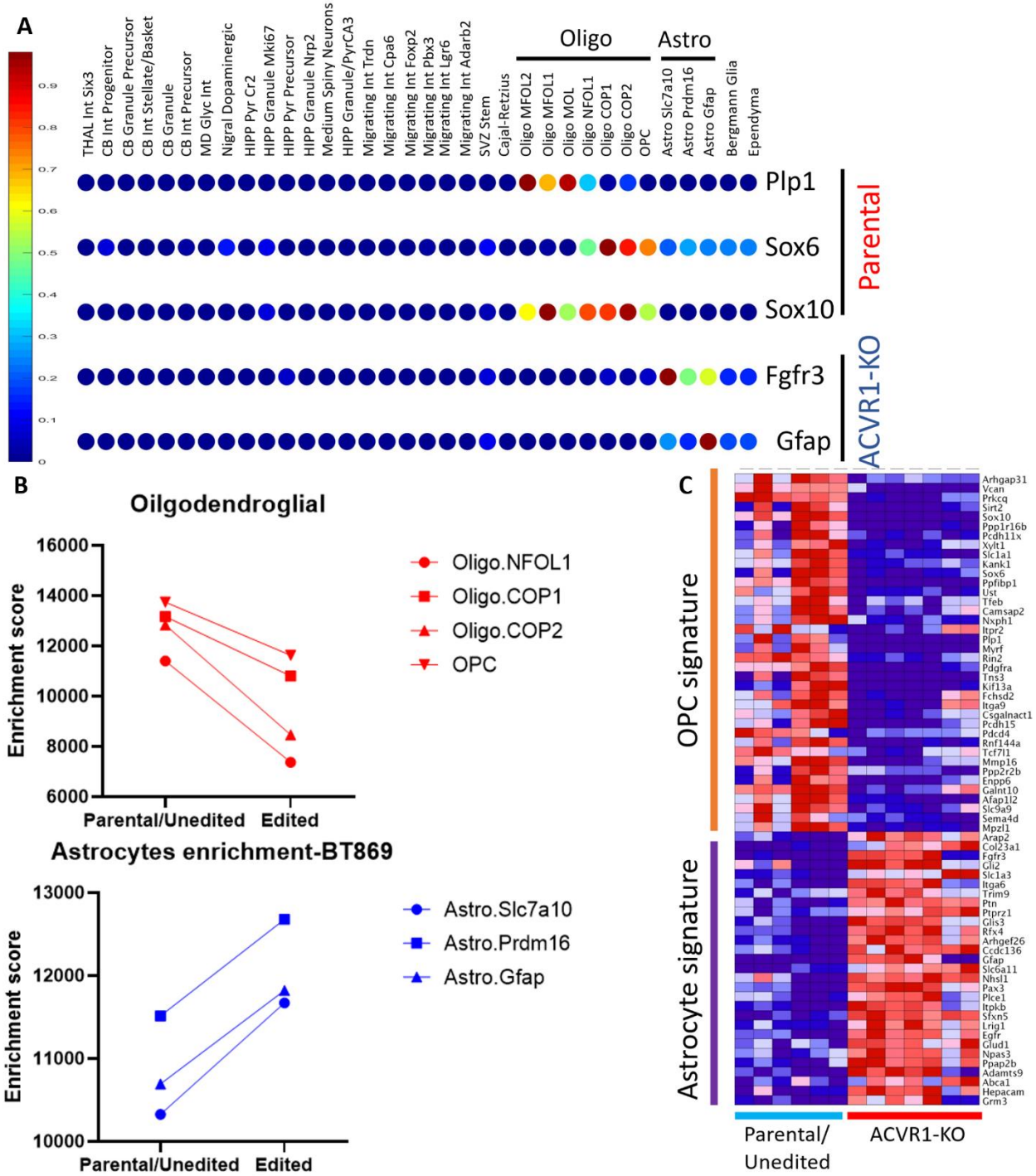
A
THAL Int Six3
CB Int Progenitor
CB Granule Precursor
CB Int Stellate/Basket
CB Granule
CB Int Precursor
MD Glyc Int
Nigral Dopaminergic
HIPP Pyr Cr2
HIPP Granule Mki67
HIPP Pyr Precursor
HIPP Granule Nrp2
Medium Spiny Neurons
HIPP Granule/PyrCA3
Migrating Int Trdn
Migrating Int Cpa6
Migrating Int Foxp2
Migrating Int Pbx3
Migrating Int Lgr6
Migrating Int Adarb2
SVZ Stem
Cajal-Retzius
Oligo MFOL2
Oligo MFOL1
Oligo MOL
Oligo NFOL1
Oligo COP1
Oligo COP2
OPC
Astro Slc7a10
Astro Prdm16
Astro Gfap
Bergmann Glia
Ependyma
Oligo
Astro
Plp1
Sox6
Sox10
Fgfr3
Gfap
Parental
ACVR1-KO
B
Oilgodendroglial
Enrichment score
Oligo.NFOL1
Oligo.COP1
Oligo.COP2
OPC
Parental/Unedited
Edited
Astrocytes enrichment-BT869
Astro.Slc7a10
Astro.Prdm16
Astro.Gfap
C
OPC signature
Astrocyte signature
Parental/ Unedited
ACVR1-KO

Figure 3.S4. Removal of R206H mutation from BT869 cell line induces astrocytic differentiation of cells.

(A and B) Cell lineage transition analyzed using the single-cell transcriptome from mouse brains and spinal cords from Rosenberg et al., (2018). ACVR1 edited cells acquire astrocytic gene expression signature in comparison to unedited controls that acquire an oligodendrocyte progenitor gene expression signature. **(C)** Heatmap of astrocytic specific gene expression profile derived from the single-cell transcriptome atlas analysis showing an overexpression of astrocytic genes in ACVR1 edited clones in comparison to parental/unedited cells.

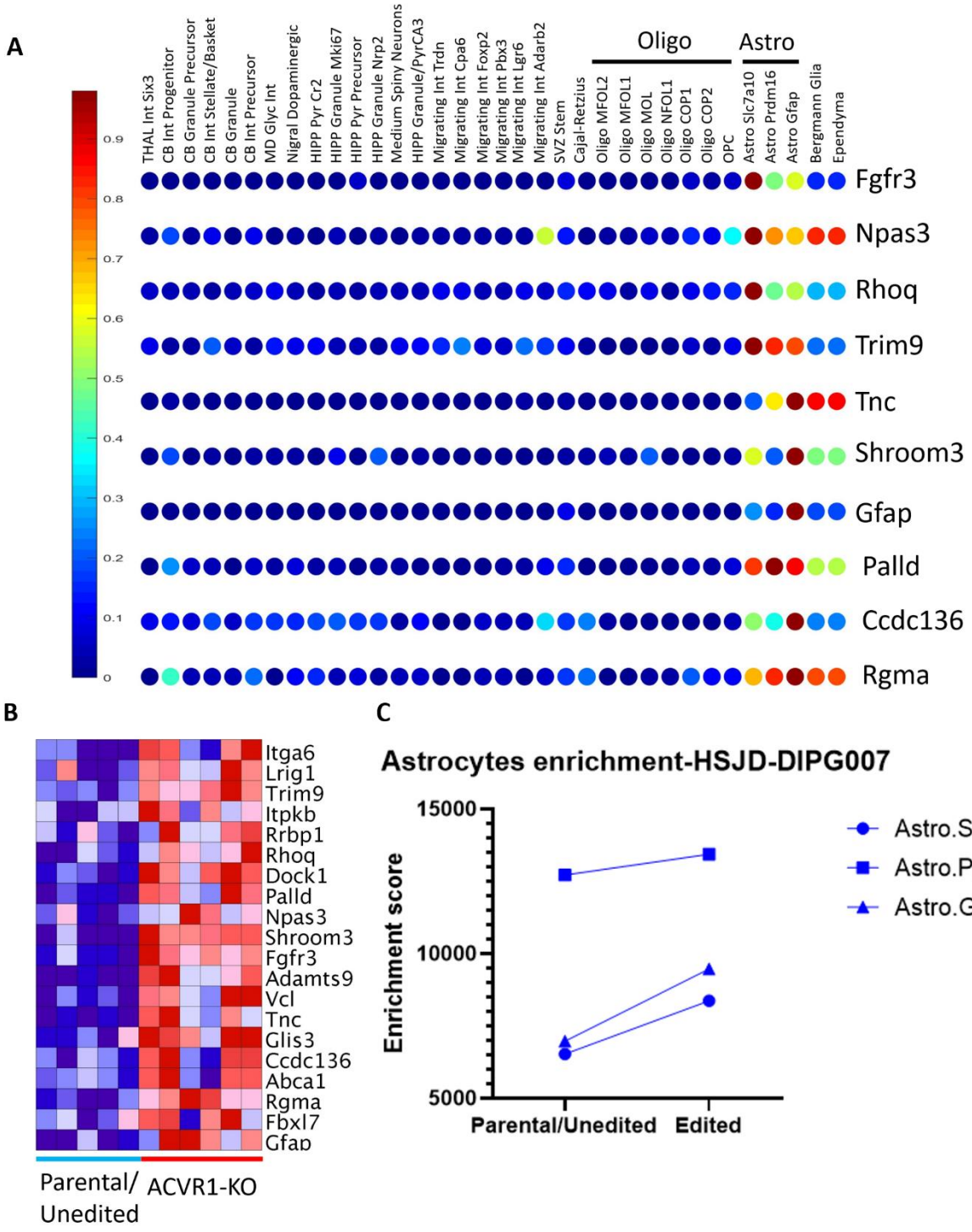
A
THAL Int Six3
CB Int Progenitor
CB Granule Precursor
CB Int Stellate/Basket
CB Granule
CB Int Precursor
MD Glyc Int
Nigral Dopaminergic
HIPP Pyr Cr2
HIPP Granule Mki67
HIPP Pyr Precursor
HIPP Granule Nrp2
Medium Spiny Neurons
HIPP Granule/PyrCA3
Migrating Int Trdn
Migrating Int Cpa6
Migrating Int Foxp2
Migrating Int Pbx3
Migrating Int Lgr6
Migrating Int Adarb2
SVZ Stem
Cajal-Retzius
Oligo
Oligo MFOL2
Oligo MFOL1
Oligo MOL
Oligo NFOL1
Oligo COP1
Oligo COP2
OPC
Astro
Astro Slc7a10
Astro Prdm16
Astro Gfap
Bergmann Glia
Ependyma
0.9
0.8
0.7
0.6
0.5
0.4
0.3
0.2
0.1
0
Fgfr3
Npas3
Rhoq
Trim9
Tnc
Shroom3
Gfap
Palld
Ccdc136
Rgma
B
Itga6
Lrig1
Trim9
Itpkb
Rrbp1
Rhoq
Dock1
Palld
Npas3
Shroom3
Fgfr3
Adamts9
Vcl
Tnc
Glis3
Ccdc136
Abca1
Rgma
Fbxl7
Gfap
Parental/ Unedited
ACVR1-KO
C
Astrocytes enrichment-HSJD-DIPG007
Enrichment score
15000
10000
5000
Parental/Unedited
Edited
Astro.Slc7a10
Astro.Prdm16
Astro.Gfap

Figure 3.S5. Removal of R206H mutation from HSJD-DIPG007 cell line induces astrocytic differentiation of cells.

(A) Cell lineage transition analyzed using the single-cell transcriptome from mouse brains and spinal cords from Rosenberg et al., (2018). ACVR1 edited cells acquire astrocytic gene expression signature in comparison to unedited controls that acquire an oligodendrocyte progenitor gene expression signature. **(B)** Heatmap of astrocytic specific gene expression profile derived from the single-cell transcriptome atlas analysis showing an overexpression of astrocytic genes in ACVR1 edited clones in comparison to parental/unedited cells. **(C)** Astrocytic identity showed higher enrichment score in ACVR1 edited clones in comparison with parental/unedited cell lines.

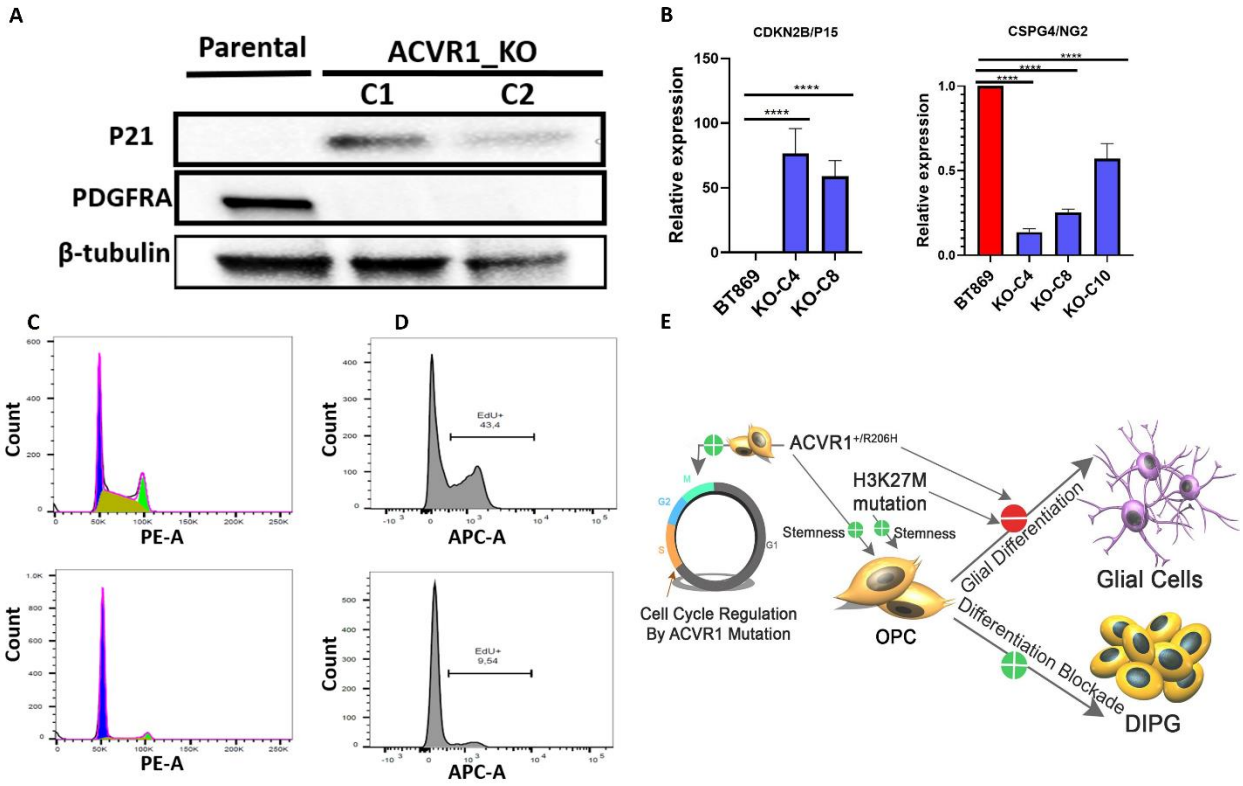

Figure 3. 4. Depletion of R206H mutation in H3.3K27M DIPGs affects stemness and cell cycle regulation.

(A) Western blot analysis for the expression of the oligodendrocyte stemness protein PDGFRA and the cell cycle regulator CDKN1A/P21 in BT869 parental and ACVR1-KO clones. B-tubulin was used as loading control. **(B)** qRT-PCR expression of the cell cycle regulator CDKN2B/P15 and the oligodendrocyte progenitor regulator CSPG4/NG2 in BT869 parental and ACVR1 KO clones. In all panels for qPCR expression analysis a One-way ANOVA was performed for statistical analysis. *p < 0.05, **p < 0.01, ***p < 0.001 ****, and p<0. 0001. Red bars represent parental cell lines and blue bars the ACVR1 KO clones. **(C** and **D)** Flow cytometry analysis of BT869 parental and ACVR1 KO cells using propidium iodide DNA staining for assessing cell cycle **(C)** and DNA synthesis using EdU incorporation **(D)**. **(E)** Schematic model for the potential role of ACVR1$^{+/R206H}$ mutation in the context of H3.3K27M mutation.

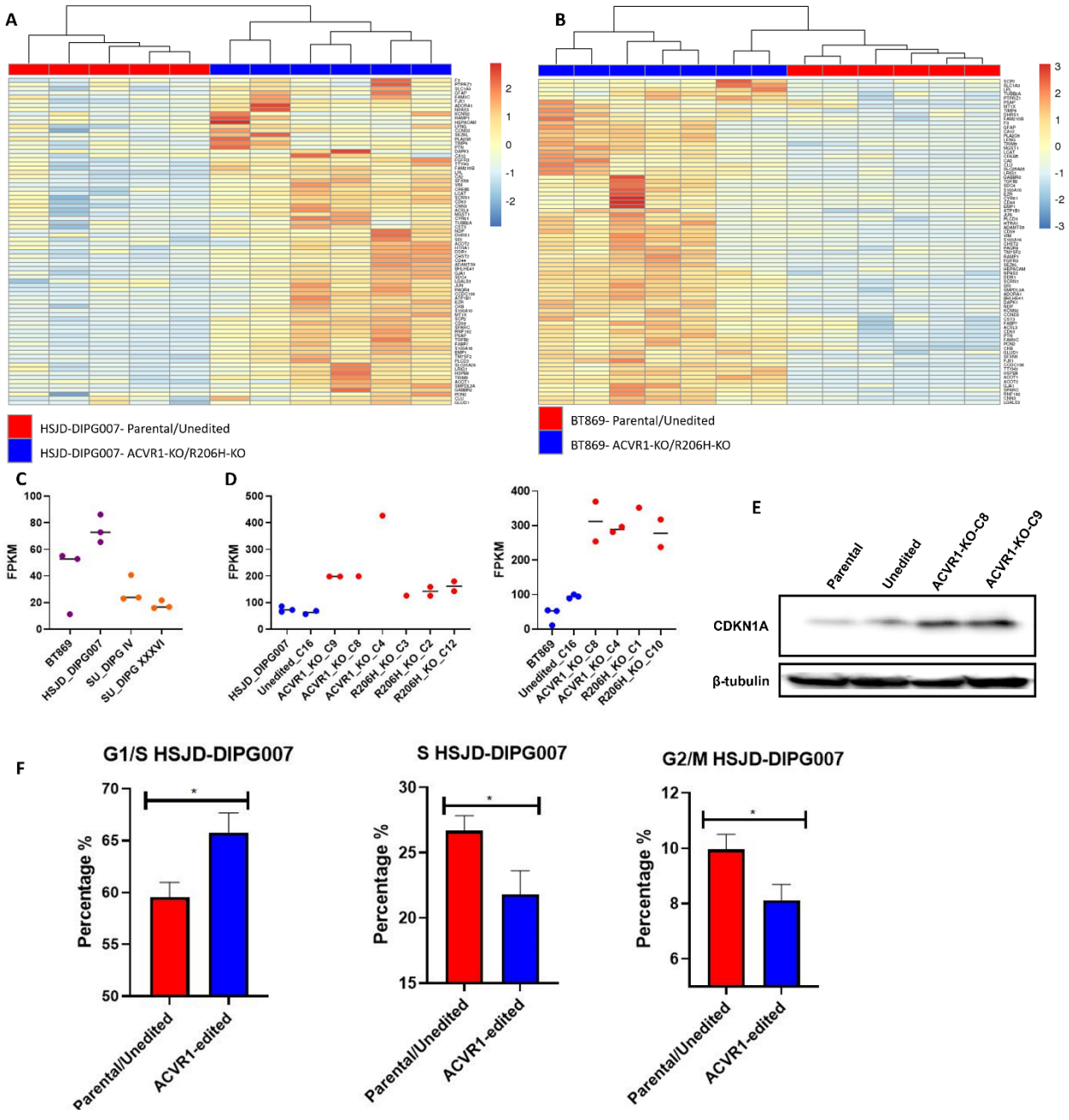
A
B
HSJD-DIPG007- Parental/Unedited
HSJD-DIPG007- ACVR1-KO/R206H-KO
BT869- Parental/Unedited
BT869- ACVR1-KO/R206H-KO
C
FPKM
BT869
HSJD_DIPG007
SU_DIPG IV
SU_DIPG XXXVI
D
FPKM
HSJD_DIPG007
Unedited_C16
ACVR1_KO_C9
ACVR1_KO_C8
ACVR1_KO_C4
R206H_KO_C3
R206H_KO_C2
R206H_KO_C12
FPKM
BT869
Unedited_C16
ACVR1_KO_C8
ACVR1_KO_C4
ACVR1_KO_C1
R206H_KO_C1
R206H_KO_C10
E
Parental
Unedited
ACVR1-KO-C8
ACVR1-KO-C9
CDKN1A
β-tubulin
F
G1/S HSJD-DIPG007
Percentage %
Parental/Unedited
ACVR1-edited
S HSJD-DIPG007
Percentage %
Parental/Unedited
ACVR1-edited
G2/M HSJD-DIPG007
Percentage %
Parental/Unedited
ACVR1-edited

Figure 3.S6. Removal of R206H mutation in HSJD-DIPG007 cell line affects stemness and cell cycle.

(A and B) Common of gene expression profile from the single cell transcriptome atlas analysis between BT869 and HSJD-DIPG007 parental/unedited and ACVR1 KO clones. **(C)** Basal expression level of CDKN1A/P21 across ACVR1 mutant cells. Purple indicates $ACVR1^{+/R206H}$ (H3.3K27M) and orange indicates ($ACVR1^{+/G328E/V}$) cells. **(D)** CDKN1A gene expression showed consistent overexpression in ACVR1 edited in both BT869 and HSDJ-DIPG007 DIPGs. Red represents parental/ unedited cells and blue represents ACVR1 edited clones (R206H-KO and ACVR1-KO). **(E)** Western blot analysis for CDKN1A/P21 protein expression in HSJD-DIPG007 parental/unedited cells and ACVR1 edited clones. B-tubulin was used as loading control. **(F)** Flow cytometry cell cycle analysis of HSJD-DIPG007 parental/unedited cells and ACVR1 KO cells using propidium iodide DNA staining. Student t-test was used for statistical analysis. * represents $p<0.05$ for mean ± SEM for three independent experiments.

ACVR1 G328V/E mutations regulate interaction with the extracellular matrix in H3.1K27M DIPGs

We next asked whether ACVR1 mutation would also affect stemness in H3.1K27M DIPGs similarly to H3.3K27M. To better investigate the role of ACVR1 G328V/E mutations in DIPG tumorigenesis, we knocked out ACVR1 in SU-DIPGIV (H3.1K27M and ACVR1 G328V) and SU-DIPGXXXVI (H3.1K27M and ACVR1 G328E). RNA-seq and qRT-PCR showed that the removal of ACVR1 G328V/E impacted the transcriptome of the edited clones compared to the parental cell lines (Fig 3.5A, 3.5B, 3.S7A, 3.S7B and 3.S7C). However, this effect was much less pronounced than the effect of ACVR1 R206H mutation in H3.3K27M, as shown in the volcano plots (compare Fig 3.S3A and 3.S3B, and 3.S7A, 3.S7B, and 3.S7C). Additionally, no significant change was found in the stemness gene CSPG4/NG2, the astrocytic marker, GFAP, and the regulator of cell cycle CDKN1A/P21, in clear contrast to what was observed in H3.3K27M DIPGs (Fig 3.5A and 3.S7D). These observations indicate that ACVR1 G328V/E and R206H mutations regulate tumorigenesis through different mechanisms. GO analysis shows an enrichment in pathways implicated in extracellular matrix organization and cell-cell adhesion in ACVR1 G328V KO H3.1K27M DIPGs (Fig 3.5C). Among the genes that were differentially expressed in ACVR1 KO versus the parental and unedited cells, the ACVR1 gene itself as well as downstream signaling target genes such as Id1 were significantly downregulated. GDF6, another BMP family member was also downregulated (Fig 3.5D). There was a striking decrease in the expression of genes involved in extracellular matrix organization and cell-cell adhesion (CLDN10, CLDN11) (Fig 3.5D). SU-DIPGIV also presented a significant decrease in expression of the cell cycle gene cyclin D2 involved in the G1/S transition in three different clones in RNA-seq (Fig 3.5D). These findings were confirmed by qRT-PCR (Fig 3.S7E). Interestingly, Cyclin D2 acts in the same pathway as CDKN1A/P21 for the regulation of the cell cycle. However, we did not observe any change in CDKN1A/P21 expression in the KO clones in both SU-DIPGIV and SU-DIPGXXXVI cell lines (Fig 3.S7E and S7F). These results demonstrate that the different ACVR1 mutations, in addition to their specific mechanisms in H3.3 and H3.1K27M respectively, also regulate the cell cycle through different mechanisms. It is worth noting that, in contrast to SU-DIPGIV, we did not identify a direct regulator of cell cycle in SU-DIPGXXXVI (Fig 3.S7F), suggesting that additional mechanisms might be involved in the tumorigenic potential of this cell line. Indeed SU-DIPGXXXVI cells completely lack *Tp53* expression

which might impact the cell cycle and could explain the difference in cell cycle regulation between these two cell lines.

In order to further confirm the role of ACVR1 G328V/E mutation in H3.1K27M DIPGs, we used the developmental single cell RNA-seq atlas for pons and forebrain again to evaluate any significant changes in cell lineages upon removing ACVR1 mutations in the H3.1K27M context. Interestingly, in contrast to ACVR1 mutation in the H3.3K27M context, there is no shift toward astrocytic gene expression profile upon removal of G328V/E mutations in H3.1K27M context (Fig 3.5E and 3.S7G). We indeed observed a decrease in gene expression of astrocytic marker GFAP in SU-DIPGIV (Fig 3.5A and 3.5F). SU-DIPGIV ACVR1-KO did not show a shift towards differentiated glial cells (Fig 3.5E). SU-DIPGXXXVI cells did not show any significant change in gene expression profile related to stemness or astrocytic differentiation, however qRT-PCR showed a decrease in GFAP expression consistent with results observed in SU-DIPGIV cell line (Fig 3.S7H and 3.S7I). The aforementioned results thus demonstrate that the ACVR1 G328V/E mutations in H3.1K27M DIPGs act through the regulation of cell interaction with the extracellular matrix and related biological processes, which might have an impact on cell adhesion and invasion, a mechanism previously described to be regulated by BMP signaling (105,106) and, at least in SU-DIPGIV, G328V mutation regulates the cell cycle through Cyclin D2.

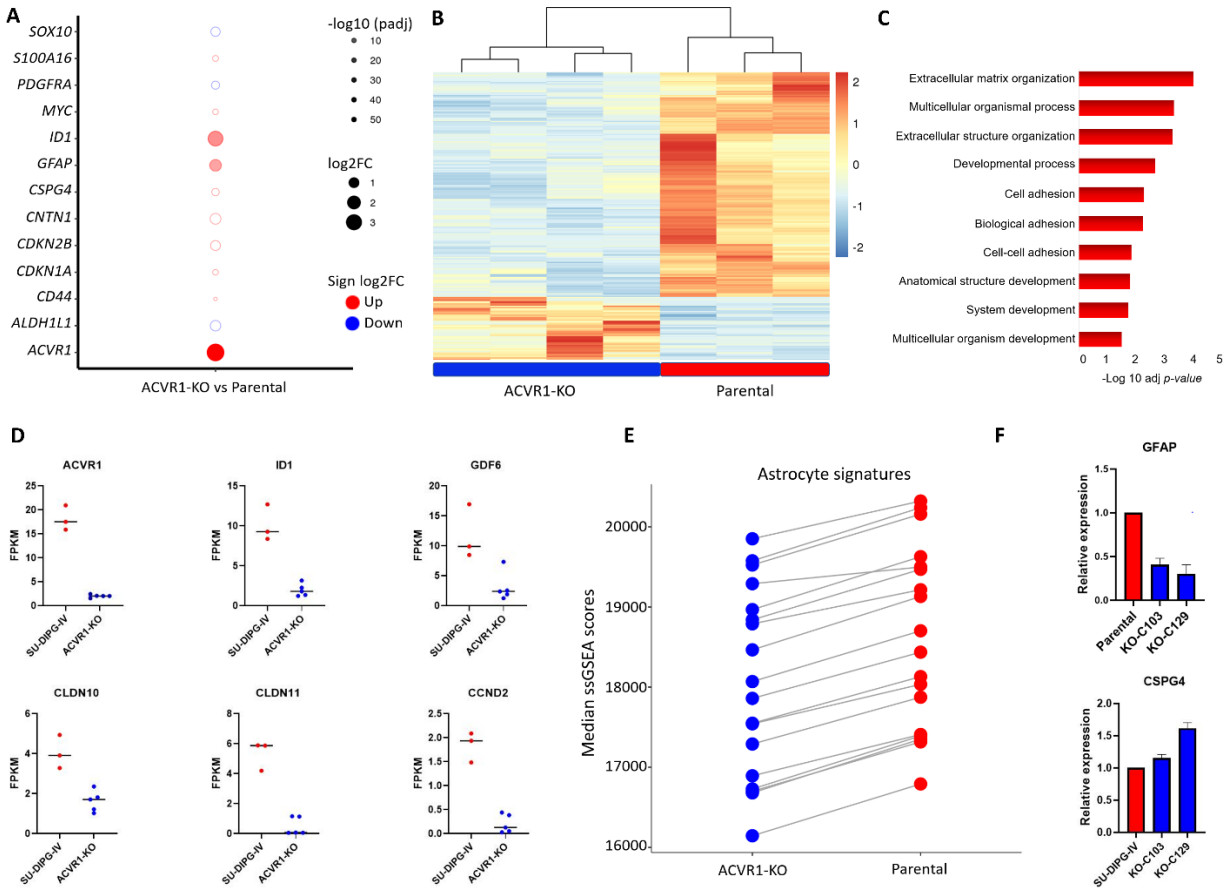

Figure 3. 5. ACVR1 G328V mutation co-occurs with H3.1K27M and regulates interaction with the extracellular matrix.

(A) Dot plot representing transcriptomic changes in SU-DIPG-IV parental and ACVR1 KO clones. In contrast with removal of R206H mutation, low number of genes is significantly affected upon removal of ACVR1 gene in this cell line. **(B)** Heatmap for the hierarchical clustering of differentially expressed genes (FPKM values) showed two distinct transcriptomic clusters for parental and edited ACVR1 KO clones. **(C)** Bulk RNA-seq analysis showing affected genes are involved in BMP signaling, cell adhesion and cell cycle in SU-DIPG-IV. **(D)** Gene ontology analysis using g: Profiler (Padj<0.05) were used to filter significant differential pathways between parental and ACVR1 KO clones. Most affected pathways are involved in extracellular matrix organization and cell-cell adhesion. **(E)** Cell lineage transition analyzed using single-cell transcriptome atlas from pons and forebrain. ACVR1 KO clones did not acquire astrocytic signatures. **(F)** qRT-PCR expression for the astrocytic marker GFAP and oligodendrocyte progenitor regulator CSPG4/NG2 in SU-DIPGIV

isogenic clones and parental cell line. Red and blue are showing parental and CRISPR edited clones respectively in all panels.

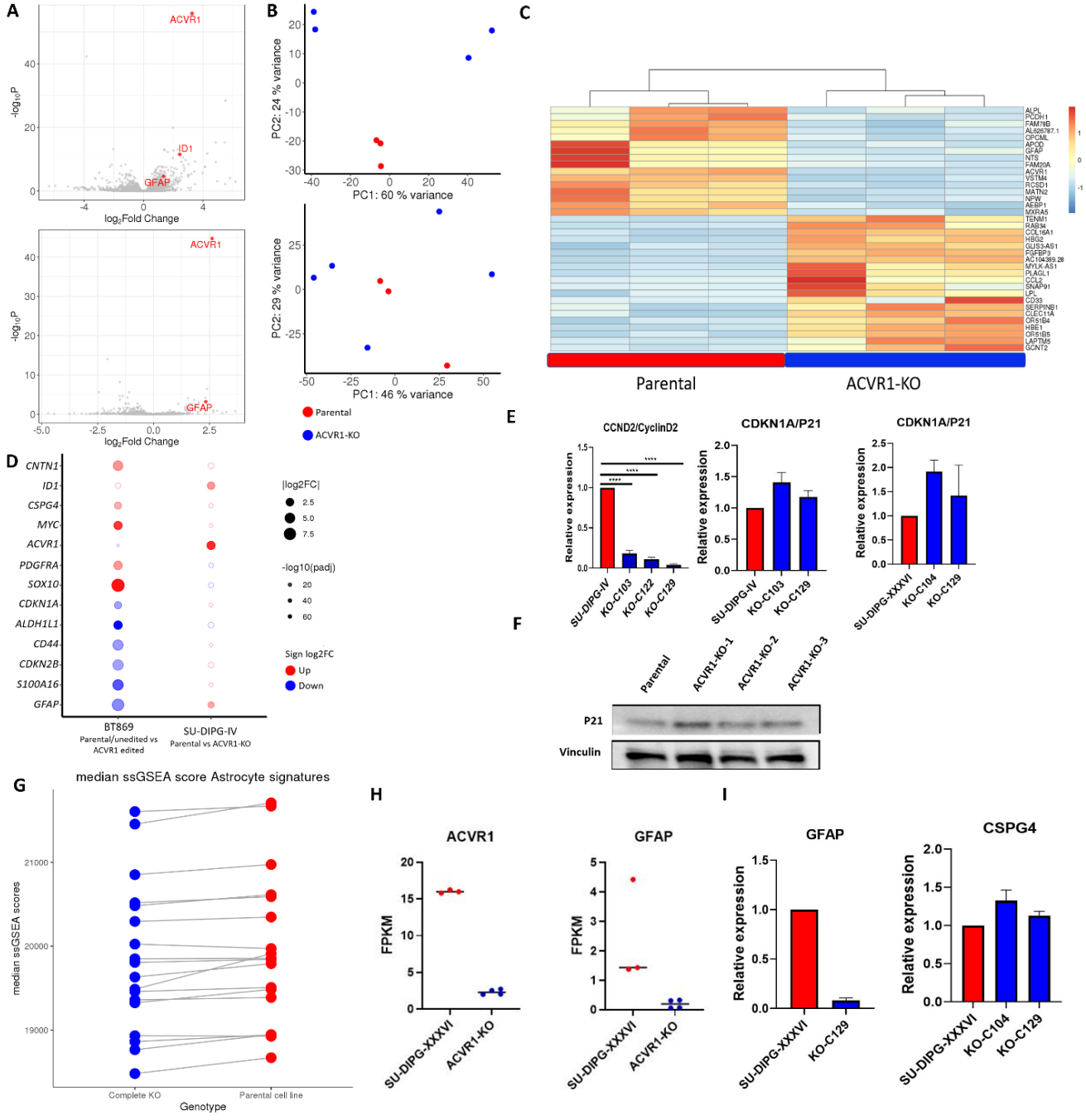

Figure 3.S7. Removal of ACVR1 G328E/V mutation in H3.1K27M DIPGs shows modest changes in transcriptome.

(A) Volcano plot representing transcriptomic changes in SU-DIPG-IV (upper panel) and SU-DIPG-XXXVI (lower panel) parental cells and ACVR1 KO clones. Low number of genes is significantly affected upon removal of ACVR1 gene in this cell line. **(B)** PCA analysis of ACVR1 edited and parental cell lines (SU-DIPGIV upper panel and SU-DIPGXXXVI lower panel), showed modest changes in transcriptome. **(C)** Hierarchical clustering of differentially expressed genes (adj *p-value* <0.05 and log2FC >1) in SU-DIPGXXXVI showed two distinct transcriptomic clusters for parental and ACVR1 KO clones. **(D)** Dot plot comparison of removal of ACVR1 R206H mutation in BT869 and G328V mutation from DIPG-IV did not show overlap on developmental and cell cycle regulator genes. **(E)** qRT-PCR quantification of CDKN1A/P21 in SU-DIPGIV and SU-DIPGXXXVI did not show significant differences between parental and edited clones. **(F)** Western blot analysis of CDKN1A/P21 protein expression in HSJD-DIPG-IV parental/unedited cells and ACVR1 edited clones. Vinculin was used as loading control. **(G)** Cell lineage transition analyzed using single-cell transcriptome atlas from pons and forebrain. SU-DIPG-XXXVI ACVR1 KO clones did not acquire astrocytic signatures. **(H)** Bulk RNA-seq analysis showed significant decrease in expression of astrocytic marker gene (GFAP). **(I)** qRT-PCR quantification of astrocytic marker (GFAP), stemness gene (CSPG4/NG2), and cell cycle gene (CDKN1A/P21) did not show significant changes in stemness and cell cycle. Red represents parental/ unedited cells and blue represents ACVR1 edited clones in all panels.

ACVR1 induces tumorigenesis *in vitro* and *in vivo*

We next sough to study the role of ACVR1 in tumorigenesis in DIPGs. Removal of ACVR1 in H3.3K27M (HSJD-DIPG007 and BT869) and H3.1K27M (SU-DIPGIV, and SU-DIPGXXXVI) DIPGs significantly reduced cell proliferation *in vitro,* as well as their clonogenic potential (Fig 3.6A, and 3.6B). In order to study the role of ACVR1 in tumorigenesis *in vivo*, we orthotopically injected HSJD-DIPG007 and BT869 parental cells and their respective isogenic ACVR1 KO clones in the pontine region of immunocompromised NSG-gamma mice (Fig 3.S8A, 3.S8B, 3.S8C, and 3.S8D). Removal of ACVR1 mutation significantly prolonged the survival of mice for HSJD-DIPG007 cell line (HSJD-DIPG007 parental: 85 days, HSJD-DIPG007 ACVR1 KO: 114 days), and prevented tumor formation in BT869 cells even a year following injection (BT869 parental: 129 days, BT869 ACVR1 KO: >365 days) (Fig 3.6C and 3.S8E). Surprisingly, the absence of tumor formation in mice implanted with BT869 ACVR1 KO clones does not result from the lack of cell survival after implantation as immunohistochemistry staining using human H3K27M antibody shows the presence of H3K27M cells in brain sections from BT869 ACVR1 KO mice albeit at a significantly lower number than the BT869 parental mice (Fig 3.6D). These results clearly imply that removal of ACVR1 from H3.3K27M DIPGs decreases the tumorigenic potential of the cells *in vivo*. H3.1K27M DIPGs were unable to grow when injected in the brain of mice; for this reason, we implanted SU-DIPGIV and SU-DIPGXXXVI cells and their respective isogenic clones subcutaneously in the flank of NSG-gamma mice. SU-DIPGIV and SU-DIPGXXXVI cell lines start developing tumors 2-3 weeks after injection, and mice are euthanized when tumor volume reaches 1.5 cm^3 (Fig 3.S8D and 3.S8E). Mice injected with ACVR1 KO clones showed slower tumor growth and prolonged survival compared to parental and unedited cells in both cell lines (Fig 3.6E, 3.S6D, and 3.S8E). Taken together, these results demonstrate that ACVR1 is an important player in DIPG tumorigenesis *in vitro* and *in vivo*, in both H3.1 and H3.3K27M DIPGs.

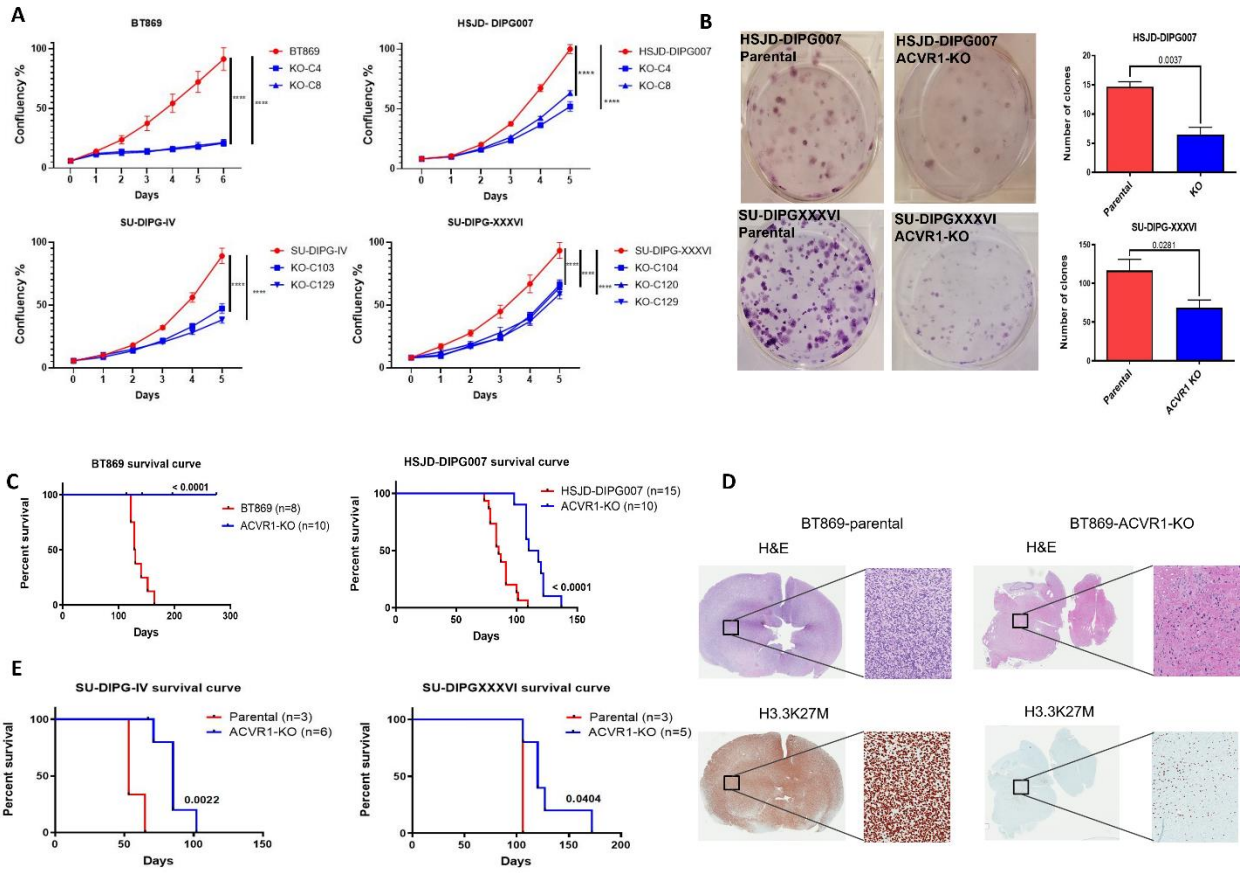

Figure 3. 6. ACVR1 induces tumorigenesis *in vitro* and *in vivo.*

(A) Proliferation assay for primary parental cell lines and isogenic ACVR1 edited clones using Incucyte® S3 Live-Cell Analysis System over 5-6 days. One-way ANOVA was performed for statistical analysis. *** represents $p<0.005$ for the mean ± SEM of three independent experiments. **(B)** Clone formation assay for SU-DIPGXXXVI and HSJD-DIPG007 parental and isogenic ACVR1 KO clones. Student t-test was performed for statistical analysis. * and *** represent $p<0.05$ and 0.005 respectively and represents mean ± SEM of three independent experiments. **(C)** *In vivo* survival curve for mice orthotopically injected in the pons with BT869 and HSJD-DIPG007 parental and ACVR1 KO clones (7.10^5 cells). **(D)** *In vivo* survival curve for mice injected subcutaneously with SU-DIPGIV and SU-DIPGXXXVI parental and isogenic ACVR1 KO clones (4.10^6 cells). Kaplan-Meier analysis was performed for generation of the survival curves. **(E)** H&E and H3K27M staining in BT869 parental cell line and isogenic ACVR1 KO clone. H3K27M

staining showed implantation and survival of ACVR1 KO cells without tumor formation. Red and blue colors are showing parental and ACVR1 edited cells respectively in all panels.

A

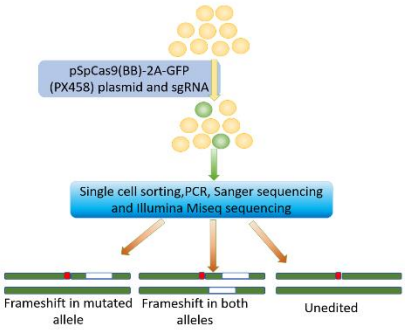

B

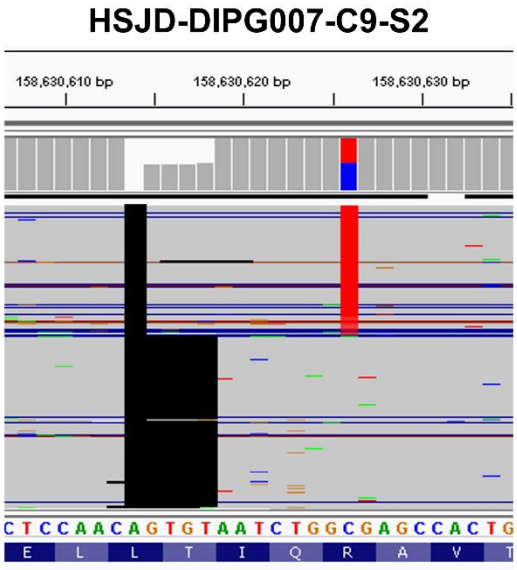

C

Cell line	Histone mutation	ACVR1 mutation	Edited clones
HSJD-DIPG007	H3.3K27M	R206H	ACVR1-KO, R206H-KO
BT869	H3.3K27M	R206H	ACVR1-KO, R206H-KO
SU-DIPG-IV	H3.1K27M	G328V	ACVR1-KO
SU-DIPGXX-VI	H3.1K27M	G328E	ACVR1-KO

D

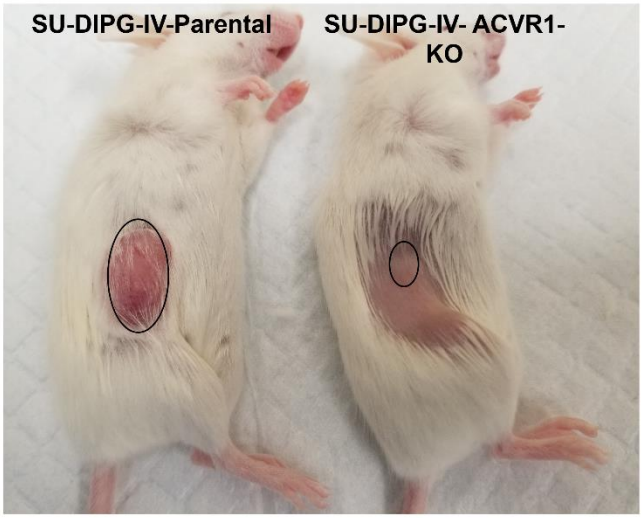

E

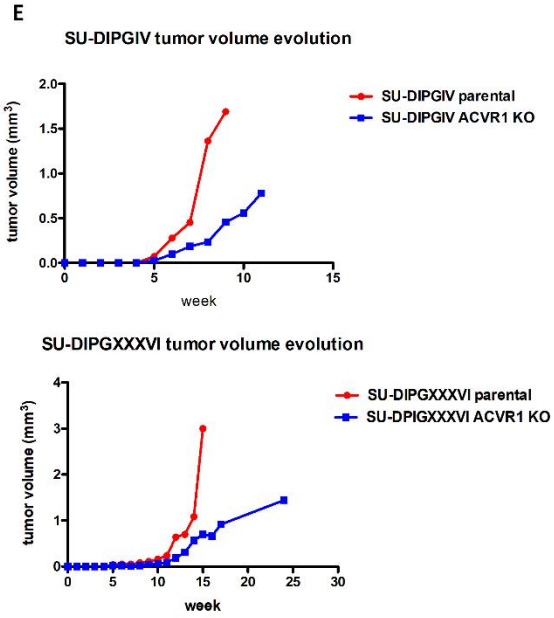

Figure 3.S8. Generation of isogenic CRISPR edited cells for ACVR1 R206H and G328E/V mutations using primary DIPG cell lines.

(A) schematic representation of the CRISPR editing strategy used in this study. CRISPR guide was used to target exon 6 of ACVR1 gene. Positive clones were sorted as single cell using FACS for isogenic clones. ACVR1 sequences were checked on all isogenic clones using sanger and Illumina Miseq sequencings. **(B)** Representative example of Illumnia Miseq results for HSJD-DIPG007. Edited clone showed one (on mutated allele) and four (on wild type allele) base pair frame shift deletion to generate complete ACVR1 KO clone. **(C)** List of primary cell lines and ACVR1 KO clones used in this study. The histone and ACVR1 mutations are indicated. **(D)** Representative image of subcutaneous tumors from mice injected with SU-DIPGIV parental and ACVR1 KO clones showing different tumor burden in parental and edited clines. (**E)** Tumor volume evolution in SU-DIPGIV and SU-DIPGXXXVI parental and ACVR1 KO clones showing clear difference in tumor growth between parental and ACVR1 KO clones in both cell lines. Tumor volume was measured twice per week using a caliper.

M4K2009 is a novel specific ACVR1 inhibitor and a potential therapeutic candidate in DIPGs

Our findings described above attribute an important role for ACVR1 in tumorigenesis of DIPGs and imply that ACVR1 might induce tumorigenesis early during development in collaboration with H3K27M. Thus, ACVR1 represents a potential therapeutic target in DIPGs. Multiple classes of ALK2 inhibitors are widely used in animal models of FOP. However, none of these compounds yielded beneficial effects due to the fact that they do not act as specific inhibitors for ALK2 but rather have a pan inhibitory effect on different ALK receptors (107). The off-target effects of ALK inhibitors is also extended to DIPGs, whereby a response to the drug is observed regardless of ACVR1 mutation status (Fig 3.S9A). Hence, the design of more specific ACVR1 inhibitors is needed in order to improve ACVR1 targeting and clinical relevance. M4K2009, a newly designed compound, was recently designed as a specific ALK2 inhibitor with very low potency on other ALK receptors (108,109). To validate the specificity of M4K2009, we performed a dose curve survival assay on DIPG parental cell lines as well as their isogenic ACVR1 KO clones. Interestingly, DIPG parental cell lines were more vulnerable to M4K2009 than the ACVR1 KO clones, which responded to the drug with higher IC50 doses (Fig 3.7A, 3.S9B). Deletion of one ACVR1 allele (R206H KO) in HSJD-DIPG007 was not sufficient to abolish the response to M4K2009, further denoting the specificity of M4K2009 for the ALK2 receptor (Fig 3.7A). We compared the effect of M4K2009 to another ALK2 inhibitor, TP-0184, a compound that entered a clinical trial for DIPG but did not show efficacy. In contrast to M4K2009, ACVR1 KO clones were still responsive to TP-0184 denoted by the same range IC50 values compared to parental cells (Fig 3.7A, 3.S9B). M4K2009 significantly decreased BT869, HSJD-DIPG007, SU-DIPGIV, and SU-DIPGXXXVI cell proliferation rates *in vitro* (Fig 3.7B, 3.S9C) and reduced clone formation in SU-DIPGXXXVI (Fig 3.7C).

These results demonstrate that M4K2009 exerts specificity to ALK2 and that it represents a potential candidate to the treatment of DIPGs that warrants further testing.

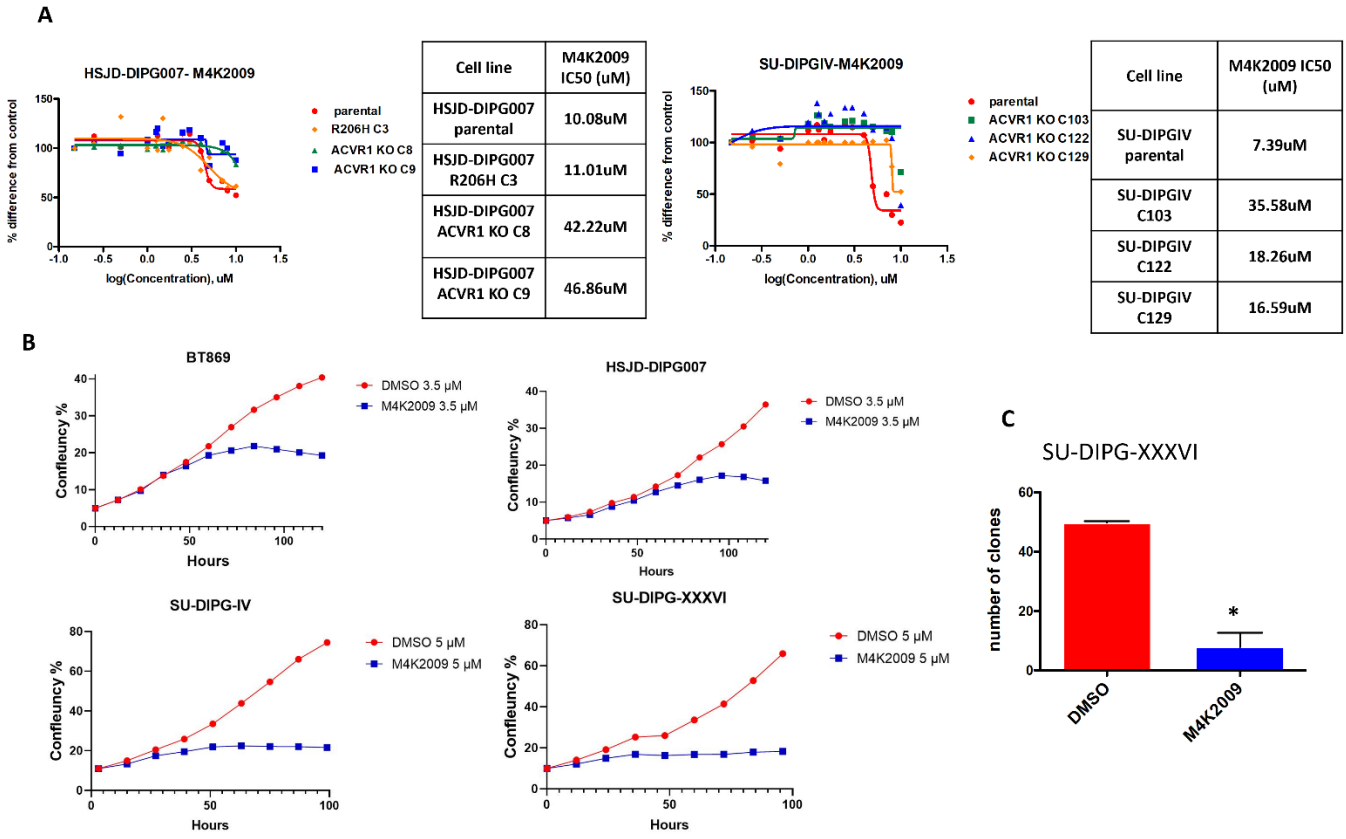

Cell line	M4K2009 IC50 (uM)
HSJD-DIPG007 parental	10.08uM
HSJD-DIPG007 R206H C3	11.01uM
HSJD-DIPG007 ACVR1 KO C8	42.22uM
HSJD-DIPG007 ACVR1 KO C9	46.86uM

Cell line	M4K2009 IC50 (uM)
SU-DIPGIV parental	7.39uM
SU-DIPGIV C103	35.58uM
SU-DIPGIV C122	18.26uM
SU-DIPGIV C129	16.59uM

Figure 3. 7. M4K2009 is a novel therapeutic agent for ACVR1 and is specific for ALK2.

(A) Drug survival curves for M4K2009 on HSJD-DIPG007 and SU-DIPGIV parental and ACVR1 KO clones. Tables show IC50 doses denoting less sensitivity of ACVR1 KO clones to M4K2009. **(B)** M4K2009 decreases proliferation over 5 days in BT869, HSJD-DIPG007, SU-DIPGIV, and SU-DIPGXXXVI. **(C)** M4K2009 decreases clone formation in SU-DIPGXXXVI cells. *indicates $p<0.05$ and represents average ± SEM of three independent experiments. Student t-test was applied for the analysis.

A

	ACVR1 mutant				ACVR1 WT			
	H3.1 K27M			H3.3K27M	H3.3 K27M			
	SU-DIPGIV	SU-DIPGXXXVI	SU-DIPGXXI	HSJD-DIPG007	SU-DIPGXIII	SU-DIPGVI	DIPG011	DIPG14
E6201	82.4uM	11.48uM	3.57uM	5.38uM	219.3uM	48.03uM	3.73uM	7.28uM
LDN212854	3.6uM	2.41uM	5.65uM	5.2uM	3.67uM	2.28uM	2.09uM	2.74uM
K00991	3.86uM	7.43uM	5.72uM	20.33uM	5.74uM	3.24uM	2.51uM	3.75uM
K04284	97.9uM	14.17uM	21.46uM	24.4uM	56.01uM	40.9uM	17.19uM	170.35uM
K05908	79.4uM	9.59uM	16.88uM	18.01uM	85.06uM	46.42uM	221.8uM	16uM

B

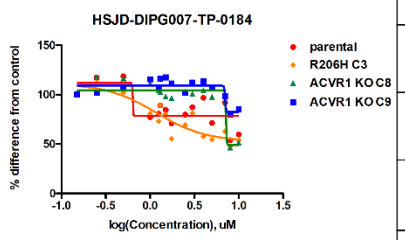

Cell line	TP-0184 IC50 (uM)
HSJD-DIPG007 parental	11.81uM
HSJD-DIPG007 R206H C3	7.92uM
HSJD-DIPG007 ACVR1 KO C8	11.51uM
HSJD-DIPG007 ACVR1 KO C9	27.41uM

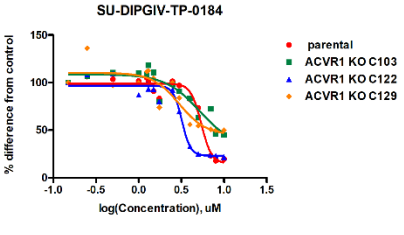

Cell line	TP-0184 IC50 (uM)
SU-DIPGIV parental	6.18uM
SU-DIPGIV C103	8.75uM
SU-DIPGIV C122	5.14uM
SU-DIPGIV C129	7.72uM

Figure 3.S9. Widely available ACVR1 inhibitors are not specific for ALK2.

(A) Screening of different ACVR1 inhibitors in a panel of DIPG cell lines harboring or not ACVR1 mutations. IC50 values are shown indicating no difference in the effect of these drugs in mutated and non-mutated cells. **(B)** Drug survival curves for TP-0184 on HSJD-DIPG007 and SU-DIPGIV parental and ACVR1 KO clones. Tables show IC50 doses denoting that TP-0184 is not specific for ACVR1 and it exerts the same effect on parental and ACVR1 KO clones.

Chapter 3.2

H3.1K27M and H3.3K27M mutations have differential effects on the epigenome

Generation of a suitable *in vitro* model to study H3K27M mutations

To better understand the role of H3K27M in DIPG tumorigenesis, we used primary DIPG cell lines harboring H3.1K27M or H3.3 K27M mutations (Table 4.1). We generated different cell models to investigate differences between these two contexts (Fig 4.1). CRISPR-Cas9 systems were used to remove ACVR1 and K27M mutations by knocking out a mutant allele or both alleles of the gene in different cell lines. The different cell lines that were edited are SU-DIPG-IV (H3.1K27M), SU-DIPG-XXXVI (H3.1K27M), SU-DIPG-XXI (H3.1K27M), and BT869 (H3.3K27M) (Table 4.2). In addition to this study, other cell lines have been studied and their results have been published, including DIPG-XIII (H3.3K27M), BT245 (H3.3K27M), and HSJ019 (H3.3K27M) (39–41) (Table 4.3).

To study and compare H3K27M mutations in different contexts, in addition to generating isogenic CRISPR-edited cell lines, we have manipulated and edited wild type cell by running overexpression experiments. In addition, we also examined SU-DIPG-XXXVI H3.1K27M-KO to overexpress H3.3K27M and BT245 H3.3K27M-KO to overexpress H3.1K27M.

Finally, to study time dependency of the PRC2 complex activity and its effect on spreading and catalyzing H3K27me2/me3 marks, we have used our isogenic ACVR1 edited cell lines, which we have proved have slower proliferation rates in comparison with their parental/unedited cell lines.

To gain insight into epigenomic differences between H3.1K27M and H3.3K27M, we have generated H3K27me1/me2/me3, H3K27ac, H3K36me2/me3, and transcriptomic data for all aforementioned experiments. In addition, we have used counterpart epigenomic and transcriptomic data for H3.3K27M cell lines from Harutyunyan et al., (2019 and 2020) (39,40).

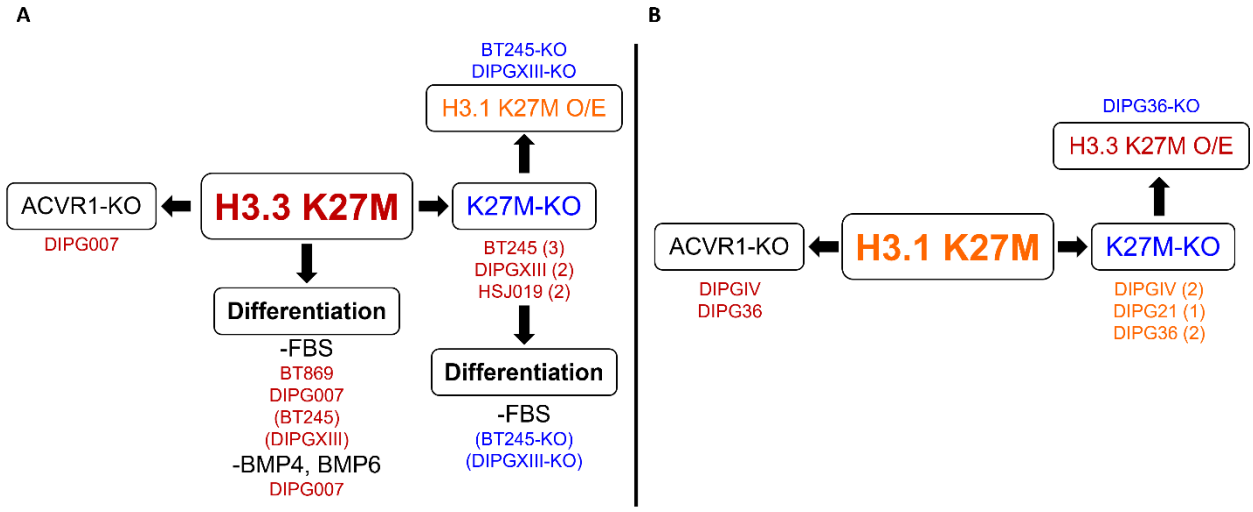

Figure 4. 1. Schematic overview on core experimental datasets to study H3.1K27M and H3.3K27M mutations.

(A) core experiments on H3.3K27M cell lines and **(B)** main experiments on H3.1K27M cell lines.

Table 4. 1. transcriptomic and epigenomic datasets generated for H3K27M gliomas and histone WT gliomas.

Red indicates H3.3K27M cell lines, orange indicates H3.1K27M cell lines and blue is showing histone wildtype cell lines.

Cell line	Age/ Gender	Location	Mutation	MS	K27ac	K36me2	K27me2	K27me3	CRISPR out K27M
BT245	8M	Thalamus	H3.3 K27M	Done	Done	Done	Done	Done	Done
SU-DIPGVI	7F	Pons	H3.3 K27M	Done	Done	-	-	Done	-
SU-DIPGXIII	6F	Pons	H3.3 K27M	Done	Done	Done	Done	Done	Done
HSJD-DIPG-007	9.9M	Pons	H3.3 K27M	Done	Done	Done	Done	Done	-
HSJ019	13F	Thalamus	H3.3 K27M	Done	Done	Done	Done	Done	Done
HSJ031	9F	Pons	H3.3 K27M	Done	Done	Done	Done	Done	-
HSJ051	11M	Thalamus	H3.3 K27M	-	Done	Done	Done	Done	-
BT-869	7F	Pons	H3.3 K27M	Done	Done	Done	Done	Done	Done
SU-DIPGIV	2F	Pons	H3.1 K27M	Done	Done	Done	Done	Done	Done
SU-DIPGXXI	7M	Probably Pons	H3.1 K27M	Done	Done	Done	Done	Done	Done
SU-DIPG36	3F	midbrain	H3.1 K27M	Done	Done	Done	Done	Done	Done
G477	7F	Cortex	WT	Done	Done	Done	Done	Done	N/A
SU-pcGBM2	15M	Cortex	WT	Done	Done	Done	Done	Done	N/A

.

Table 4. 2. experimental datasets including transcriptomic and epigenomic data generated for CRISPR edited H3.1K27M cell lines.

Orange and blue are indicating parental/unedited and H3.1K27M-KO clones respectively.

Cell line	Mutation	Edit	Clone	MS	K27ac	K36me2	K27me2	K27me3	RNA-seq	WGBS
DIPGIV	H3.1 K27M	parental	mix (2)	3x	Done	Done	Done	Done	3x	1x
DIPGIV	H3.1 K27M	unedited	C3	-	Done	Done	Done	Done	3x	-
DIPGIV	H3.1 K27M	K27M-KO	C1 (C8)	-	Done	Done	Done	Done	3x-C1, 1x-C8	1x (C8)
DIPGIV	H3.1 K27M	K27M-KO	C9	-	Done	Done	Done	Done	2x	-
DIPGXXI	H3.1 K27M	parental	p28	3x	Done	Done	Done	Done		1x
DIPGXXI	H3.1 K27M	unedited	C4	-	Done	Done	Done	Done		-
DIPGXXI	H3.1 K27M	K27M-KO	C7	-	Done	Done	Done	Done		1x
DIPG36	H3.1 K27M	parental	p20	4x	Done	Done	Done	Done	3x	1x
DIPG36	H3.1 K27M	unedited	C1	-	Done	Done	Done	Done	2x	-
DIPG36	H3.1 K27M	K27M-KO	C2	-	Done	Done	Done	Done	3x	1x
DIPG36	H3.1 K27M	K27M-KO	C3	-	Done	Done	Done	Done	3x	-

Table 4. 3. experimental datasets including transcriptomic and epigenomic data generated for CRISPR edited H3.3K27M cell lines.

Red and blue are indicating parental/unedited and H3.1K27M-KO clones respectively.

Cell line	Mutation	Edit	Clone	MS	K27ac	K36me2	K27me2	K27me3	RNA-seq	WGBS
BT245	H3.3 K27M	parental	C24	3x	Done*	Done	Done	Done	5x	1x
BT245	H3.3 K27M	unedited	C1	-	Done	Done	Done	Done	1x	-
BT245	H3.3 K27M	K27M-KO	C2	2x	Done	Done	Done	Done	2x	1x
BT245	H3.3 K27M	K27M-KO	C4	2x	Done	Done	Done	Done	2x	-
BT245	H3.3 K27M	K27M-KO	C5,C7	2x	Done	-	-	-	2x	-
DIPGXIII	H3.3 K27M	parental	C14	3x	Done	Done	Done	Done	-	1x
DIPGXIII	H3.3 K27M	unedited	C12	-	Done	-	Done	-	2x	-
DIPGXIII	H3.3 K27M	K27M-KO	C5	2x	Done	Done	Done	Done	1x	1x
DIPGXIII	H3.3 K27M	K27M-KO	C10	2x	Done	Done	Done	Done	1x	-
HSJ019	H3.3 K27M	parental	C7	3x	Done	Done	Done	Done	-	-
HSJ019	H3.3 K27M	parental	p25	-	Done	Done	Done	Done	4x	1x
HSJ019	H3.3 K27M	K27M-KO	C8	2x	Done	Done	Done	Done	2x	-
HSJ019	H3.3 K27M	K27M-KO	C10	2x	Done	Done	Done	Done	2x	1x

H3K27me3 is less abundant in H3.1K27M in comparison with H3.3K27M mutated primary cell lines.

H3K27me3 is a repressive mark, which has been shown to be affected significantly by H3K27M mutations. Recently, Sarthy et al., (2020) showed a global reduction of H3K27me3 in H3.3K27M context, but the complete absence of this mark in H3.1K27M contexts (110). To substantiate or contradict their previous findings as to whether level or spread of this mark is different between the two contexts or H3K27me3 is absent in H3.1K27M, we have done series experiments on patient derived cell lines. Mass spectrometry data for patient derived cell lines and results showed the presence of the H3K27me3 in both H3.3K27M and H3.1K27M cell lines, although the amount of these modifications are lower in H3.1K27M primary cell lines in comparison with H3.3K27M cell lines (Fig 4.2A). In addition, we profiled this histone modification in H3.1K27M and H3.3K27M cell lines using ChIP-seq and we found consistency with our mass spectrometry analysis, in which the number of regions (peaks) identified for H3K27me3 is lower in H3.1K27M context (Fig 4.2B). The correlation analysis has revealed that even though the H3K27me3 mark in H3.1K27M context is more limited to CGIs, but more CGIs and bin have shown H3K27me3 to appear in H3.3K27M mutant lines. In conclusion, H3.1K27M and H3.3K27M led to global decrease of the H3K27me3 mark. It's important to note that the level of this modification is lower in H3.1K27M, but still present in comparison with H3.3K27M.

Previously, it has been described that the mechanism of the H3.3K27M mutation works so that upon its removal, there is significant spread of H3K27me3 mark into surrounding regions .To study whether H3.1K27M and H3.3K27M show the same or different mechanistic behavior upon their removal, we have generated isogenic cell lines in which both mutations have been removed across different cell lines using the CRISPR-Cas9 strategy. All generated cell lines have been profiled using ChIP-seq experiments for H3K27me3 modifications. In both contexts, removing mutations showed the same mechanistic behavior in spread and the global increase of H3K27me3 modifications in H3KK27M-KO cell lines, in comparison with their parental and unedited cell lines (Fig 4.2C). So, despite different levels of this mark in these two contexts,

removing these mutations show the same mechanistic behavior in restoring H3K27me3 levels (Fig 4.2C).

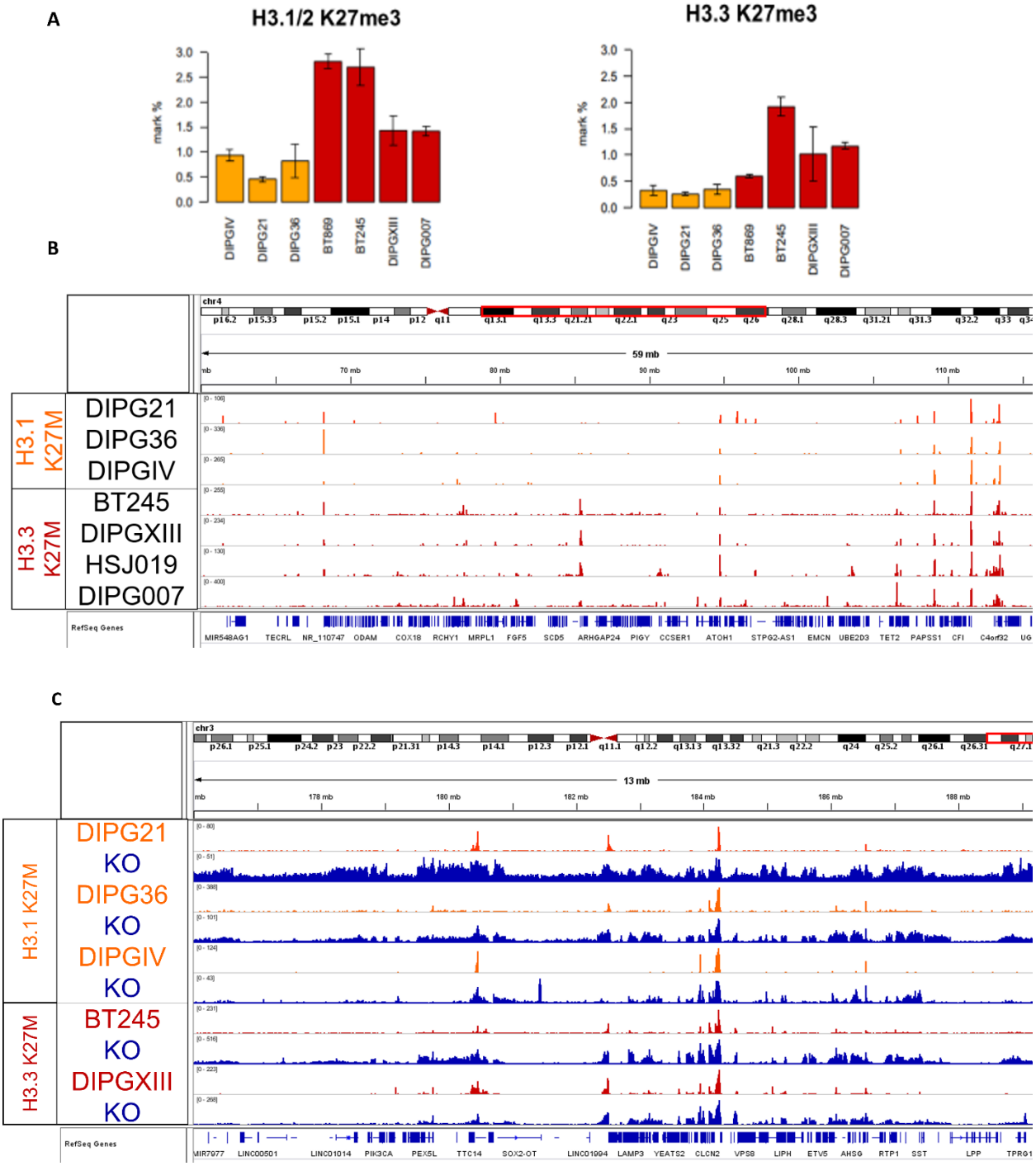

Figure 4. 2. H3K27M restrict H3K27me3, an effect reversible by alleviating inhibition of PRC2

(A) Mass spectrometry data of H3.1/2K27me3 and H3.3K27me3 in diffuse midline gliomas, mean % +/- SD. **(B)** H3K27me3 ChIP-seq enrichment tracks over a large representative genomic region in gliomas. H3K27me3 shows generally similar narrow distribution in both H3.1K27M and H3.3K27M mutated cell lines. **(C)** H3K27me3 ChIP-seq enrichment tracks, in representative K27M-mutant and isogenic CRISPR-KO cell lines, over the same region. Orange and purple colors are showing H3.1K27M and H3.3K27M cell lines respectively. Blue color indicates isogenic K27M-KO edited clones.

H3K27me2 is less abundant in H3.1K27M in comparison with H3.3K27M mutated primary cell lines.

Currently, our group has shown lower levels of H3K27me2 in patient derived cell lines caused by the H3.3K27M mutation and upon removal of this mutation using CRISPR-Cas9 system led to restores H3K27me2 spread and increase the global level of this mark . To study possible differences in the level of H3K27me2 in our primary cell lines between H3.1K27M and H3.3K27M, we have generated mass spectrometry data. This data showed lower levels of H3K27me2 in both H3.1K27M and H3.3K27M in comparison with wildtype cell lines. We were also able to exhibit consistent and lower levels of H3K27me2 in H3.1K27M mutated primary cell lines in comparison with H3.3K27M (Fig 4.3A). In addition, we profiled this histone modification using ChIP-seq for H3.1K27M and H3.3K27M cell lines. ChIP-seq analysis supported there being less H3K27me2 and little spread of this mark in H3.1K27M in comparison with H3.3K27M mutated primary cell lines (Fig 4.3B and 4.3C).

To test whether the removal of H3.1K27M mutation support the same mechanistic behavior with H3.3K27M in restoring H3K27me2 spread and levels, we used the CRISPR-Cas9 system to remove this mutation and generate isogenic system (32). Previously, our group found H3K27me2 levels in H3.3K27M mutated cell lines corresponded to H3K27me3 cell lines that upon removal of the H3.3K27M mutation, displayed a significant increase in H3K27me2 levels comparable with wildtype cell lines (32). To tease out the effect of the H3.1K27M mutation, in addition to parental

cell lines, we profiled H3K27me2 in three H3.1K27M-KO and three H3.3K27M-KO cell lines (Fig 4.4A). Our results indicated that H3K27me2 levels in H3K27M are similar to H3K27me3 in H3K27M-KO clones (Fig 4.4A). This behavior was the same between the two contexts with significant increase and spread of H3K27me2 exhibited in both contexts. One of the possible explanations for different levels of H3K27me2 modification between these two contexts is the difference in the mutational burden of H3.1K27M and H3.3K27M. Our mass spectrometry results across different patient derived cell lines showed that there is no significant difference in the level of H3.1K27M and H3.3K27M mutations (Fig 4.4B). So, despite contrasting levels of H3K27me2 between H3.1K27M and H3.3K27M, possibly due to the different cells of origin but after removal of mutations, they have exhibited the same behavior in spreading to surrounding regions and restoring H3K27me2 levels.

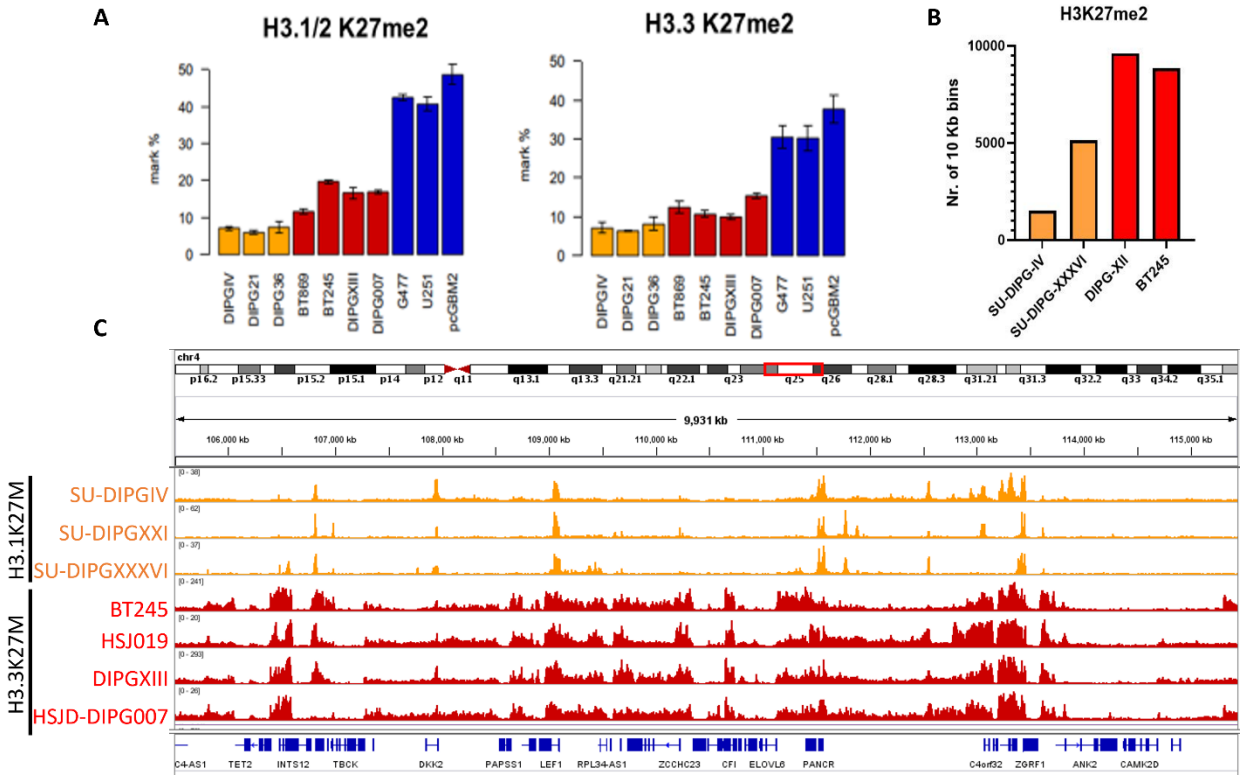

Figure 4. 3. H3K27M restrict H3K27me2 and H3K27me2 is less spread in H3.1K27M context.

(A) Mass spectrometry data of H3.1/2K27me3 and H3.3K27me3 in diffuse midline gliomas, mean % +/- SD. **(B)** H3.3K27M showed higher number of 10 kb bins enriched for H3K27me2 in comparison with H3.1K27M mutated cell lines. **(C)** H3K27me3 ChIP-seq enrichment tracks over a large representative genomic region in gliomas. H3K27me2 is least spread in H3.1K27M and occupies broader domains in H3.3K27M.

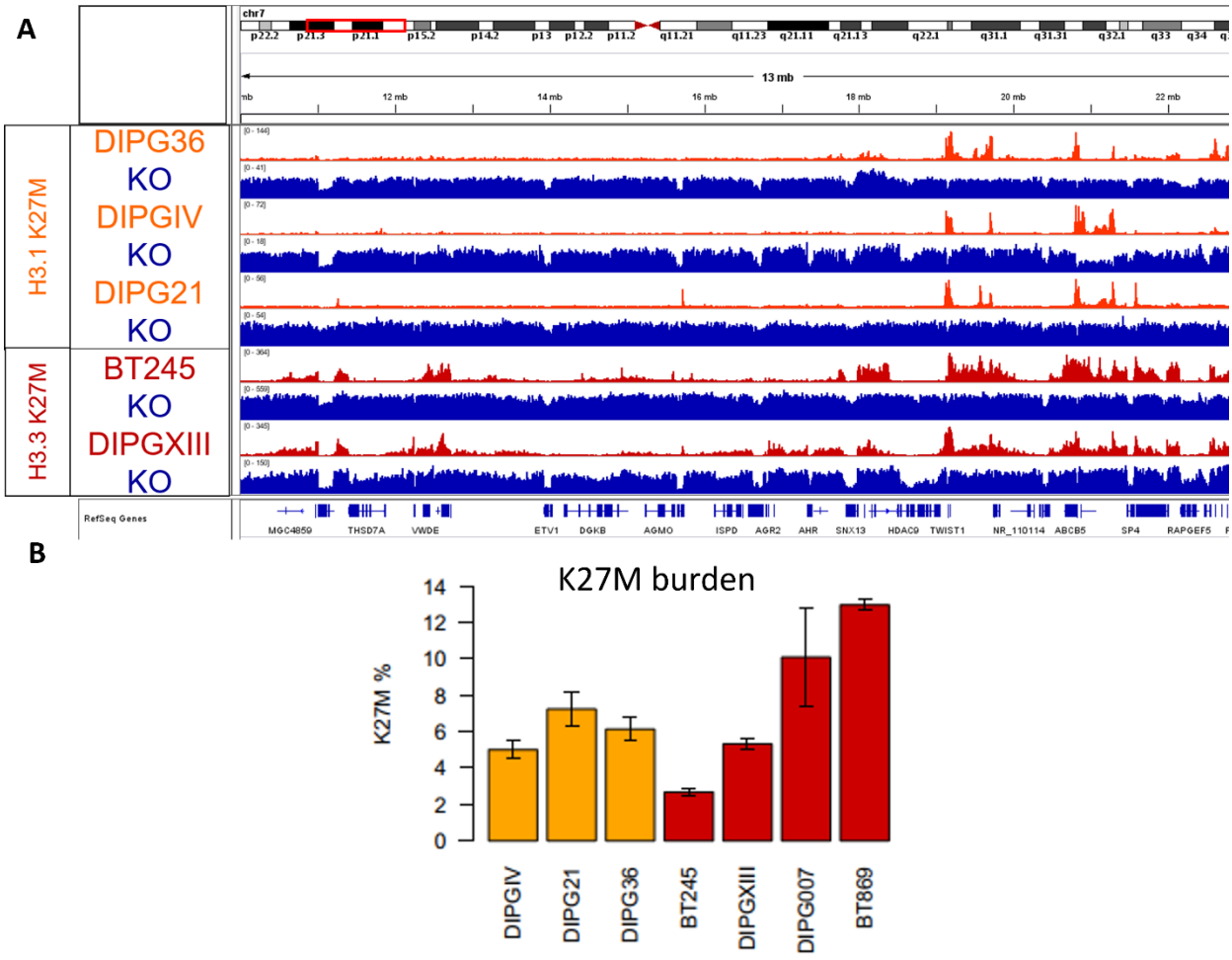

Figure 4. 4. H3K27M effect of H3K27me2 is reversible by alleviating inhibition of PRC2.

(A) H3K27me3 ChIP-seq enrichment tracks, in representative K27M-mutant and isogenic CRISPR-KO cell lines, over the same region. Orange and purple colors are showing H3.1K27M and H3.3K27M cell lines respectively. Blue color indicates isogenic K27M-KO edited clones. **(B)** Mass spectrometry data has been used to measure mutational burden of H3.1K27M and H3.3K27M.

H3K27ac is negatively correlated with H3K27me2/me3 and shows pervasive patterns in comparison with wildtype cell lines.

It has been shown, in the presence of H3.3K27M mutations, that there is a global decrease in the level of H3K27me2/me3 and a global increase in the level of H3K27ac modifications (24,26,27,80). Our research identified the presence of the H3.3K27M mutation as having led to pervasive acetylation across the genome (80). To study how H3.1K27M mutations affect H3K27ac in the genome and to study the relationship between H3K27me2/me3 and H3K27ac in H3.1K27M and H3.3K27M contexts, we have generated tumor-derived isogenic models bearing these mutations (Table 2 and Table 3). Mass spectrometry and ChIP-seq profiling for H3K27ac across parental cell lines and isogenic models for H3.1K27M and H3.3K27M mutations showed a pervasive state of acetylation in both contexts in comparison with wildtype models (Fig 4.5A and 4.5B). As H3K27ac is a narrow mark, MACS for peak calling supported a modestly higher number of peaks in the H3.1K27M context in comparison with H3.3K27Mc, which may reflect lower levels of H3K27me2/me3 in comparison with H3.3K27M cell lines. In summary, both contexts support a global decrease in H3K27me2/me3 levels and pervasive acetylation across the genome.

Previous to our research, the mutual exclusivity of H3K27me3 and H3K27ac had been established. In our research, we asked whether the same exclusivity is present for H3K27ac and H3K27me2 in our patient derived cell lines. To determine the relationship between H3K27ac and H3K27me2, we have divided the SU-DIPGIV genome into 10 kb bins. For all bins, we have generated scatter plots based on the RPKM values for H3K27ac and H3K27me2 PTMs. Scatter plot results indicated marks exhibiting mutually exclusive behavior, except a few regions with both H3K27ac and H3K27me2 marks (Fig 4.5C). To elaborate more on these observations, we have limited our 10 kb bins in SU-DIPGIV to those with RPKMs bigger than one for H3K27ac and/or H3K27me2. Venn diagram analysis also supported findings of mutually exclusive behavior with the exception of 44 bins (44 bins out of 12411 regions for H3K27me2) (Fig 4.5E). To find out why there are a small number of 10 kb bins with both H3K27ac and H3K27me2 levels, we visualized H3K27ac and H3K27me2 tracks across different cell lines (Fig 4.5D). Tracks showed complete, mutually exclusive behavior of these marks in these regions as 10 kb bins can be divided between two marks without overlap (Fig 4.5E). To see our results for SU-DIPGIV repeated

across several H3.1K27M and H3.3K27M cell lines on a global level, we have generated heatmaps for both H3K27me2 and H3K27ac. Results clearly showed there is a consistent pattern of exclusivity for H3K27ac and H3K27me in all examined cell lines regardless of H3.1K27M and H3.3K27M mutations (Fig 4.5F).

In conclusion, we have found pervasive acetylation in both H3.1K27M and H3.3K27M contexts in comparison with wildtype contexts. In addition, we have found H3K27ac is mutually exclusive from H3K27me2, similar to results described for H3K27me3.

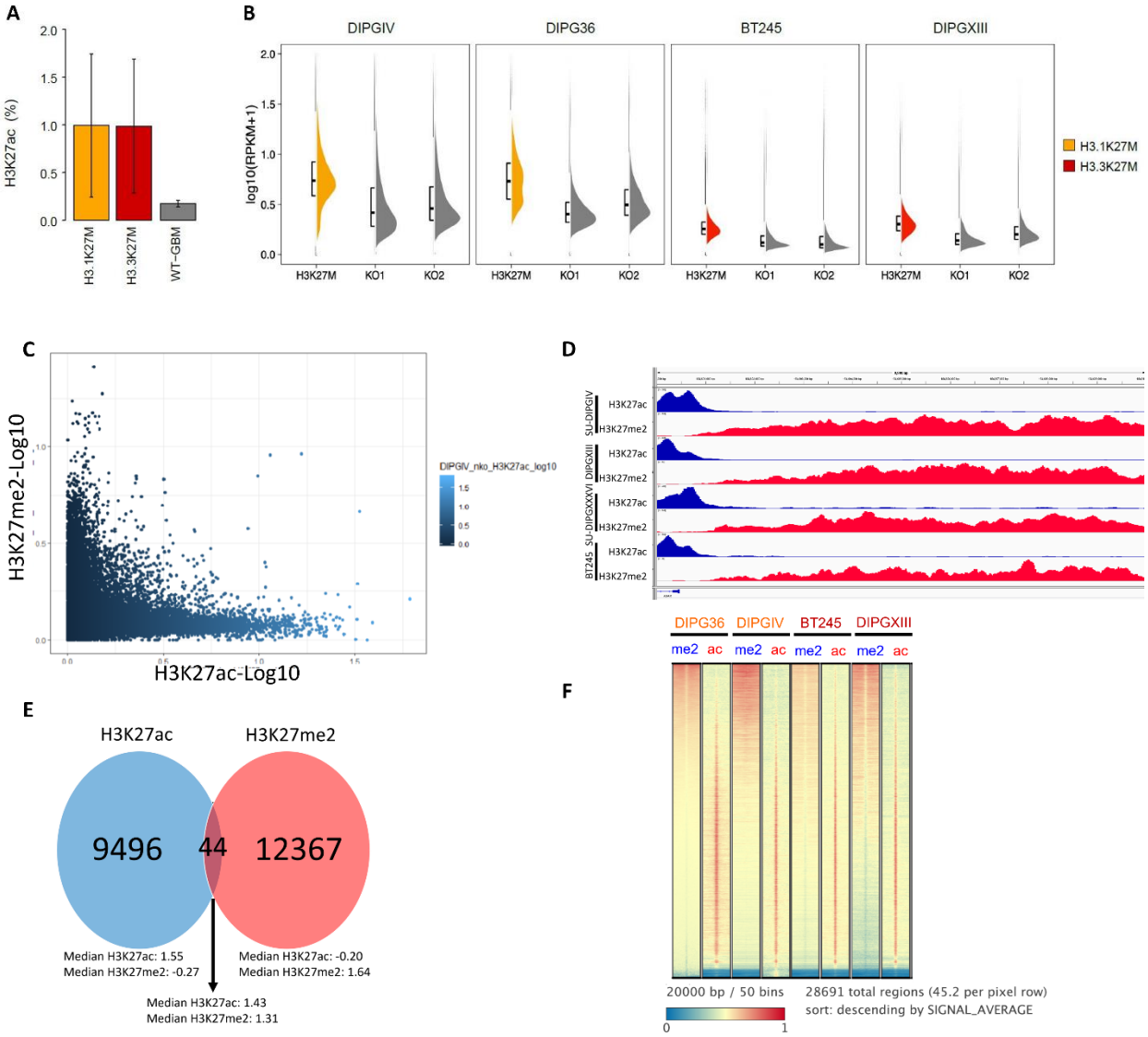
A
H3K27ac (%)
H3.1K27M
H3.3K27M
WT-GBM
B
DIPGIV
DIPG36
BT245
DIPGXIII
log10(RPKM+1)
H3K27M
KO1
KO2
H3.1K27M
H3.3K27M
C
H3K27me2-Log10
H3K27ac-Log10
DIPGIV_nko_H3K27ac_log10
D
SU-DIPGIV
DIPGXIII
SU-DIPGXXVI
BT245
H3K27ac
H3K27me2
E
H3K27ac
H3K27me2
9496
44
12367
Median H3K27ac: 1.55
Median H3K27me2: -0.27
Median H3K27ac: -0.20
Median H3K27me2: 1.64
Median H3K27ac: 1.43
Median H3K27me2: 1.31
F
DIPG36
DIPGIV
BT245
DIPGXIII
me2
ac
20000 bp / 50 bins
28691 total regions (45.2 per pixel row)
sort: descending by SIGNAL_AVERAGE
0
1

Figure 4. 5. pervasive acetylation is common to H3.1 and H3.3K27M gliomas and H3K27ac is negatively correlated with H3K27me2/me3 in both H3.1K27M and H3.3K27M contexts.

(A) Mass spectrometry data of H3K27ac in gliomas and ependymomas, mean % +/- SD. H3K27M mutant gliomas. Distribution of genome-wide H3K27ac signal in isogenic glioma cell lines, showing pervasive spread of H3K27ac in both H3.1 and H3.3K27M. **(B)** Distribution of genome-wide H3K27ac signal in isogenic glioma cell lines, showing pervasive spread of H3K27acin both H3.1 and H3.3K27M. show higher levels of this histone mark **(C)** scatter plot for H3K27me2 and H3K27ac behavior across the genome of SU-DIPGIV. whole genome has been divided into 10 kb bins and levels of H3K27me2 in H3K27ac calculated. **(D)** Venn diagram to overlap 10 kb bins with RPKM >1 for H3K27me2 and H3K27ac in SU-DIPGIV cell line. **(E)** tracks are showing mutually exclusive behavior in 10 kb bins which have high level of H3K27ac and H3K27me2 across different cell lines. **(F)** Heatmap plots of ChIP-seq signal intensity for H3K27me2 and H3K27ac across different H3.1K27M and H3.3K27M cell lines.

Slowing down proliferation rates increases level and spread of H3K27me2/me3 marks in H3K27M contexts.

We have found that the mechanism of action for H3.1K27M and H3.3K27M is the same in restricting H3K27me2/me3 to diffuse midline gliomas. Characteristics of different cells of origin, such as doubling times, are one of the possible reasons for differing levels of H3K27me2/me3 in H3.1K27M and H3.3K27M contexts. To assess whether PRC2 function is time dependent or not, we have designed a number of experiments to decrease proliferation rates in H3.1K27M and H3.3K27M primary cell lines. To investigate the potential variances in these patient derived cell lines, we quantified their doubling times based on the proliferation experiments. These experiments have been performed using the IncuCyteS3 machine and then doubling times were calculated. Our results across six different cell lines supported the finding that H3.1K27M showed faster proliferation rates and shorter doubling times in comparison with H3.3K27M cell lines (Fig 4.6A). As expected and consistent with our previous results, H3.1K27M corroborated earlier findings of lower levels of H3K27me2/me3 along with shorter cycling time (Fig 4.6B). As these experiments have been done in diffuse midline gliomas characterized by H3K27M mutation, the need for functional experiments in isogenic systems are critical to assess the role of cycling times in the level of H3K27me2 mark. To this aim, we have removed the ACVR1 mutation for the SU-DIPGIV cell line. Removal of ACVR1 mutation led to a decrease in proliferation rates, while maintaining H3K27M mutation (Fig 4.7A). Also, it has not been shown that ACVR1 is involved in any epigenetic regulation. Therefore, to substantiate our findings on the effect of the removal of the ACVR1 mutation, we have profiled the transcriptome of parental and edited cell lines using bulk RNA-seq. Bulk RNA-seq analysis did not show any changes related to genes involved in epigenetic regulation. So, this model provides a reliable isogenic model to study the effect of time on H3K27me2 levels (Fig 4.7A). In this regard, we sought to identify whether they show changes in the level of H3K27me3 and its spread. Our results clearly documented an increase in the number of bins with H3K27me3 and spread of this mark into surrounding regions (Fig 4.7B) in ACVR-KO cells lines. ChIP-seq track distribution for all three cell lines showed spread and the appearance of new peaks in all three ACVR1-KO cell lines (Figure 4.S9). In addition, ChIP-seq analysis revealed considerable increase and spread of H3K27me2 mark in H3.1K27M upon removal of ACVR1 mutation in SU-DIPG-IV cell line. ACVR1-KO cell lines showed higher number

of bins (10 kb bins) with H3K27me2 in comparison with parental cell lines, but lower bin numbers than H3.1K27M-KO cells (Fig 4.7C). Furthermore, to provide genome wide analysis, as H3K27me2 is a broad mark, we have divided genome into 100 kb bins to generate scatter plot. Scatter plot revealed high number of 100 kb bins enriched for H3K27me2 in ACVR1 edited clones in comparison with control group (Fig 4.7D). Visualization of tracks using IGV indicate same trend in spread of H3K27me2 in ACVR1 edited clones (Figure 4.7E). Since there is no known role for ACVR1 to regulate PTMs and our transcriptomic data did not show significant changes in the gene expression of related proteins (ie. writers, readers and erasers), we believe these effects are due to the slower proliferation rate of these cells.

In our recent publication, Harutyunyan et al., (2020) showed that H3K36me2 forms boundaries with H3K27me2/me3 (88). Our ChIP-seq analysis revealed that upon the removal of ACVR1 mutations and deceleration of the cell cycle, PRC2 has more time to spread up to the point where the H3K36me2 mark is met. To investigate this possibility, we checked ChIP-seq track distribution for H3K27me2 and H3K36me2 marks in our isogenic contexts. Interestingly, we found many big domains in which H3K27me2 is spread in the regions lacking H3K36me2 marks in ACVR1-KO (Fig 4.7E). They do not, however, reach to the same level as present in H3.1K27M-KO cells (Fig 4.7C.

In summary, we have exhibited that the slowing down of the cell cycle is providing more time for PRC2 complex activity in both H3.1K27M and H3.3K27M cell lines. This led to an increase in the level and spread of H3K27me2/me3 marks in comparison with parental cell lines. Despite having the same trend, it seems the spread is more pronounced in H3.3K27M cell lines.

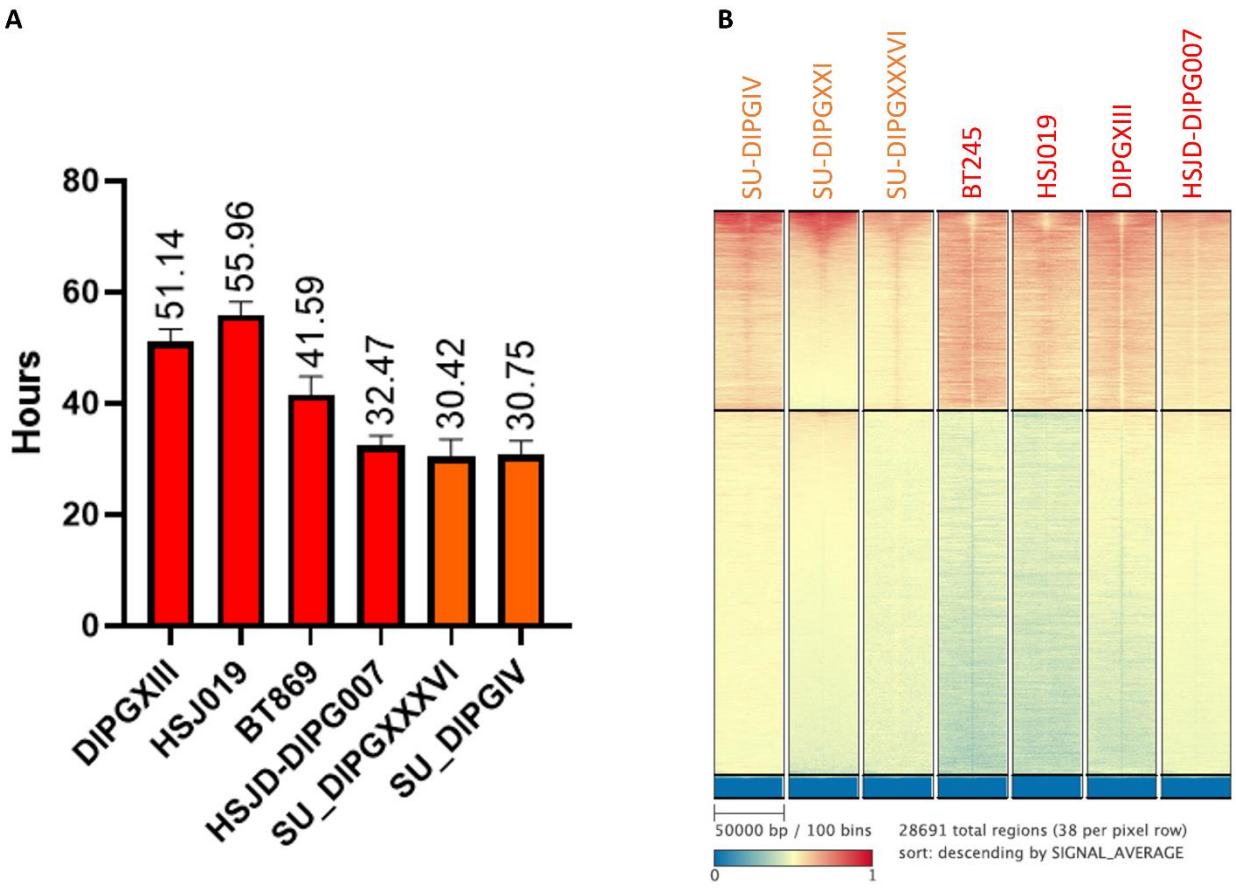

Figure 4. 6. H3.1K27M cell lines proliferate faster than H3.3K27M cell lines with lower level of H3K27me2.

(A) Doubling times of patient derived cell lines were calculated based on their proliferation rates obtained from IncuCyte S3. Red indicates H33K27M and orange indicates H3.1K27M. **(B)** Heatmap plots of ChIP-seq signal intensity for H3K27me2 across different H3.1K27M and H3.3K27M cell lines.

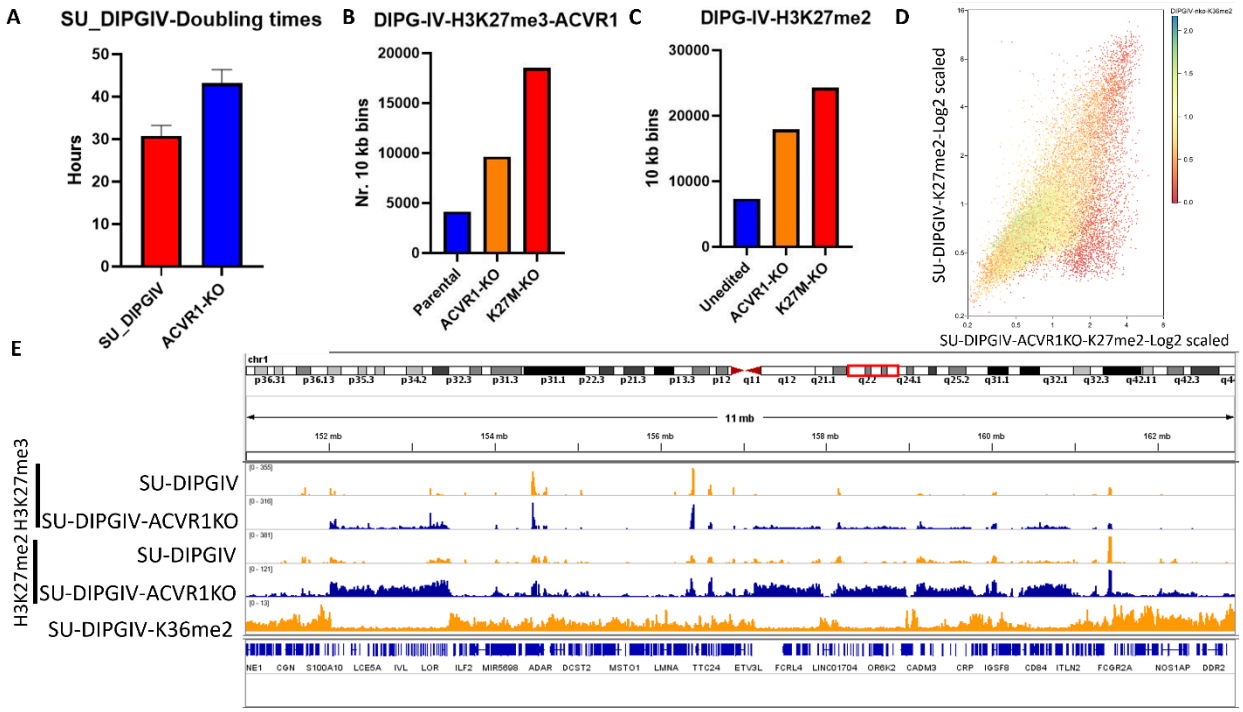

Figure 4. 7. Slowing down proliferation rates increases level and spread of H3K27me2/me3 marks in H3K27M contexts.

(A) Removal of ACVR1 mutation using CRISPR-Cas9 system from SU-DIPGIV slowing down cell cycle. **(B)** ACVR1 KO showed higher number of 10 kb bins enriched for H3K27me2 in comparison with parental cell lines and less than H3.1K27M KO isogenic clones. **(C)** ACVR1 KO showed higher number of 10 kb bins enriched for H3K27me2 in comparison with parental cell lines and less than H3.1K27M KO isogenic clones. **(D)** Genome wide comparison of H3K27me2 in SU-DIPGIV parental cell line and ACVR1 edited clone. Genomes divided into 100 kb bins to generate scatter plot. **(E)** tracks for H3K27me2, H3K27me3 and H3K36me2 for SU-DIPGIV edited clone and parental cell line is showing increasing H3K27me2 and H3K27me3. H3K27me2 is spreading in SU-DIPGIV spread until H3K36me2 boundaries.

Epigenomic and transcriptomic data revealed H3.1K27M and H3.3K27M have different profiles of lineage specific genes.

In this section of our research, we used transcriptomic and epigenomic data from different patient derived cell lines and their isogenic clones to study the behavior of lineage specific genes in H3.1K27M and H3.3K27M contexts. Previously, Krug et al., (2019) and Harutyunyan et al., (2019) showed significant transcriptomic shifts upon the removal of H3.3K27M mutations (32,80). Also, data from a study by Jessa et al., (2019) supported H3.3K27M mutation block differentiation that, upon removal of H3.3K27M from DIPG-XIII and the provision of cells with differentiation factors, differentiated cells into GFAP positive cells (69). To investigate the role of H3.1K27M in DIPGs, this mutation was removed from SU-DIPG-IV and SU-DIPG-XXXVI, and Bulk RNA-seq data was generated from these cells. Upon removal of H3.1K27M, Transcriptomic analysis of our isogenic cell lines revealed drastic changes in gene expression in both cell lines (Fig 4.8A and 4.8B). Consistent with our expectation that H3.1K27M mutations lead to a global decrease in repressive H3K27me3 mark level, most of the genes were downregulated upon removal of the H3.1K27M mutation (Fig 4.8C and 4.8D). Our results presented additional findings. The first, is that there were differentiating DIPG cell lines with H3.3K27M mutation when using 10% fetal bovine serum (FBS) for two weeks. Our results further revealed that the differentiation with BMP4 and CNTF increased the number of GFAP positive cells, which reflects astrocytic differentiation. In contrast, parental cell lines with the H3.1K27M mutation never expressed an increase in GFAP expression based on immunofluorescence staining and q-RT-PCR. In addition, removal of the ACVR1 mutation from DIPG cell lines with H3.3K27M showed clear lineage differentiation towards astrocyte fate. Single sample GSEA analysis using a mouse brain developmental atlas revealed the profile of astrocyte specific genes were upregulated upon removal of ACVR1 mutations in H3.3K27M cell lines. In contrast, removal of ACVR1 mutations in H3.1K27M cell lines did not support any significant shift toward astrocytic lineage. Even GFAP expression showed modest downregulation. To investigate the role of H3.1K27M in blocking astrocytic specific genes, we removed H3.1K27M mutation from SU-DIPGIV and SU-DIPGXXXVI cell lines. In addition to immunofluorescence staining for GFAP, we preformed qRT-PCR for this gene in the absence and presence of 10 % FBS (Fig 4.9A, 4.9B, and 4.9C). Our results did not show any significant increase in expression level of GFAP. In addition, we profiled the transcriptome of

SU-DIPGIV using bulk RNA-seq data. Interestingly, this cell line did not reveal any significant increases in GFAP expression, even though they showed a significant downregulation of GPAP expression, similar to our observation for ACVR1-KO in the same cell lines (Fig 4.9D). In addition, after removal of the H3.1K27M mutation from SU-DIPGIV, we differentiated isogenic KO clones in comparison with parental cell lines using 10% FBS for two weeks and BMP4 (20 ng/ml) and CNTF (20 ng/ml) for one week (Fig 4.9A, 4.9E, and 4.9F). Immunofluorescence staining did not show any differences and increase in expression of GFAP (Fig 4.9A). Furthermore, q-RT-PCR showed a modest downregulation of GFAP in parental cell line for both differentiation protocols (Fig 4.9B, 4.9E, and 4.9F). Finally, we have replicated all of the results for SU-DIPGIV by SU-DIPGXXXVI as another patient-derived H3.1K27M cell line (Fig 4.10A, 4.10B, and 4.10C). All of these observations highlight the possibility of different cell of origins for DIPGs within H3.1K27M and H3.3K27M cell lines. To decode possible differences related to cells of origin based on our differentiation and isogenic experiments, we have used integrated transcriptomic and epigenomic analysis. We profiled H3K27me3 in promoter regions for both H3.1K27M and H3.3K27M cell lines. Then, we generated specific gene lists for each of the H3.1K27M and H3.3K27M mutations. Selection favored those genes with two-fold levels of H3K27me3 in H3.1K27M in comparison with H3.3K27M cell lines. Integration with transcriptomic data showed clear anticorrelation between H3K27me3 methylation levels and gene expression levels for H3.1K27M specific genes (Fig 4.11A and 4.11B). As H3K27me3 level is lower in H3.1K27M in comparison with H3.3K27M, there H3.1K27M has a shorter list of genes. This list contains many important developmental genes related to nervous system stem cells and development. OLIG1, OLIG2, PAX3, SOX8 and many other neural stem cells and glial stem cells found on this gene list have higher H3K27me3 and lower gene expression levels in H3.1K27M (Fig 4.11B). In contrast, these genes are showing lower levels of H3K27me3 and higher expression levels in H3.3K27M cell lines (Fig 4.11B). In addition to H3K27me3, we have investigated H3K27ac in these master regulators of stemness and have found that there are higher levels of H3K27ac in H3.3K27M cell lines in comparison with H3.1K27M (Fig 4.11B). These transcription factors play important roles in neural stem cells and glial progenitors; for example, Monje et al., (2011) identified neural precursor cells with Olig2 expression as cells of origin for DIPGs (38). In addition, we have found

DIPGs with H3.3K27M mutations exhibit high levels of OLIG2 expression that could be differentiated to the glial lineage. DIPGs with H3.1K27M mutations and low levels of OLIG2 are not able to be differentiated in this lineage.

To study the profile of lineage specific genes for H3.3K27M mutations, we have identified promoters enriched for H3K27me3 (RPKM>1 and FC>2) in H3.3K27M in comparison with H3.1K27M (Fig 4.12A). Due to higher levels of H3K27me3 in H3.3K27M in comparison with H3.1K27M, we have found a longer list of genes in this context. To simplify our analysis, we have restricted our list to transcription factors based on Lambert et al., (2018), which provides a list of human transcription factors (111). Interestingly, we have found promoter regions of many members of homeobox genes (HOX), including HOXA2, HOXB2, HOXD3, HOXD4, and HOXD8 with higher level of H3K27me3 in H3.3K27M in comparison with H3.1K27M cell lines (Fig 4.12A). Mapping gene expression data generated by bulk RNA-seq data from the same cell lines showed lower expressions of these genes in H3.3K27M context (Fig 4.12B). These genes showed lower levels of H3K27me3 in H3.1K27M and their expression was higher in comparison within the H3.3K27M context (Fig 4.12B and 4.12C). It is interesting to note that previously, Castel et al., (2018) used ChIP-seq and RNA-seq data from diffuse midline gliomas to show higher expression levels of OLIG2 in H3.3K27M (with lower H3K27me3) and lower expression of HOXD8 (with higher level of H3K27me3) (Fig 4.12C) (100).

Furthermore, we have found anatomical locations also playing a role in shaping epigenomics and transcriptomic features of diffuse midline gliomas. For example, heatmaps for genes enriched for H3.1K27me3 in H3.1K27M show more similarities with pontine H3.3K27M cell lines than H3.3K27M cell lines derived for thalamic tumors. For example, HOXD3 and HOXD4 showed higher expression levels in pontine H3.3K27M cell lines, including DIPGXIII and BT869 cell lines, in comparison with thalamic cell lines like BT245 and HSJ019. These genes exhibit the highest expression in H3.1K27M cell lines (pontine), then in H3.3K27M (pontine) and finally lowest expression in thalamic tumor cell lines with H3.3K27M mutations (Fig 4.12C and 4.12D).

So, our integrated transcriptomic and epigenomic analyses revealed H3.1K27M and H3.3K27M cell lines exhibited significantly different profiles of lineage specific transcription factors, which

strongly reflect their different cell or lineage of origin. These differences in cells of origin could explain the differences in the epigenomic landscape of tumors, partially explained through different proliferation rates.

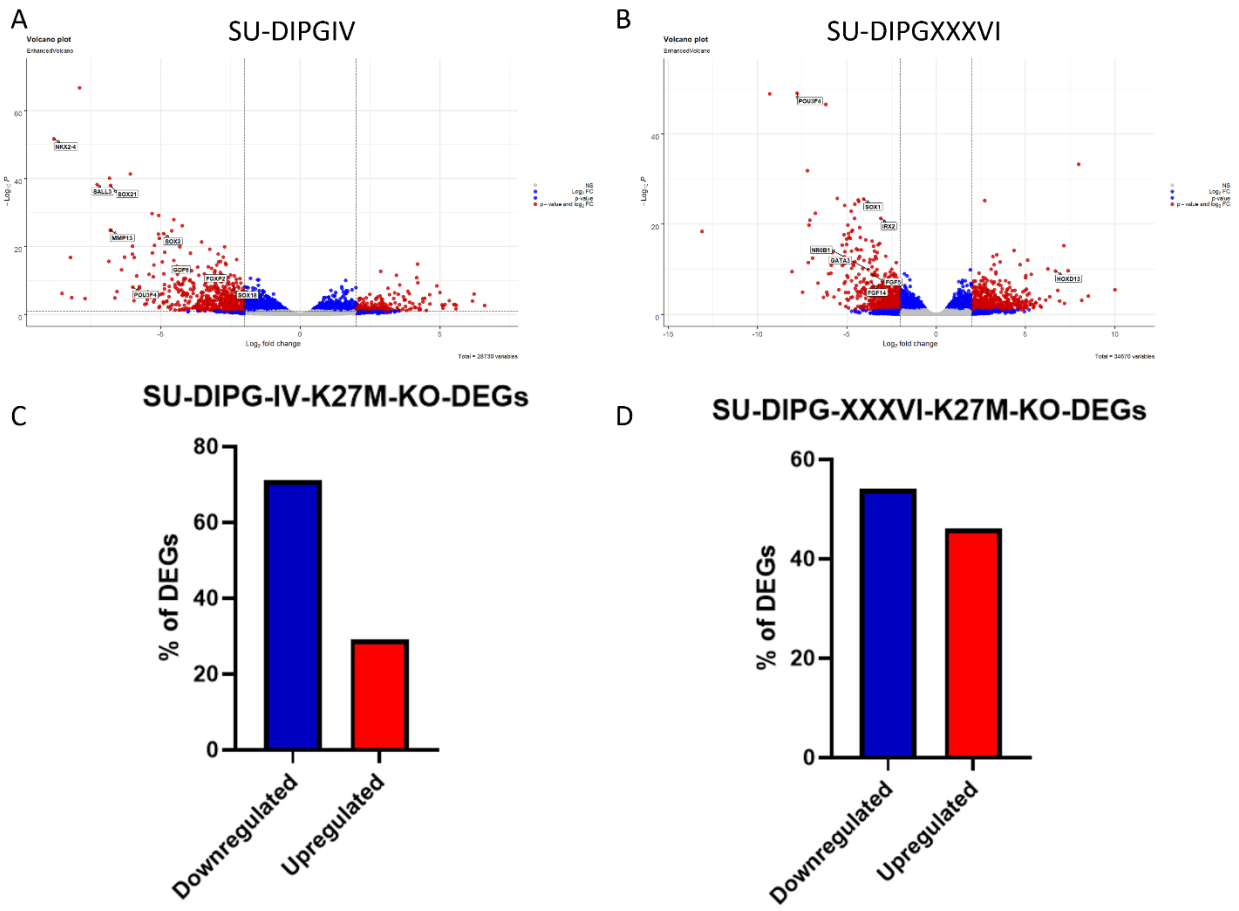

Figure 4. 8. Removal H3.1K27M and restoring H3K27me2/me3 affects gene expression profiles of patient-derived cell lines.

(A) volcano plot is showing high number of genes are differentially expressed after removal of H3.1K27M in SU-DIPGIV. **(B)** volcano plot is showing high number of genes are differentially expressed after removal of H3.1K27M in SU-DIPGXXXVI. (**C and D)** In both SU-DIPGIV and SU-DIPGXXXVI upon removal of H3K27M mutation and restoring of H3K27me2/me3, there are more genes downregulated in comparison with upregulated genes.

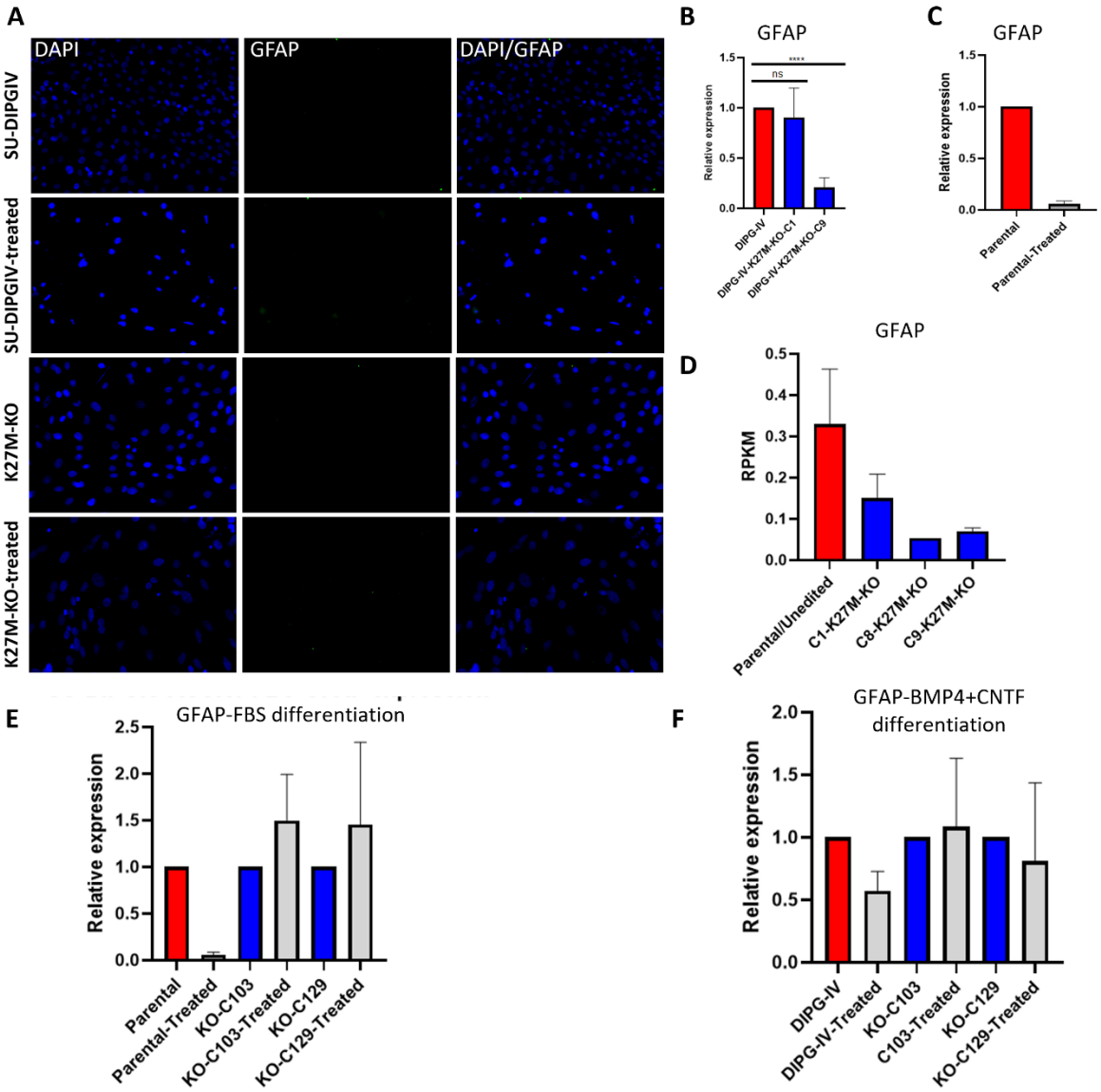
A
DAPI
GFAP
DAPI/GFAP
SU-DIPGIV
SU-DIPGIV-treated
K27M-KO
K27M-KO-treated
B
GFAP
Relative expression
ns
****
DIPG-IV
DIPG-IV-K27M-KO-C1
DIPG-IV-K27M-KO-C9
C
GFAP
Relative expression
Parental
Parental-Treated
D
GFAP
RPKM
Parental/Unedited
C1-K27M-KO
C8-K27M-KO
C9-K27M-KO
E
GFAP-FBS differentiation
Relative expression
Parental
Parental-Treated
KO-C103
KO-C103-Treated
KO-C129
KO-C129-Treated
F
GFAP-BMP4+CNTF differentiation
Relative expression
DIPG-IV
DIPG-IV-Treated
KO-C103
C103-Treated
KO-C129
KO-C129-Treated

Figure 4. 9. H3.1K27M cell lines are not able to be differentiated toward astrocytic fate.

(A) assessing differentiation potential of parental and isogenic H3.1K27M KO cell lines toward astrocyte. Differentiation induced by adding 10% FBS for two weeks. Differentiation results were checked by immunofluorescence staining using GFAP as mature astrocytes marker. **(B)** qRT-PCR results for GFAP expression in parental cell line and isogenic CRISPR edited clones in SU-DIPGIV. **(C)** qRT-PCR results for GFAP expression in parental cell line treated with 10% FBS for two weeks. **(D)** Bulk RNA-seq analysis of parental and different CRISPR edited clone from SU-DIPGIV cell lines showed modest decrease of GFAP expression in edited clones. RPKM values have been used to generate expression plot. **(E)** Differentiation of SU-DIPGIV parental cell line and ACVR1 KO cell lines assessed by FBS treatments for two weeks and evaluating GFAP expression levels using qRT_PCR. **(F)** Differentiation of SU-DIPGIV parental cell line and ACVR1 KO cell lines assessed by treatment of cells with BMP4 (20ng/ml) and CNTF (20ng/ml) for one week and followed by evaluating GFAP expression level using qRT-PCR. * represents $p<0.05$ for mean ± SEM for three independent experiments.

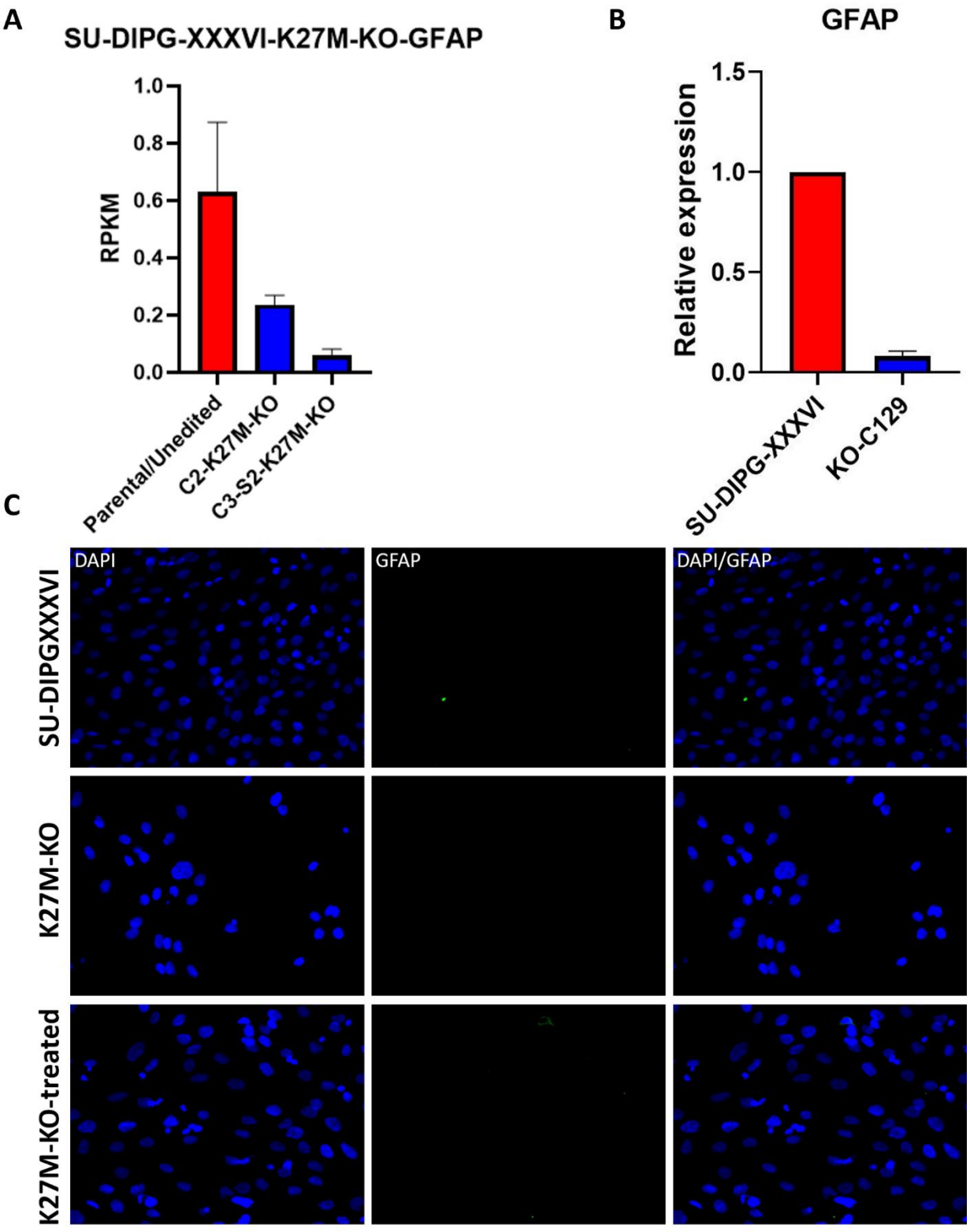
A
SU-DIPG-XXXVI-K27M-KO-GFAP
RPKM
1.0
0.8
0.6
0.4
0.2
0.0
Parental/Unedited
C2-K27M-KO
C3-S2-K27M-KO
B
GFAP
Relative expression
1.5
1.0
0.5
0.0
SU-DIPG-XXXVI
KO-C129
C
DAPI
GFAP
DAPI/GFAP
SU-DIPGXXXVI
K27M-KO
K27M-KO-treated

Figure 4. 10. SU-DIPGXXXVI is not differentiating toward astrocytic fate.

(A) Bulk RNA-seq analysis of parental and different CRISPR edited clone from SU-DIPGXXXVI cell lines showed modest decrease of GFAP expression in edited clones. RPKM values have been used to generate expression plot. **(B)** qRT-PCR results for GFAP expression in parental cell line and isogenic CRISPR edited clones in SU-DIPGXXXVI. **(C)**. assessing differentiation potential of parental and isogenic H3.1K27M KO cell lines toward astrocyte. Differentiation induced by adding 10% FBS for two weeks. Differentiation results were checked by immunofluorescence staining using GFAP as mature astrocytes marker. * represents $p<0.05$ for mean ± SEM for three independent experiments.

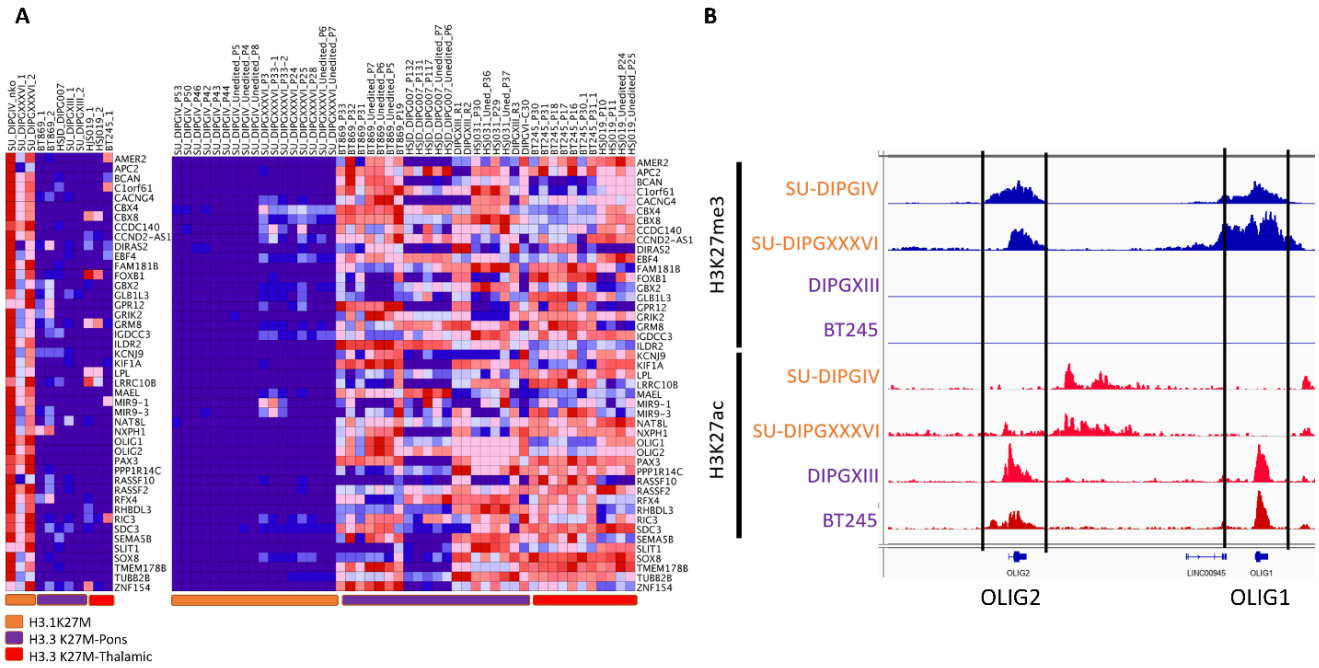

Figure 4. 11. H3.3K27M cell lines showed different deposition of H3K27me3 and gene expression in lineage specific transcription factors in comparison with H3.1K27M cell lines.

(A) H3K27me3 enriched in the promoter region of several transcription factors of H3.1K27M cell lines. **(B)** Gene expression results from bulk RNA-seq results revealed gene expression repression in those genes with higher level of H3K27me3 in their promoter regions. **(C)** ChIP-seq tracks for OLIG1 and OLIG2 as an examples of differentially expressed transcription factors between two contexts. H3K27me3 is absent in the promoter region of H3.3K27M cell lines and instead H3K27ac enriched in the same region.

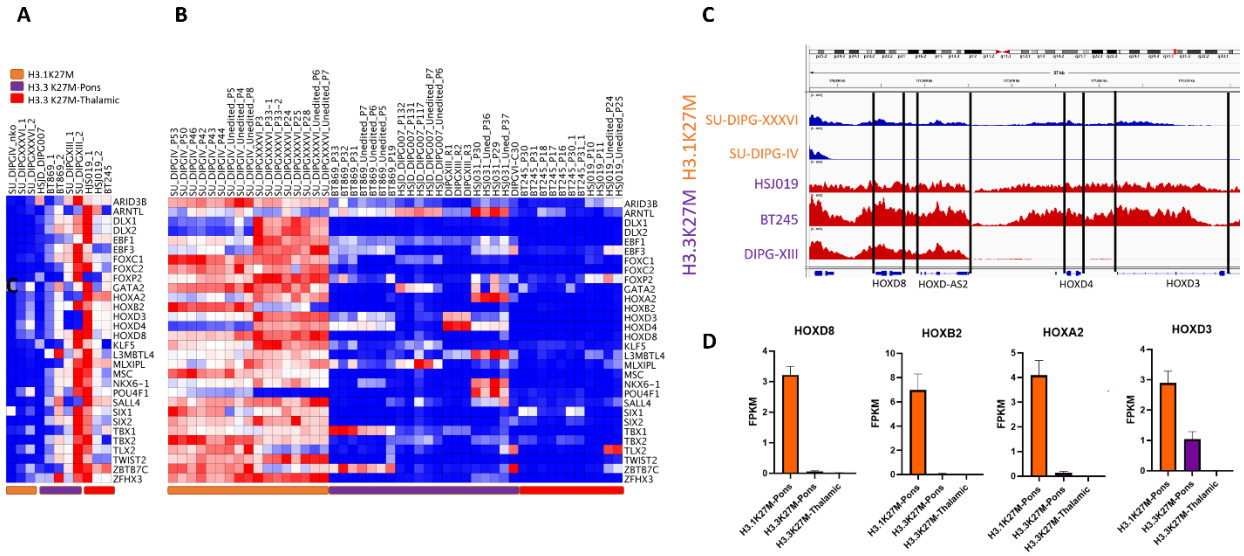

Figure 4. 12. H3.1K27M cell lines showed different deposition of H3K27me3 and gene expression in lineage specific transcription factors in comparison with H3.1K27M cell lines.

(A) H3K27me3 enriched in the promoter region of several transcription factors of H3.1K27M cell lines. **(B)** Gene expression results from bulk RNA-seq results revealed gene expression repression in those genes with higher level of H3K27me3 in their promoter regions. **(C)** ChIP-seq tracks for HOXD3 and HOXD4 as an example of differentially expressed transcription factors between two contexts. H3K27me3 is absent in the promoter region of H3.1K27M cell lines.

Chapter 4

Discussion

ACVR1 exerts different mechanisms in H3.1 and H3.3K27M contexts to induce tumorigenesis in diffuse intrinsic pontine gliomas

The finding that ACVR1 is mutated in 30% of DIPG cases has brought increased interest in the role of ACVR1 and its interplay with H3K27M mutations in DIPG tumorigenesis. The role of ACVR1 has been extensively studied in FOP, but it is still poorly understood in DIPGs. Here we show that ACVR1 is an important player in the tumorigenic effect of H3K27M in DIPGs. Crucially, we demonstrate that ACVR1 mutations act through distinct mechanisms in H3.3 and H3.1K27M DIPGs to induce tumorigenesis.

It has long been disputed that H3.1 and H3.3K27M pHGGs form two separate entities, with differences that encompass the transcriptome, DNA methylation, enhancer profiles, as well as genomic distribution underlying distinct chromatin and gene expression profiles (23,24,27,37). Intriguingly, a segregation of ACVR1 mutations between these two histone variant backgrounds also exists. ACVR1 mutations prevail in H3.1K27M DIPGs (~80%) compared to H3.3K27M DIPGs (~20%) (7,9). By analyzing publicly available data, we revealed a preferential segregation of ACVR1 R206H mutation with H3.3K27M DIPGs, whereas G328V/E mutations accompany H3.1K27M. These differences prompted us to ask whether ACVR1 mutations confer distinct effects on DIPG tumorigenesis in these two histone backgrounds, and in particular whether these differences are due to distinct cells of origin from which these two mutations emerge. Using RNA sequencing to profile the transcriptome of ACVR1 mutated H3.3 and H3.1K27M DIPG cell lines, we show important differences in gene expression between these two backgrounds. H3.3K27M DIPGs more closely resemble NPCs with a clear expression of OLIG2, NES, and SOX2 whereas H3.1K27M express genes involved in cell adhesion and cell-ECM interaction. Previous findings also show an enrichment of H3.3K27M DIPGs for early neural development genes (23,24). The discrepancies between the two H3K27M histone variants clearly highlight differences in cell of origin that underlie DIPG generation and prompted us to further investigate the role of ACVR1 mutations in these contexts.

The tumorigenic effect of H3K27M mutation in pHGGs is partly mediated by its ability to block differentiation of tumor cells and increase self-renewal capacity (38,39). Indeed, depletion of H3K27M in DIPGs enhances glial differentiation and increases survival *in vivo* (39). This suggests that DIPGs must be constituted of cells that are poised in a stem cell state and that the absence of K27M favors their reprogramming to glial cells. We demonstrate that H3.3K27M DIPG cell lines express NPC markers, OLIG2, NES, and SOX2, which is in complete accordance with the work of Filbin and colleagues that showed using single-cell RNA-seq that DIPGs are mainly constituted of OPC-like, astrocyte-like, oligodendrocyte-like and cycling/stem like cells (40). These findings, together with previous work, indicate that DIPGs may originate from an oligodendroglial origin and that an early developmental event accounted for this tumorigenic effect (24,41,42). There was a clear difference in the expression of stem cell markers between H3.1K27M and H3.3K27M DIPGs, suggesting that these two entities do not emerge from the same cell of origin. The question remains whether H3K27M obligate partners contribute to this segregation and whether these mutations exacerbate the effect of H3K27M on tumorigenesis. Previous work from our group shows that ACVR1 mutation is acquired early during development rather than being a subclonal defect (13). This suggests that ACVR1 might be implicated in the fate determination of H3.3K27M and H3.1K27M cells early during development. Here, we show that ACVR1 mutations largely contribute to the tumorigenicity of H3K27M and is a key player in the determination of cell fate in DIPGs. ACVR1 R206H mutation prevents H3.3K27M from differentiating to astrocytes and the removal of ACVR1 R206H cells reverses this process, an effect that is not observed with ACVR1 G328V/E mutations in H3.1K27M DIPGs. Our results propose that the role of ACVR1 activating mutations on DIPGs tumorigenesis is context dependent and is largely correlated with the histone variant mutation and the cell of origin. Using a transgenic mouse model, Fortin and colleagues overexpressed ACVR1 G328V mutation in Olig2 positive cells. They showed that the ACVR1 G328V mutation blocks differentiation of Olig2 positive cells and enhances cell proliferation in part through activation of the cell cycle (15). Although these results disagree with our findings that ACVR1 G328V does not induce glial differentiation, they do not completely rule out the possibility that ACVR1 G328V mutation could induce glial differentiation in cells that are already destined towards this fate, such as in Olig2 positive cells. Interestingly, ACVR1 G328V was

unable to induce tumor formation alone or in the presence of H3.1K27M when expressed in Olig2 positive cells. Tumor formation required additional mutations such as PIK3CA in this context (15). These results indicate that the role of ACVR1 activating mutations is context dependent and that Olig2 positive cells do not support the tumorigenic effect of H3.1K27M ACVR1 G328V, and thus do not constitute the correct cell of origin for these mutations, which is in line with our findings. Thus, determining DIPG cells of origin would be of key importance for studying the role of ACVR1 mutations in tumorigenesis. We found that NPCs differentiate to glial cells in response to BMP signaling and that the BMP pathway affects proliferation of these cells. Moreover, NPCs overexpressing ACVR1 R206H mutations mimic H3.3K27M/ACVR1 R206H DIPGs in response to BMPs as well as the aberrant response to activin A, characterized by a decrease in proliferation and activation of pSMAD1/5. Interestingly, NPCs overexpressing G328V/E mutations were not able to survive, suggesting that NPCs do not constitute a suitable environment for the maintenance of this mutation.

BMP signaling plays a crucial role at different stages of brain development (43). Throughout development, differential interplay between BMPs and BMP receptors shapes the architecture of the nervous system and their effects depend on the developmental stage of progenitor cells (43–45). In particular, the role of BMP signaling in promoting astrocytic differentiation has long been documented (45–47), in line with our results that NPCs treated with BMPs differentiate to astrocytes. It has been demonstrated that gradient formation of BMPs allow embryonic development in zebrafish (48) and Drosophila (49). In addition, the BMP ligand effect on stemness could be both context- and dose-dependent. For example, human embryonic stem cells maintain their pluripotency properties at low levels of BMP4 (below 2ng/ml) but higher concentrations of BMP4 promote their differentiation toward mesenchymal lineages (50,51). This effect was also shown in fibroblasts derived from FOP patients (harboring ACVR1 R206H mutation) that showed high efficiency of reprogramming into induced pluripotent stem cells (52). Our results point to a dose dependent effect of BMP signaling activation in DIPGs. Whereas BMP4 induces astrocytic differentiation of HSJD-DIPG007 and BT869, a slight activation of the receptor induced by the ACVR1 mutation prevents glial differentiation. Removal of ACVR1 in BT869 is sufficient to induce their differentiation to astrocytes. Taking into account the aberrant activation

of ACVR1 in DIPGs, this suggests that, in this context, ACVR1 potentiates the effect of H3K27M on stemness maintenance and that removal of ACVR1 relieves this phenotype. In contrast, exogenous activation of BMP signaling with BMP ligands contributes to the activation of multiple ALK receptors and pathways that could contribute to differentiation.

In striking contrast to H3.3K27M ACVR1 R206H mutations, we show that H3.1K27M DIPGs harboring ACVR1 G328V/E mutations activate different pathways. These pathways include mesenchymal properties related to cell adhesion, extracellular matrix interaction and cytokine secretion. Zebrafish models for FOP showed variable effects of ACVR1 mutations on dorsoventral patterning of zebrafish embryos (9), which would probably be attributed to different kinase activities of the receptors harboring these mutations as well as distinct pathway crosstalk mechanisms (53). We observed an increase in the expression of genes correlated with epithelial-mesenchymal transition (EMT) and tumor progression such as TWIST2 and Collagen genes. Indeed, evidence indicates an increased correlation between ACVR1 and EMT in gastric cancer (54). In view of the differences between the ACVR1 R206H and G328E/V mutations, it is very possible that different signaling pathways and crosstalk among them are implicated. This leads to the activation of several mechanisms potentialized by the differences in oncohistone variants, ultimately contributing to distinct tumorigenic mechanisms in DIPGs. In line with this, we document that ACVR1 is a crucial player in DIPG tumorigenesis. Removal of ACVR1 prolongs survival of mice in H3.1 and H3.3K27M contexts when injected subcutaneously or orthotopically in the pons, respectively.

Despite the importance of ACVR1 mutations in the tumorigenic effect of DIPGs, there is an obligate requirement of H3K27M for the development of tumorigenesis (14,15), which is in accordance with the fact that patients with FOP do not have a propensity to develop DIPGs. Altogether, the aforementioned results indicate that H3K27M and ACVR1 mutations act in concordance towards the maintenance of stemness and the induction of tumorigenesis in DIPGs.

Our results clearly state the importance of ACVR1 in DIPG tumorigenesis, which places ACVR1 as a potential therapeutic target in DIPGs. To date, multiple ACVR1 inhibitors were developed and are in clinical trials for FOP. Many of these inhibitors have shown efficacy in the treatment of

DIPGs (16), however, no progress in clinical trials has been made. In addition, all the inhibitors developed so far show low or no specificity to ALK2, with wide inhibition of other ALK receptors. The recently developed M4K2009 inhibitor is a potent, orally bioavailable and highly brain penetrant ACVR1 inhibitor (35,36) that shows high specificity to ALK2, as we demonstrate in our study by the lack of potency in ACVR1 KO cells. M4K2009 was able to decrease cell proliferation *in vitro* as well as the clonogenic potential of cells. Further studies on this compound as well as newly developed M4K compounds are underway to determine their efficacy in *in vivo* models of DIPGs.

In this study we demonstrate that ACVR1 exerts differential effects in DIPGs when associated with different oncohistone variants. We show that ACVR1 R206H contributes to the maintenance of stemness whereas G328E/V mutations affect mesenchymal properties of the cells leading to tumorigenesis progression through different mechanisms. We suggest that ACVR1 mutations in DIPGs potentially underlie different cells of origin and future studies would aim to better understand the mechanisms of these mutations allowing the development of improved treatments for DIPGs.

H3.1K27M and H3.3K27M mutations have differential effects on the epigenome

In addition to the different role of ACVR1 mutations in H3.1K27M and H3.3K27M, there are many papers that have investigated possible differences in epigenetic, morphogenic and lineage of origin between these two contexts. One of the earliest reports determined that DIPGs with H3.1K27M and ACVR1 mutations show mesenchymal and pro-angiogenic signature gene expression signatures in comparison with H3.3K27M mutant cell lines (63). More recently, Hoeman et al., demonstrated that the overexpression of ACVR1 and H3.1K27M mutations in mouse models led to the generation of glioma-like lesions with endothelial and mesenchymal gene signatures(14). It has been shown that the ACVR1 mutation induced a mesenchymal signature and this effect significantly increased in the presence of H3.1K27M mutations. For example, the presence of these two mutations led to the upregulation of mesenchymal genes, including CD44, TNC and Snail2 but the downregulation of proneural and glial lineage regulator Sox10. Studying DIPG samples from patients, including H3K27M mutants and non-H3K27M mutants, using single cell RNA-seq data showed higher level of genes involved in epithelial to mesenchymal transition (EMT) in K27M mutated samples in comparison with wildtype patients (47). Interestingly, they found H3.3K27M samples were enriched for epithelial signatures but H3.1K27M showed higher expression levels for mesenchymal signatures (47). Single cell RNA-seq analysis and scoring EMT showed higher scores and completeness of EMT in H3.1K27M tumors rather than H3.3K27M tumors (47). Studying H3.1K27M (SU-DIPGIV) and H3.3K27M (SU_DIPGVI and JHH-DIPG1) cell lines revealed higher mesenchymal signatures in H3.1K27M cell lines in comparison with H3.3K27M cell lines (47). As H3.1K27M and ACVR1 mutations mainly co-occur in DIPGs and because it has been shown that these two mutations could work synergistically to induce mesenchymal signatures, the well-known functions of BMP signaling may have the potential to provide a better understanding of mesenchymal signature in these tumors. Even before discovering H3K27M mutations, molecular profiling of DIPGs showed two distinct categories; the first group with mesenchymal and pro-angiogenic characteristics and the second group with oligodendroglia features, which are largely driven by PDGFRA (amplification and/or novel missense mutations). All of these documents are consistent with our results supporting our findings that H3.1K27M have possible origins from different cells or lineage of origins.

Meanwhile, our results reinforce that H3.3K27M more closely resemble NPCs and oligodendroglia progenitors with higher expression levels of OLIG2 and OLIG1. Our findings also supported the ability of H3.3K27M to be differentiated into an astrocytic lineage upon removal of the ACVR1 mutation or using differentiation protocols. In addition, DIPG tumors with H3.3K27M mutations that show higher levels of OLIG2 exhibit corresponding elevated levels of PDGFRA expression. By removing ACVR1 mutations from the BT869 cell line (H3.3K27M mutated), two master regulators of oligodendrocyte progenitors CSPG4/NG2 and PDGFRA were downregulated. On the other hand, our transcriptomic and epigenomic profiling showed lower expression levels of neural progenitor cell and oligodendrocyte progenitor cell regulators in H3.1K27M. For example, OLIG2 exhibits higher levels of the inhibitory mark, H3K27me3, in promoter regions and the absence of activation mark, H3K27ac. This is consistent with the gene expression level of this master regulator in H3.1K27M cell lines. In addition, single sample gene set enrichment analysis (ssGSEA) and deconvolution of bulk transcriptomic datasets using single cell RNA-seq data from mouse brain atlas (112) and single cell RNA-seq data from developing mouse brain (79) showed a higher enrichment of oligodendrocyte progenitor cell signatures in H3.3K27M in comparison with H3.1K27M cell lines. Lower levels of NPC and OPC regulators and lower enrichment of OPCs in H3.1K27M was accompanied by both a higher expression in the number of HOX genes and higher enrichment for mesenchymal signatures. Our isogenic experiments confirmed these observations. As evidenced, upon removal of ACVR1 mutations from H3.1K27M cell lines, there was no significant enrichment in astrocyte differentiation, even though there appeared to be a modest decrease in GFAP expression. Furthermore, removal of ACVR1 mutations in H3.1K27M showed significant changes in the expression of genes related to the extracellular matrix. Finally, two distinct astrocyte differentiation protocols on parental cell lines showed ACVR1-KO and H3.1K27M-KO do not differentiate into astrocytes. In summary, transcriptomic and epigenomic experiments, besides functional experiments, showed H3.1K27M and H3.3K27M raised from different cell or lineage of origins led to different transcriptomic, epigenomic, stem cell and differentiation behaviors.

Epigenetic differences between H3.1K27M and H3.3K27M have been the topic of new research in the field. Castel et al., (2018), for example, used bulk RNA-seq data derived from the tumors

of DMG patients to study the differences in ChIP-seq experiments examining H3K27M (100). Their transcriptomic analysis using microarray technology from patient-derived tumor samples did not indicate any significant differences between H3.1K27M and H3.3K27M tumors. This is possibly due to low sample size with several batches of microarray samples tested. When bulk RNA-seq data was performed on 21 samples, tSNE analysis revealed distinct transcriptomic profiles between these two contexts. They analyzed differences and highlighted two transcription factors, OLIG2 and HOXD8 as exhibiting the majority of the differences between the two oncohistones (100). These transcriptomic differences were correlated with H3K27me3 levels. They showed OLIG2 was expressed at higher levels in H3.3K27M tumors with lower levels of inhibitory mark H3K27me3 and, on the other side, they found higher expressions of HOXD8 in H3.1K27M with lower levels of H3K27me3. These results are consistent with our transcriptomic and epigenomic analysis. We have found a longer list of transcription factors involved in stemness and lineage commitment in which the expression and profile of histone PTMs, including H3K27me3 and H3K27ac, showed two distinct identities between H3.1K27M and H3.3K27M. More recently, Sarthy et al., (2020) tried to address epigenic differences in genomic scale between H3.1K27M and H3.3K27M contexts (110). They have profiled H3K27me3 in DMG samples derived from patients and they have found a dramatic decrease of this mark for both mutations. Surprisingly, they showed the presence of some domains of H3K27me3 in H3.3K27M tumors but complete absence of this mark in H3.1K27M tumors (110). We tried to address differences between these contexts using ChIP-seq experiments for H3K27me2, H3K27me3, and H3K27ac histone PTMs and mass spectrometry data derived from DMGs samples. Our ChIP-seq results consistently showed a dramatic decrease in H3K27me3 in both contexts, despite higher levels of this mark in H3.3K27M cell lines. However, the mark is still present in H3.1K27M samples. These results have been confirmed using mass spectrometry data, so despite clear differences in both contexts, histone PTM is present in both contexts. In addition, we went further on to profile the H3K27me2 mark in both contexts, and we have found significantly lower level and lower spread of the H3K27me2 mark in H3.1K27M cell lines. Furthermore, our functional experiments using CRISPR-Cas9 system to remove H3.3K27M and H3.1K27M mutations clearly showed that these mutations are acting through similar mechanisms in

decreasing H3K27me2 and H3K27me3 modifications across the genome. We have shown completely different transcriptomic and epigenomic differences for lineage specific transcription factors between these two tumor types. These differences possibly arise from different cell or lineage of origins of these tumors. Recently, Nagaraja et al., (2019) used different experimental models to study differences between these two oncohistones (42). They differentiated human induced pluripotent stem cells into relevant stem cell populations, including NPC, pre-OPC, and early-OPCs to investigate early epigenetic events upon introduction of H3.1K27M and H3.3K27M into these stem cell populations. To study these events, they induced each oncohistone for one cell cycle (14 days) and they profiled these cells using ChIP-seq experiments for H3K27me3.They found a similar loss of H3K27me3 but in different loci between H3.1K27M and H3.3K27M oncohistones (42). Nagaraja et al., (2019) results were consistent with our results supporting the same mechanism of action for both mutations but with different loci being affected. To highlight which cell of origin is showing higher correlation with DMGs derived from patients, they correlated the enhancer landscape of NPCs, pre-OPCs, and early-OPCs before and after oncohistone induction. They found early-OPCs with H3.3K27M mutation showed the highest enhancer similarity with H3.3K27M tumors. These correlations were weaker for all three cell populations with H3.1K27M mutations (42). So, authors highlighted the possibility that H3.1K27M tumors were derived from later stem cell populations in the glial lineage. These results highlight the importance and possible difference in cell of origins between H3.1K27M and H3.3K27M DMGs.

It has been shown in the presence of H3.3K27M mutations that there is a global decrease in the level of H3K27me2/me3 and a global increase in the level of H3K27ac modifications (24,26,27,80). Our research indicated that the presence of the H3.3K27M mutation led to pervasive acetylation across the genome (80). In this study, we found both mutations act through the same mechanism of action, so our H3K27ac profiling across DMG derived cell lines indicated the same pervasive acetylation in H3.1K27M cell lines, similar to those that have been reported for H3.3K27M.

Castel et al., (2018) used microarray gene expression analysis to show pontine and thalamic DMGs forming distinct transcriptomes from all other tumors (100). Our results distinctly

characterized tumors with H3.1K27M and H3.3K27M as having unique and recognizable transcriptomic and epigenomic profiles. We went on to ask whether we could identify differences based on tumor locations or not. The transcriptomic and epigenomic profiling for lineage specific transcription factors, specifically for the HOX gene, highlighted some differences between tumors derived from pontine and thalamic areas. As H3.1K27M genes exclusively occur in the pontine, they express HOX genes, including HOXA2, HOXB2, HOXD3, HOXD4, and HOXD8. Expression of these HOX genes is absent or undetectable in our bulk RNA-seq datasets. It is interesting that DIPG derived H3.3K27M cell lines (located in the pons) showed an intermediate expression between DIPGs with H3.1K27M (pontine) and DMGs with H3.3K27M (thalamic). For example, HOXD3 and HOXD4 showed higher expression levels, but lower H3K27me3 marks in the promoter region of H3.3K27M cell lines derived from pontine, including DIPGXIII and BT869. These two HOX transcription factors are completely silent with the presence of H3K27me3 in their promoter regions and a lack of expression in thalamic H3.3K27M cell lines.

In this study, we have showed that the H3K27M mutations showed the same mechanism of action in restricting H3K27me3 in DMGs. In addition, we have shown that H3K27me2 and H3K27me3 levels are lower in H3.1K27M in comparison with H3.3K27M. Removal of both mutations exhibit similar behaviors in regaining H3K27me2 and H3K27me3. Also, in the presence of these two oncohistones there are significant decreases of H3K27me2 and H3K27me3, which is consistent with genome wide pervasive acetylation in both contexts. Finally, we have found distinct transcriptomic and epigenomic profiles of lineage regulators which highlight different cells of origins.

Chapter 5

Conclusion and Future Directions

Conclusion

The role of ACVR1 in DIPGs is not clearly elucidated. In addition, the fact that different ACVR1 mutation variants segregate differently with the H3K27M histone mutations raises questions about the distinct roles of ACVR1 in these two contexts. This study reveals mechanistic differences for the different ACVR1 mutations in H3.1 and H3.3K27M DIPGs and reiterate the fact that they emerge from different cells of origin. We show that ACVR1 R206H mutation blocks astrocytic differentiation in H3.3K27M whereas ACVR1 G328E/V mutations confer H3.1K27M DIPGs a mesenchymal phenotype. ACVR1 is an important player in DIPG tumorigenesis *in vitro* and *in vivo* and a potential therapeutic target for the recently designed selective ACVR1 inhibitor, M4K2009. Our results suggest that H3.1K27M and H3.3K27M DIPGs emerge from a different cell of origin and implicate distinct roles for the different ACVR1 variant mutations.

Our data indicate that H3.1K27M in high grade gliomas shows more restricted deposition of H3K27me3/me3 compared to H3.3K27M tumors. H3K27me2/me3 restore upon removal of H3.1K27M and H3.3K27M mutations using CRISPR-Case9 system. In addition to transcriptomic and epigenomic analysis, functional experiments revealed H3.1K27M and H3.3K27M cell lines have different profile lineage specific transcription factors and capacity to be differentiated in oligodendroglial lineages. Our results suggesting that the effect of the methylation and distribution of H3K27me2/me3 marks is not due to the nature of the oncohistone variant but more the progenitor cell it arises in. The effect of canonical and noncanonical H3K27M oncohistones is reversible and converge to maintain H3K27me3 deposition to PRC2 nucleation sites, especially CGIs and restrain the spread of the mark from these sites.

Future directions

Based on our findings there are new question which will be valuable for future directions. Our main findings suggest H3.1K27M and H3.3K27M tumors arise from different cell of origins with distinct transcriptomic and epigenomic features. These identities indicate different profile of lineages specific transcription factors, different level of stemness, different differentiation potentials. It would be very interesting to determine exact developmental cell of origins for both of these cell identities, specifically for H3.1K27M tumors. Identifying those cells of origins will provide most reliable developmental contexts to study effect of different mutations in early events for tumorigenesis. We found BMP signaling activity is context dependent and contributes to tumorigenesis via distinct mechanisms in H3.1K27M and H3.3K27M contexts. So, access to exact cellular context to study these mutations *in vivo* will provide unique opportunity in understanding early events in tumorigenesis and possibly suggesting better treatment strategies. In addition, as these tumors arise from different cell or lineage identities, it will be interesting to study other related signaling pathways involved in nervous system development beside BMP signaling pathway to get deep insight into molecular mechanisms and deviation from normal development during tumorigenesis. For example, studying hedgehog (HH) and WNT and PI3K signaling pathways in parallel with BMP pathway and their effects on developmental pathway possibly will determine mesenchymal signature we have observed in our study. In addition to cell identities directions, there are interesting questions to follow in next studies, for example we found upon removing of ACVR1 mutations and injecting isogenic ACVR1 KO cells into mice, there is significant increase in survival time. It would be interesting to follow these cells *in vivo* to determine of tumor microenvironment of edited cells. In BT869 after CRISPR out ACVR1 mutation mice never formed tumors, so it will be interesting to do single cell RNA-seq and understand heterogeneity of tumor edited cells and microenvironment. Finally removing both ACVR1 and histone mutations in the same context at the same time could provide more details on possibly synergic effect of these mutations on lineage deviations during development.

Chapter 6

References

References:

1. Kaye EC, Baker JN, Broniscer A. Management of diffuse intrinsic pontine glioma in children: current and future strategies for improving prognosis. CNS Oncol. 2014;3:421–31.

2. Schwartzentruber J, Korshunov A, Liu XY, Jones DTW, Pfaff E, Jacob K, et al. Driver mutations in histone H3.3 and chromatin remodelling genes in paediatric glioblastoma. Nature. 2012;482:226–31.

3. Larson JD, Kasper LH, Paugh BS, Jin H, Wu G, Kwon CH, et al. Histone H3.3 K27M Accelerates Spontaneous Brainstem Glioma and Drives Restricted Changes in Bivalent Gene Expression. Cancer Cell. 2019;35:140-155.e7.

4. Pathania M, De Jay N, Maestro N, Harutyunyan AS, Nitarska J, Pahlavan P, et al. H3.3K27M Cooperates with Trp53 Loss and PDGFRA Gain in Mouse Embryonic Neural Progenitor Cells to Induce Invasive High-Grade Gliomas. Cancer Cell. 2017;32:684-700.e9.

5. Mackay A, Burford A, Carvalho D, Izquierdo E, Fazal-Salom J, Taylor KR, et al. Integrated Molecular Meta-Analysis of 1,000 Pediatric High-Grade and Diffuse Intrinsic Pontine Glioma. Cancer Cell. 2017;32:520-537.e5.

6. Taylor KR, Vinci M, Bullock AN, Jones C. ACVR1 mutations in DIPG: Lessons learned from FOP. Cancer Res. 2014;74:4565–70.

7. Fontebasso AM, Papillon-Cavanagh S, Schwartzentruber J, Nikbakht H, Gerges N, Fiset PO, et al. Recurrent somatic mutations in ACVR1 in pediatric midline high-grade astrocytoma. Nat Genet. Nature Publishing Group; 2014;46:462–6.

8. Taylor KR, Mackay A, Truffaux N, Butterfield YS, Morozova O, Philippe C, et al. Recurrent activating ACVR1 mutations in diffuse intrinsic pontine glioma. Nat Genet. Nature Publishing Group; 2014;46:457–61.

9. Wu G, Diaz AK, Paugh BS, Rankin SL, Ju B, Li Y, et al. The genomic landscape of diffuse intrinsic pontine glioma and pediatric non-brainstem high-grade glioma. Nat Genet.

2014;46:444–50.

10. Buczkowicz P, Hoeman C, Rakopoulos P, Pajovic S, Letourneau L, Dzamba M, et al. Genomic analysis of diffuse intrinsic pontine gliomas identifies three molecular subgroups and recurrent activating ACVR1 mutations. Nat Genet. Nature Publishing Group; 2014;46:451–6.

11. Shore EM, Xu M, Feldman GJ, Fenstermacher DA, Brown MA, Kaplan FS. A recurrent mutation in the BMP type I receptor ACVR1 causes inherited and sporadic fibrodysplasia ossificans progressiva. Nat Genet. 2006;38:525–7.

12. Han HJ, Jain P, Resnick AC. Shared ACVR1 mutations in FOP and DIPG: Opportunities and challenges in extending biological and clinical implications across rare diseases. Bone [Internet]. The Authors; 2018;109:91–100. Available from: https://doi.org/10.1016/j.bone.2017.08.001

13. Nikbakht H, Panditharatna E, Mikael LG, Li R, Gayden T, Osmond M, et al. Spatial and temporal homogeneity of driver mutations in diffuse intrinsic pontine glioma. Nat Commun. 2016;7.

14. Hoeman CM, Cordero FJ, Hu G, Misuraca K, Romero MM, Cardona HJ, et al. ACVR1 R206H cooperates with H3.1K27M in promoting diffuse intrinsic pontine glioma pathogenesis. Nat Commun [Internet]. Springer US; 2019;10. Available from: http://dx.doi.org/10.1038/s41467-019-08823-9

15. Fortin J, Tian R, Zarrabi I, Hill G, Williams E, Sanchez-Duffhues G, et al. Mutant ACVR1 Arrests Glial Cell Differentiation to Drive Tumorigenesis in Pediatric Gliomas. Cancer Cell [Internet]. Elsevier Inc.; 2020;37:308-323.e12. Available from: https://doi.org/10.1016/j.ccell.2020.02.002

16. Hoffman LM, Van Zanten SEMV, Colditz N, Baugh J, Chaney B, Hoffmann M, et al. Clinical, radiologic, pathologic, and molecular characteristics of long-term survivors of Diffuse Intrinsic Pontine Glioma (DIPG): A collaborative report from the International and European Society for Pediatric Oncology DIPG registries. J Clin Oncol. 2018;36:1963–72.

17. Mendez FM, Núñez FJ, Garcia-Fabiani MB, Haase S, Carney S, Gauss JC, et al. Epigenetic reprogramming and chromatin accessibility in pediatric diffuse intrinsic pontine gliomas: A neural developmental disease. Neuro Oncol. 2020;22:195–206.

18. Robison NJ, Kieran MW. Diffuse intrinsic pontine glioma: A reassessment. J Neurooncol. 2014;119:7–15.

19. Cohen KJ, Jabado N, Grill J. Diffuse intrinsic pontine gliomas - Current management and new biologic insights. Is there a glimmer of hope? Neuro Oncol. 2017;19:1025–34.

20. Cutter AR, Hayes JJ. A brief review of nucleosome structure. FEBS Lett. 2015;589:2914–22.

21. Ren M, Van Nocker S. In silico analysis of histone H3 gene expression during human brain development. Int J Dev Biol. 2016;60:167–73.

22. Cao R, Wang L, Wang H, Xia L, Erdjument-Bromage H, Tempst P, et al. Role of histone H3 lysine 27 methylation in polycomb-group silencing. Science (80-). 2002;298:1039–43.

23. Petryniak MA, Potter GB, Rowitch DH, Rubenstein JLR. Dlx1 and Dlx2 Control Neuronal versus Oligodendroglial Cell Fate Acquisition in the Developing Forebrain. Neuron. 2007;55:417–33.

24. Lewis PW, M. MM, S. KM, Francisco C, Shu L, A BL, et al. Inhibition of PRC2 Activity by a Gain-of-Function H3 Mutation Found in Pedriatic Glioblastoma. Science (80-). 2011;23:1–7.

25. Weinberg DN, Allis CD, Lu C. Oncogenic mechanisms of histone H3 mutations. Cold Spring Harb Perspect Med. 2017;7:1–14.

26. Piunti A, Hashizume R, Morgan MA, Bartom ET, Horbinski CM, Marshall SA, et al. Therapeutic targeting of polycomb and BET bromodomain proteins in diffuse intrinsic pontine gliomas. Nat Med. Nature Publishing Group; 2017;23:493–500.

27. Herz HM, Morgan M, Gao X, Jackson J, Rickels R, Swanson SK, et al. Histone H3 lysine-to-methionine mutants as a paradigm to study chromatin signaling. Science (80-).

2014;345:1065–70.

28. Cordero FJ, Huang Z, Grenier C, He X, Hu G, McLendon RE, et al. Histone H3.3K27M represses p16 to accelerate gliomagenesis in a murine model of DIPG. Mol Cancer Res. 2017;15:1243–54.

29. Paugh BS, Broniscer A, Qu C, Miller CP, Zhang J, Tatevossian RG, et al. Genome-wide analyses identify recurrent amplifications of receptor tyrosine kinases and cell-cycle regulatory genes in diffuse intrinsic pontine glioma. J Clin Oncol. 2011;29:3999–4006.

30. Zarghooni M, Bartels U, Lee E, Buczkowicz P, Morrison A, Huang A, et al. Whole-genome profiling of pediatric diffuse intrinsic pontine gliomas highlights platelet-derived growth factor receptor α and poly (ADP-ribose) polymerase as potential therapeutic targets. J Clin Oncol. 2010;28:1337–44.

31. Giacinti C, Giordano A. RB and cell cycle progression. Oncogene. 2006;25:5220–7.

32. Harutyunyan AS, Krug B, Chen H, Papillon-Cavanagh S, Zeinieh M, De Jay N, et al. H3K27M induces defective chromatin spread of PRC2-mediated repressive H3K27me2/me3 and is essential for glioma tumorigenesis. Nat Commun [Internet]. 2019;10:1262. Available from: http://www.nature.com/articles/s41467-019-09140-x

33. Silveira AB, Kasper LH, Fan Y, Jin H, Wu G, Shaw TI, et al. Correction to: H3.3 K27M depletion increases differentiation and extends latency of diffuse intrinsic pontine glioma growth in vivo (Acta Neuropathologica, (2019), 137, 4, (637-655), 10.1007/s00401-019-01975-4). Acta Neuropathol [Internet]. Springer Berlin Heidelberg; 2019;137:1021. Available from: https://doi.org/10.1007/s00401-019-02006-y

34. Cantone I, Fisher AG. Epigenetic programming and reprogramming during development. Nat Struct Mol Biol. 2013;20:282–9.

35. Atlasi Y, Stunnenberg HG. The interplay of epigenetic marks during stem cell differentiation and development. Nat Rev Genet [Internet]. Nature Publishing Group; 2017;18:643–58. Available from: http://dx.doi.org/10.1038/nrg.2017.57

36. Bernstein BE, Mikkelsen TS, Xie X, Kamal M, Huebert DJ, Cuff J, et al. A Bivalent Chromatin Structure Marks Key Developmental Genes in Embryonic Stem Cells. 2006;315–26.

37. Tate MC, Lindquist RA, Nguyen T, Sanai N, Barkovich AJ, Huang EJ, et al. Postnatal growth of the human pons: A morphometric and immunohistochemical analysis. J Comp Neurol. 2015;523:449–62.

38. Monje M, Mitra SS, Freret ME, Raveh TB, Kim J, Masek M, et al. Hedgehog-responsive candidate cell of origin for diffuse intrinsic pontine glioma. Proc Natl Acad Sci U S A. 2011;108:4453–8.

39. Lu QR, Yuk DI, Alberta JA, Zhu Z, Pawlitzky I, Chan J, et al. Sonic hedgehog-regulated oligodendrocyte lineage genes encoding bHLH proteins in the mammalian central nervous system. Neuron. 2000;25:317–29.

40. Lindquist RA, Guinto CD, Rodas-Rodriguez JL, Fuentealba LC, Tate MC, Rowitch DH, et al. Identification of proliferative progenitors associated with prominent postnatal growth of the pons. Nat Commun. Nature Publishing Group; 2016;7.

41. Funato K, Major T, Lewis PW, Allis CD, Tabar V. Use of human embryonic stem cells to model pediatric gliomas with H3.3K27M histone mutation. Science (80-). 2014;346:1529–33.

42. Nagaraja S, Quezada MA, Gillespie SM, Arzt M, Lennon JJ, Woo PJ, et al. Histone Variant and Cell Context Determine H3K27M Reprogramming of the Enhancer Landscape and Oncogenic State. Mol Cell [Internet]. Elsevier Inc.; 2019;76:965-980.e12. Available from: https://doi.org/10.1016/j.molcel.2019.08.030

43. Sun Y, Xu C, Pan C, Chen X, Geng Y, Wu Y, et al. Diffuse Intrinsic Pontine Gliomas Exhibit Cell Biological and Molecular Signatures of Fetal Hindbrain-Derived Neural Progenitor Cells. Neurosci Bull [Internet]. Springer Singapore; 2019;35:216–24. Available from: https://doi.org/10.1007/s12264-018-00329-6

44. Filbin MG, Tirosh I, Hovestadt V, Shaw ML, Escalante LE, Mathewson ND, et al. Developmental and oncogenic programs in H3K27M gliomas dissected by single-cell RNA-seq. Science (80-). 2018;360:331–5.

45. Sedykh I, Keller AN, Yoon B, Roberson L, Moskvin O V., Grinblat Y. Zebrafish Rfx4 controls dorsal and ventral midline formation in the neural tube. Dev Dyn. 2018;247:650–9.

46. Deaton AM, Bird A. CpG islands and the regulation of transcription. Genes Dev. 2011;25:1010–22.

47. Sanders LM, Cheney A, Seninge L, Van Den Bout A, Chen M, Beale HC, et al. Identification of a differentiation stall in epithelial mesenchymal transition in histone H3-mutant diffuse midline glioma. Gigascience. Oxford University Press; 2021;9:1–14.

48. Long W, Yi Y, Chen S, Cao Q, Zhao W, Liu Q. Potential new therapies for pediatric diffuse intrinsic pontine glioma. Front Pharmacol. 2017;8:1–13.

49. Wrana JL, Attisano L, Wieser R, Ventura F, Massagué J. Mechanism of activation of the TGF-β receptor. Nature. 1994;370:341–7.

50. Wrana JL. TGF-beta receptors and signalling mechanisms. Miner Electrolyte Metab. Switzerland; 1998;24:120–30.

51. Wang RN, Green J, Wang Z, Deng Y, Qiao M, Peabody M, et al. Bone Morphogenetic Protein (BMP) signaling in development and human diseases. Genes Dis [Internet]. Elsevier Ltd; 2014;1:87–105. Available from: http://dx.doi.org/10.1016/j.gendis.2014.07.005

52. Ramachandran A, Mehić M, Wasim L, Malinova D, Gori I, Blaszczyk BK, et al. Pathogenic ACVR1 R206H activation by Activin A-induced receptor clustering and autophosphorylation . EMBO J. 2021;40.

53. Hatsell SJ, Idone V, Wolken DMA, Huang L, Kim HJ, Wang L, et al. ACVR1R206H receptor mutation causes fibrodysplasia ossificans progressiva by imparting responsiveness to activin A. Sci Transl Med. 2015;7:1–12.

54. Hino K, Ikeya M, Horigome K, Matsumoto Y, Ebise H, Nishio M, et al. Neofunction of ACVR1 in fibrodysplasia ossificans progressiva. Proc Natl Acad Sci U S A. 2015;112:15438–43.

55. Bond AM, Bhalala OG, Kessler JA. The dynamic role of bone morphogenetic proteins in neural stem cell fate and maturation. Dev Neurobiol. 2012;72:1068–84.

56. Hegarty S V., O'Keeffe GW, Sullivan AM. BMP-Smad 1/5/8 signalling in the development of the nervous system. Prog Neurobiol [Internet]. Elsevier Ltd; 2013;109:28–41. Available from: http://dx.doi.org/10.1016/j.pneurobio.2013.07.002

57. Cheng X, Wang Y, He Q, Qiu M, Whittemore SR, Cao Q. Bone Morphogenetic Protein Signaling and Olig1/2 Interact to Regulate the Differentiation and Maturation of Adult Oligodendrocyte Precursor Cells. Stem Cells. 2007;25:3204–14.

58. Bjartmar C, Kidd G, Mörk S, Rudick R, Trapp BD. Neurological disability correlates with spinal cord axonal loss and reduced N-acetyl aspartate in chronic multiple sclerosis patients. Ann Neurol. 2000;48:893–901.

59. Kan L, Kitterman JA, Procissi D, Chakkalakal S, Peng CY, McGuire TL, et al. CNS demyelination in fibrodysplasia ossificans progressiva. J Neurol. 2012;259:2644–55.

60. Lasorella A, Benezra R, Iavarone A. The ID proteins: Master regulators of cancer stem cells and tumour aggressiveness. Nat Rev Cancer. Nature Publishing Group; 2014;14:77–91.

61. Park NI, Guilhamon P, Desai K, McAdam RF, Langille E, O'Connor M, et al. ASCL1 Reorganizes Chromatin to Direct Neuronal Fate and Suppress Tumorigenicity of Glioblastoma Stem Cells. Cell Stem Cell [Internet]. Elsevier Inc.; 2017;21:209-224.e7. Available from: http://dx.doi.org/10.1016/j.stem.2017.06.004

62. Carro MS, Lim WK, Alvarez MJ, Bollo RJ, Zhao X, Snyder EY, et al. The transcriptional network for mesenchymal transformation of brain tumours. Nature. Nature Publishing Group; 2010;463:318–25.

63. Castel D, Philippe C, Calmon R, Le Dret L, Truffaux N, Boddaert N, et al. Histone H3F3A and HIST1H3B K27M mutations define two subgroups of diffuse intrinsic pontine gliomas with different prognosis and phenotypes. Acta Neuropathol. Springer Berlin Heidelberg; 2015;130:815–27.

64. Puget S, Philippe C, Bax DA, Job B, Varlet P, Junier MP, et al. Mesenchymal transition and pdgfra amplification/mutation are key distinct oncogenic events in pediatric diffuse intrinsic pontine gliomas. PLoS One. 2012;7.

65. Ran FA, Hsu PD, Wright J, Agarwala V, Scott DA, Zhang F. Genome engineering using the CRISPR-Cas9 system. Nat Protoc. 2013;8:2281–308.

66. Chu VT, Weber T, Wefers B, Wurst W, Sander S, Rajewsky K, et al. Increasing the efficiency of homology-directed repair for CRISPR-Cas9-induced precise gene editing in mammalian cells. Nat Biotechnol. 2015;33:543–8.

67. Pajovic S, Siddaway R, Bridge T, Sheth J, Rakopoulos P, Kim B, et al. Epigenetic activation of a RAS/MYC axis in H3.3K27M-driven cancer. Nat Commun [Internet]. Springer US; 2020;11. Available from: http://dx.doi.org/10.1038/s41467-020-19972-7

68. Dirkse A, Golebiewska A, Buder T, Nazarov P V., Muller A, Poovathingal S, et al. Stem cell-associated heterogeneity in Glioblastoma results from intrinsic tumor plasticity shaped by the microenvironment. Nat Commun [Internet]. Springer US; 2019;10:1–16. Available from: http://dx.doi.org/10.1038/s41467-019-09853-z

69. Jessa S, Blanchet-Cohen A, Krug B, Vladoiu M, Coutelier M, Faury D, et al. Stalled developmental programs at the root of pediatric brain tumors [Internet]. Nat. Genet. Springer US; 2019. Available from: http://dx.doi.org/10.1038/s41588-019-0531-7

70. Magistri M, Khoury N, Mazza EMC, Velmeshev D, Lee JK, Bicciato S, et al. A comparative transcriptomic analysis of astrocytes differentiation from human neural progenitor cells. Eur J Neurosci. 2016;44:2858–70.

71. Bourgey M, Dali R, Eveleigh R, Chen KC, Letourneau L, Fillon J, et al. GenPipes: An open-

source framework for distributed and scalable genomic analyses. Gigascience. Oxford University Press; 2019;8:1–11.

72. Bolger AM, Lohse M, Usadel B. Trimmomatic: A flexible trimmer for Illumina sequence data. Bioinformatics. 2014;30:2114–20.

73. Dobin A, Davis CA, Schlesinger F, Drenkow J, Zaleski C, Jha S, et al. STAR: Ultrafast universal RNA-seq aligner. Bioinformatics. 2013;29:15–21.

74. Anders S, Huber W. Differential expression analysis for sequence count data. Genome Biol [Internet]. 2010;11:R106. Available from: https://doi.org/10.1186/gb-2010-11-10-r106

75. Robinson MD, McCarthy DJ, Smyth GK. edgeR: A Bioconductor package for differential expression analysis of digital gene expression data. Bioinformatics. 2009;26:139–40.

76. Raudvere U, Kolberg L, Kuzmin I, Arak T, Adler P, Peterson H, et al. G:Profiler: A web server for functional enrichment analysis and conversions of gene lists (2019 update). Nucleic Acids Res. Oxford University Press; 2019;47:W191–8.

77. Korotkevich G, Sukhov V, Budin N, Shpak B, Artyomov M, Sergushichev A. Fast gene set enrichment analysis. 2016;

78. Reich M, Liefeld T, Gould J, Lerner J, Tamayo P, Mesirov JP. GenePattern 2.0. Nat Genet [Internet]. 2006;38:500–1. Available from: https://doi.org/10.1038/ng0506-500

79. Rosenberg AB, Roco CM, Muscat RA, Kuchina A, Sample P, Yao Z, et al. Single-cell profiling of the developing mouse brain and spinal cord with split-pool barcoding. Science (80-). 2018;360:176–82.

80. Krug B, De Jay N, Harutyunyan AS, Deshmukh S, Marchione DM, Guilhamon P, et al. Pervasive H3K27 Acetylation Leads to ERV Expression and a Therapeutic Vulnerability in H3K27M Gliomas. Cancer Cell [Internet]. Elsevier Inc.; 2019;35:782-797.e8. Available from: https://doi.org/10.1016/j.ccell.2019.04.004

81. Li H, Durbin R. Fast and accurate short read alignment with Burrows-Wheeler transform.

Bioinformatics. 2009;25:1754–60.

82. Heinz S, Benner C, Spann N, Bertolino E, Lin YC, Laslo P, et al. Simple Combinations of Lineage-Determining Transcription Factors Prime cis-Regulatory Elements Required for Macrophage and B Cell Identities. Mol Cell [Internet]. Elsevier Inc.; 2010;38:576–89. Available from: http://dx.doi.org/10.1016/j.molcel.2010.05.004

83. Younesy H, Möller T, Lorincz MC, Karimi MM, Jones SJM. VisRseq: R-based visual framework for analysis of sequencing data. BMC Bioinformatics. 2015;16:1–14.

84. Ramírez F, Ryan DP, Grüning B, Bhardwaj V, Kilpert F, Richter AS, et al. deepTools2: a next generation web server for deep-sequencing data analysis. Nucleic Acids Res [Internet]. 2016;44:W160–5. Available from: https://doi.org/10.1093/nar/gkw257

85. Carroll TS, Liang Z, Salama R, Stark R, de Santiago I. Impact of artifact removal on ChIP quality metrics in ChIP-seq and ChIP-exo data. Front Genet. 2014;5:1–11.

86. Thorvaldsdóttir H, Robinson JT, Mesirov JP. Integrative Genomics Viewer (IGV): high-performance genomics data visualization and exploration. Brief Bioinform [Internet]. 2013;14:178–92. Available from: https://doi.org/10.1093/bib/bbs017

87. Weinberg DN, Papillon-Cavanagh S, Chen H, Yue Y, Chen X, Rajagopalan KN, et al. The histone mark H3K36me2 recruits DNMT3A and shapes the intergenic DNA methylation landscape. Nature [Internet]. 2019;573:281–6. Available from: https://doi.org/10.1038/s41586-019-1534-3

88. Harutyunyan AS, Chen H, Lu T, Horth C, Nikbakht H, Krug B, et al. H3K27M in Gliomas Causes a One-Step Decrease in H3K27 Methylation and Reduced Spreading within the Constraints of H3K36 Methylation. Cell Rep [Internet]. ElsevierCompany.; 2020;33:108390. Available from: https://doi.org/10.1016/j.celrep.2020.108390

89. Liao Y, Smyth GK, Shi W. FeatureCounts: An efficient general purpose program for assigning sequence reads to genomic features. Bioinformatics. 2014;30:923–30.

90. Liao Y, Smyth GK, Shi W. The R package Rsubread is easier, faster, cheaper and better for

alignment and quantification of RNA sequencing reads. Nucleic Acids Res. Oxford University Press; 2019;47.

91. Killick R, Eckley IA. changepoint: An R Package for Changepoint Analysis. J Stat Softw [Internet]. 2014;58:1–19. Available from: https://www.jstatsoft.org/index.php/jss/article/view/v058i03

92. Quinlan AR, Hall IM. BEDTools: A flexible suite of utilities for comparing genomic features. Bioinformatics. 2010;26:841–2.

93. Zhang Y, Liu T, Meyer CA, Eeckhoute J, Johnson DS, Bernstein BE, et al. Model-based analysis of ChIP-Seq (MACS). Genome Biol. 2008;9.

94. Lovén J, Hoke HA, Lin CY, Lau A, Orlando DA, Vakoc CR, et al. Selective inhibition of tumor oncogenes by disruption of super-enhancers. Cell. 2013;153:320–34.

95. Carvalho D, Taylor KR, Olaciregui NG, Molinari V, Clarke M, Mackay A, et al. ALK2 inhibitors display beneficial effects in preclinical models of ACVR1 mutant diffuse intrinsic pontine glioma. Commun Biol [Internet]. Springer US; 2019;2. Available from: http://dx.doi.org/10.1038/s42003-019-0420-8

96. Machiya A, Tsukamoto S, Ohte S, Kuratani M, Fujimoto M, Kumagai K, et al. Effects of FKBP12 and type II BMP receptors on signal transduction by ALK2 activating mutations associated with genetic disorders. Bone [Internet]. The Authors; 2018;111:101–8. Available from: https://doi.org/10.1016/j.bone.2018.03.015

97. Shen Q, Little SC, Xu M, Haupt J, Ast C, Katagiri T, et al. The fibrodysplasia ossificans progressiva R206H ACVR1 mutation activates BMP-independent chondrogenesis and zebrafish embryo ventralization. J Clin Invest. 2009;119:3462–71.

98. Groppe JC, Wu J, Shore EM, Kaplan FS. In vitro analyses of the dysregulated R206H ALK2 kinase-FKBP12 interaction associated with heterotopic ossification in FOP. Cells Tissues Organs. 2011;194:291–5.

99. Hildebrand L, Stange K, Deichsel A, Gossen M, Seemann P. The Fibrodysplasia Ossificans

Progressiva (FOP) mutation p.R206H in ACVR1 confers an altered ligand response. Cell Signal [Internet]. Elsevier Inc.; 2017;29:23–30. Available from: http://dx.doi.org/10.1016/j.cellsig.2016.10.001

100. Castel D, Philippe C, Kergrohen T, Sill M, Merlevede J, Barret E, et al. Transcriptomic and epigenetic profiling of “diffuse midline gliomas, H3 K27M-mutant” discriminate two subgroups based on the type of histone H3 mutated and not supratentorial or infratentorial location. Acta Neuropathol Commun. Acta Neuropathologica Communications; 2018;6:117.

101. Shaltouki A, Peng J, Liu Q, Rao MS, Zeng X. Efficient generation of astrocytes from human pluripotent stem cells in defined conditions. Stem Cells. 2013;31:941–52.

102. Toofan P, Busch C, Morrison H, O’Brien S, Jørgensen H, Copland M, et al. Chronic myeloid leukaemia cells require the bone morphogenic protein pathway for cell cycle progression and self-renewal. Cell Death Dis. 2018;9.

103. Swarbrick A, Åkerfeldt MC, Lee CSL, Sergio CM, Caldon CE, Hunter LJK, et al. Regulation of cyclin expression and cell cycle progression in breast epithelial cells by the helix-loop-helix protein Id1. Oncogene. 2005;24:381–9.

104. Lee JY, Kang MB, Jang SH, Qian T, Kim HJ, Kim CH, et al. Id-1 activates Akt-mediated Wnt signaling and p27Kip1 phosphorylation through PTEN inhibition. Oncogene. 2009;28:824–31.

105. Di L, Liu LJ, Yan YM, Fu R, Li Y, Xu Y, et al. Discovery of a natural small-molecule compound that suppresses tumor EMT, stemness and metastasis by inhibiting TGFβ/BMP signaling in triple-negative breast cancer. J Exp Clin Cancer Res. 2019;38:1–15.

106. Tian H, Zhou T, Chen H, Li C, Jiang Z, Lao L, et al. Bone morphogenetic protein-2 promotes osteosarcoma growth by promoting epithelial-mesenchymal transition (EMT) through the Wnt/β-catenin signaling pathway. J Orthop Res. 2019;37:1638–48.

107. Sanvitale CE, Kerr G, Chaikuad A, Ramel MC, Mohedas AH, Reichert S, et al. A New Class

of Small Molecule Inhibitor of BMP Signaling. PLoS One. 2013;8.

108. Smil D, Wong JF, Williams EP, Adamson RJ, Howarth A, McLeod DA, et al. Leveraging an Open Science Drug Discovery Model to Develop CNS-Penetrant ALK2 Inhibitors for the Treatment of Diffuse Intrinsic Pontine Glioma. J Med Chem. 2020;63:10061–85.

109. Ensan D, Smil D, Zepeda-Velázquez CA, Panagopoulos D, Wong JF, Williams EP, et al. Targeting ALK2: An Open Science Approach to Developing Therapeutics for the Treatment of Diffuse Intrinsic Pontine Glioma. J Med Chem. 2020;63:4978–96.

110. Sarthy JF, Meers MP, Janssens DH, Henikoff JG, Feldman H, Paddison PJ, et al. Histone deposition pathways determine the chromatin landscapes of h3.1 and h3.3 k27m oncohistones. Elife. 2020;9:1–18.

111. Lambert SA, Jolma A, Campitelli LF, Das PK, Yin Y, Albu M, et al. The Human Transcription Factors. Cell [Internet]. Elsevier Inc.; 2018;172:650–65. Available from: https://doi.org/10.1016/j.cell.2018.01.029

112. La Manno G, Siletti K, Furlan A, Gyllborg D, Vinsland E, Mossi Albiach A, et al. Molecular architecture of the developing mouse brain. Nature [Internet]. Springer US; 2021;596:92–6. Available from: http://dx.doi.org/10.1038/s41586-021-03775-x